EFFECT OF SPECTRAL FILTERING ON PULSE DYNAMICS OF ULTRAFAST FIBER OSCILLATORS AT NORMAL DISPERSION

Dissertation

Submitted to

The School of Engineering of the

UNIVERSITY OF DAYTON

In Partial Fulfillment of the Requirements for

The Degree of

Doctor of Philosophy in Electro-Optics

By

Ankita Nayankumar Khanolkar

Dayton, Ohio

August, 2021

University *of* Dayton

EFFECT OF SPECTRAL FILTERING ON PULSE DYNAMICS OF ULTRAFAST FIBER OSCILLATORS AT NORMAL DISPERSION

Name: Khanolkar, Ankita Nayankumar

APPROVED BY:

Andy Chong, Ph.D.
Advisory Committee Chairman
Associate Professor, Physics and Electro-Optics and Photonics

Imad Agha, Ph.D.
Committee Member
Associate Professor, Physics and Electro-Optics and Photonics

Todd B. Smith, Ph.D.
Committee Member
Associate Professor, Physics

Andrew Sarangan, Ph.D., P.E.
Committee Member
Professor, Electro-Optics and Photonics

Robert J. Wilkens, Ph.D., P.E.
Associate Dean for Research and Innovation
School of Engineering

Margaret F. Pinnell, Ph.D.
Interim Dean, School of Engineering

ABSTRACT

EFFECT OF SPECTRAL FILTERING ON PULSE DYNAMICS OF ULTRAFAST FIBER OSCILLATORS AT NORMAL DISPERSION

Name: Khanolkar, Ankita Nayankumar
University of Dayton

Advisor: Dr. Andy Chong

Mode-locked oscillators are the building blocks to generate ultrafast pulses which can then be used for many applications, including optical communication, metrology, spectroscopy, microscopy, material processing, as well as many applications in the healthcare industry. Mode-locked fiber oscillators are especially popular for their compactness, efficiency, and beam quality compared to their solid-state counterparts such as Ti:Sapphire lasers. Apart from their practicality, the mode-locked fiber lasers are an interesting object for studies, as they represent dynamically rich nonlinear systems.

For ultrafast fiber oscillators at normal dispersion, a spectral filter is the utmost important optical component that determines the behavior of these systems in terms of the spectral bandwidth, pulse duration, central wavelength of the output spectra, multipulse dynamics, pulse structure as well as pulse velocity. Recently, there is a growing interest in fiber based spectral filters as they facilitate construction of all-fiber laser cavities. This dissertation investigates the laser performance parameters by developing an all- fiber spectral filter and exploiting its characteristics. Especially, this dissertation reports the first experimental observation of dissipative solitons of the complex Swift Hohenberg equation. This is very important as it births multiple future projects related to implementing higher order spectral filtering in mode-locked fiber lasers.

Although most of the ultrafast oscillators in this dissertation are built at 1 μm, ideas to build mode-locked lasers at visible wavelengths are also presented along with primary numerical simulation and experimental results.

Finally, all the upcoming research directions are discussed in detail.

To my father, for whom nothing is dearer than his daughter

ACKNOWLEDGMENTS

There are not enough words to convey my deep gratitude and respect for my advisor, Dr. Andy Chong. Him being a renowned fiber laser scientist, his humbleness and simplicity always surprised me. He gave me the freedom to choose my research projects and he always protected my research interests despite facing multiple experimental difficulties. He helped me to become an independent researcher and a critical thinker. I will be forever indebted to him for teaching me how to build fiber lasers. I would also like to thank Dr. Imad Agha who consistently pushed me to break the limits when I was ready to settle down for a little. He is amazingly inventive and endlessly resourceful, the qualities which helped me on multiple occasions during my experiments. My sincere thanks must also go to the rest of the members of my dissertation committee: Dr. Todd Smith and Dr. Andrew Sarangan. In particular, Dr. Smith was always encouraging and showed constant support whenever I met him. Dr. Sarangan, in spite of being a late addition to the committee, offered great advice regarding my research projects and took immense interest in the tunable spectral filter project. I would like to offer special thanks to Dr. Joseph Haus, with whom, I published my first co-authored paper. Although he is no longer with us, continues to inspire me by his example and dedication to the students. I would also like to thank my funding sources - National Science Foundation (NSF) and Graduate Academic Affairs (GAA).

I owe much to my past and current co-workers in our ultrafast laser lab : Yimin Zang, Chunyang Ma, Xiaowei Ge, Dinesh Amal Mirando, Fanli Wei, Jianhao and Jordan Adams. It was an absolute pleasure to work on some of the projects together with them. Especially, Yimin Zang provided extensive support regarding numerical simulations for the complex Swift Hohenberg equation based fiber oscillator project. Because of Chunyang Ma I could get an invaluable experience of being a mentor which has helped me in the long run.

Joshua Burrow played an important role as a patient friend and mentor when I navigated through graduate school experience in a foreign country. I deeply thank him for his efforts in making me overcome my shyness and getting involved in scientific communities such as OSA and SPIE. Similarly, Dr. David Lombardo helped me countless times with research tools such as Overleaf and Inkscape. I would also extend my thanks to my friends and current and former colleagues from the department – Gary Sevison, Zairui Li, Diego Garcia, Long Wang, Chenchen Wan, Yining Liu, Mallik Hussain, Ujitha Abeywickrema and Roseanna Lawandi for their constant support. Much appreciation should be granted to the Department of Electro-Optics and Photonics, Department of Physics and Department of Electrical and Computer Science for providing a protective environment to an international student like me and for rendering impeccable services whenever needed.

I would like to thank my parents, whose love and guidance are with me in whatever I do. My father continuously encouraged and prepared me to pursue higher education. My mother who daily reminded me to graduate taught me perseverance. My sister looked after my parents when I was busy with my Ph.D. and I am very grateful for that gesture. I would also like to thank my friends Manisha Gonda, Sneha Patil, Nayana Kapse, Ruhi Redij and Ashish Rasam for tolerating my blabber regarding lasers. I also appreciate the support I received from the Dayton based families - Schommers and Jardines. I would be remiss if I did not acknowledge Adrian Pereira, for the innumerable sacrifices made by him, in shouldering far more than his fair share of the household burdens and financial aspects, for standing by me in my sickness and recovery, for celebrating my smallest of achievements, for inspiring me to fight for what is right and for not letting me give up when I encountered tough days while I pursued this degree.

TABLE OF CONTENTS

ABSTRACT iii

DEDICATION v

ACKNOWLEDGMENTS vi

LIST OF FIGURES xi

LIST OF TABLES xix

CHAPTER I. INTRODUCTION 1

1.1 Original contributions and publications 4
1.2 Organization of thesis 4
1.3 Nonlinear Schrödinger equation 6
1.4 Soliton solution of NLSE 7
1.5 Dispersion managed soliton 9
1.6 Similaritons 10
1.6.1 Passive similariton 11
1.6.2 Amplifier similariton 13
1.7 Ginzburg-Landau equation and dissipative solitons 14
1.8 Cubic Quintic Ginzburg-Landau equation and all-normal dispersion fiber laser 15
1.9 Mamyshev Oscillator 18
1.10 Saturable absorber 19
1.11 Spectral filter 20
1.11.1 Birefringence based filter 21
1.11.2 Interference filter 23
1.11.3 Dispersive element - waveguide filter 25
1.12 Optical fibers 26
1.12.1 Single mode and multimode fibers 26
1.12.2 Double clad fibers 27
1.12.3 Large mode area fibers 29
1.12.4 Polarization maintaining fibers 30
1.12.5 Photonic crystal fibers 31
1.12.6 Fluoride fibers 32

CHAPTER II. AN ALL-FIBER BANDWIDTH TUNABLE SPECTRAL FILTER 33

2.1 Introduction 33
2.2 Twisted PM fiber based spectral filter 34
2.3 PM-SMF-PM spectral filter 38
2.4 Experimental results 41
2.5 Temperature sensitivity of the spectral filter 46
2.5.1 Conclusion 48

CHAPTER III. AN ALL FIBER SPECTRAL FILTER FOR MULTIPULSE STATES MANAGEMENT IN FIBER LASERS 49

3.1 Introduction 49
3.2 The spectral filter design 51
3.3 Experimental results 53
3.4 Conclusion 60

CHAPTER IV. COMPLEX SWIFT HOHENBERG EQUATION BASED DISSIPATIVE SOLITON FIBER LASER 62

4.1 Introduction 62
4.2 Experimental Setup 65
4.3 Numerical simulation results 66
4.4 Experimental results 72
4.5 Additional experimental dataset 77
4.6 Modification to the laser cavity 79
4.7 Discussion 81
4.8 Conclusion 82

CHAPTER V. A WIDELY TUNABLE FIBER LASER USING GRATING COLLIMATOR SPECTRAL FILTER 83

5.1 Introduction 83
5.2 Experimental Set-up 85
5.3 Experimental Results 86
5.4 Discussion and conclusion 89

CHAPTER VI. FEW CYCLE PULSE GENERATION FROM A FIBER OSCILLATORS WITH A VERY NARROW INTRACAVITY SPECTRAL FILTER 91

6.1 Introduction 91
6.2 Numerical model of a self-similar oscillator with a PCF and results 94
6.3 Experimental results of a self-similar oscillator with a PCF 95
6.4 Experimental results of Mamyshev oscillator with an intracavity PCF . . 98
6.5 Conclusion 101

CHAPTER VII. VISIBLE FIBER LASER 102

7.1 Introduction 102
7.2 Pr doped visible fiber lasers 105
7.3 Simulation results 107
7.3.1 Simulation results at 520 nm 108
7.3.2 Simulation results at 605 nm 111
7.3.3 Simulation results at 635 nm 112
7.4 Proposed Pr doped fiber laser experimental cavities and design considerations 114
7.4.1 Pump diode 115
7.4.2 Gain fiber 115
7.4.3 Coupling optics 116
7.5 Experimental results 117
7.5.1 Experimental results for Pr:WPFG fiber 118
7.5.2 Experimental results for Pr, Yb:ZBLAN fiber 121
7.5.3 Experimental results for Pr:ZBLAN fiber 122

7.6 Discussion and future direction 128

CHAPTER VIII. FUTURE DIRECTIONS FOR ULTRAFAST FIBER LASERS RESEARCH 129

8.1 Summary of future research ideas 129
8.2 Noise like pulses from a mode-locked fiber laser 132
8.3 Dual wavelength mode-locking 134
8.4 Long duration energetic pulse generation from mode-locked fiber lasers . 135
8.5 Implementing higher order spectral filter in mode-locked fiber lasers . . . 136

BIBLIOGRAPHY 141

APPENDICES

A. Nonlinearity and Dispersion Parameter Calculation for Photonic Crystal Fiber 154

B. Group Velocity Dispersion Calculation for Praseodymium doped ZBLAN Fiber 158

LIST OF FIGURES

1.1 Schematic of a soliton fiber laser along with its dispersion map. The intracavity pulse shape is fairly constant. 8

1.2 Schematic of a DM soliton fiber laser with intracavity dispersion map and pulse evolution. 10

1.3 Self-similar evolution in (a) passive fiber (b) active fiber. 12

1.4 Schematic of a passive self-similar laser along with its dispersion map and intracavity pulse evolution. 12

1.5 Schematic of a soliton-similariton fiber laser with dispersion map and intracavity pulse evolution. 13

1.6 Schematic of an active self-similar laser without any anomalous dispersion component. Intracavity pulse evoluton is shown with the gain being a very strong attractor. 14

1.7 Schematic of the ANDi fiber laser with dispersion map and intracavity pulse evolution. 16

1.8 Schematic of a Mamyshev oscillator. 18

1.9 Working principle of a saturable absorber where T: transmittance of the saturable absorber and I: incident intensity. 19

1.10 Nonlinear polarization based saturable absorber. 20

1.11 (a) Birefringent plate based spectral filter (b) Calculated filter transmission profile for the birefringent plate filter with the plate thickness d = 7.5 mm. 21

1.12 An all-fiber Lyot Filter (a) schematic of the filter (b) Calculated transmission profile with the PM fiber length = 14.75 cm. P: in-line polarizer. 23

1.13 Schematic of a Fabry-Perot bandpass filter. The incident angle is denoted by θ. 24

1.14 Recorded transmission of an interference filter at the central wavelength of 1030 nm (T1), 1028 nm (T2) and 1026 nm (T3) by tuning the angle of the filter with respect to the incident beam. As the center wavelength deviates from 1030 nm, the transmission curve exhibits complex structures. 25

1.15 Schematic of a grating-collimator filter. 26

1.16 Cross-section of a DC fiber with offset core. 28

1.17 Schematic diagram of a cladding pumped double-clad fiber laser [27]. 28

1.18 Comparison between uncoated a) standard SMF and b) LMA fiber. The dark blue circle represents core. 29

1.19 Types of PM fibers a) PANDA fiber b) bow-tie fiber. The dark blue circle represents the core while dark gray features are the stress elements. 30

1.20 Types of PCFs a) high index PCF [29] b) low index PCF [30]. 31

2.1 Schematic of twisted fiber based spectral filter. P: polarizer, PM: polarization maintaining fiber, L1: unrotated, non-twisted PM fiber, L2: twisted PM fiber with ϕ as a twist angle, L3: rotated PM fiber. The arrows indicate parts under rotation. 35

2.2 Twisted fiber filter results (a) calculated transmission spectra of the filter for different twist angles, $\phi = 0$ ° (blue curve) and $\phi = 45$ ° (red curve), respectively (b) measured experimental transmittance with different twist angles. 37

2.3 Schematic of fiber based spectral filter. P: polarizer, PC: polarization controller, PM: polarization maintaining fiber, SMF: single mode fiber. 38

2.4 Calculated transmission spectra of the filter for different angles of rotation of polarization inside the SMF, namely, $\phi = 45.8°$ (red curve) and $\phi = 10°$ (blue curve). The values for the birefringence assumed are $\Delta n_1 = \Delta n_3 = 3.6 \times 10^{-4}$ and $\Delta n_2 = 3.8 \times 10^{-6}$ for the PM fibers and the SMF, respectively. 39

2.5 Calculated transmission spectra of the PM1-SMF1-PM2-SMF2-PM3 filter with FWHM BW of 4 nm (blue curve), 8 nm (red curve) and 17.5 nm (dotted black curve), respectively. 40

2.6 The experimental set-up of the fiber laser. PC: polarization controller, HWP:Half waveplate, QWP: Quarter Waveplate, PBS: Polarizing beam splitter. 41

2.7 The experimental (a) ASE (b) transmission spectra of wideband (red curve) and narrowband (blue curve) filter at different settings of PC1 (c) theoretical (dashed line) and experimental (solid line) transmittance of wideband filter (d) theoretical (dashed line) and experimental (solid line) transmittance of narrowband filter. 42

2.8 Experimental (a) spectrum at the PBS at 350 mW input pump power. (b) spectrum at the 20% port. (c) radio frequency spectrum; f_R: repetition frequency, RBW: resolution bandwidth. (d) Interferometric AC. 44

2.9 Experimental (a) spectrum at the PBS at 220 mW input pump power (b) spectrum at the 20% port (c) AC for the spectrum in (a) (d) RF spectrum showing sidebands as the evidence of multipulsing (e) spectrum at the PBS at 350 mW input pump power (f) AC for the spectrum in (e). 45

2.10 Calculated transmission spectra of (a) wideband filter and (b) narrowband filter as a function of temperature. Black, red and blue curves denote the transmission spectra at room temperature, 1 °C, and 2 °C rise in temperature, respectively. 47

3.1 Schematic of fiber based spectral filter. P: polarizer, PC: polarization controller, PM: polarization maintaining fiber, SMF: single mode fiber. 52

3.2 Simulated transmission spectra of the filter. The calculated birefringence values for the PM fibers are $\Delta n_1 = \Delta n_3 = \Delta n_5 = 3.6 \times 10^{-4}$. Birefringence values for SMFs (Δn_2 and Δn_5) and the rotation angles (Θ_1 and Θ_2) are variable. . . . 52

3.3 The experimental set-up of the fiber laser. PC: polarization controller, HWP: Half waveplate, QWP: Quarter Waveplate, PBS: Polarizing beam splitter. . . . 53

3.4 Output spectrum of the spectral filter with ASE (dashed line) as input. The inset shows experimental transmittance of the spectral filter. 54

3.5 Experimental data for the harmonic mode-locking (a) mode-locked spectrum (b) spectrum at the 20% port (c) long range pulse train (d) short range pulse train (e) RF spectrum; span: 500 MHz, RBW: 1 kHz (f) autocorrelation. 55

3.6 Experimental data for the fundamental mode-locking (a) short range pulse train (b) long range pulse train (c) RF spectrum; span: 200 MHz, RBW: 1 kHz (d) RF spectrum over 1 MHz span (e) mode-locked spectrum (f) spectrum at the 20% port. 57

3.7 Output spectrum of the filter with ASE as input. Inset shows the change in the transmittance of the filter. 58

3.8 Experimental data for the soliton bunch mode-locking (a) short range pulse train (b) mode-locked spectrum at the PBS at 650 mW input power (c) spectrum at 20% port (d) spectral filter output with ASE as input (e) transmittance of the spectral filter. 59

3.9 Dissipative soliton bunch with hybrid pulse separation of (a) 170 ps and 110 ps (b) 120 ps and 285 ps 60

3.10 Experimental data for the non-periodic mode-locked pulses (a) long range pulse train (b) short range pulse train (c) mode-locked spectrum (d) spectrum at the 20% port (e) output spectrum of the spectral filter with ASE as input (f) Comparison of the spectral filter transmittance. 61

4.1 Schematic of the fiber oscillator along with the pulse characterization system. PBS, polarizing beam splitter; BPF, bandpass filter; HWP, half wave plate; P, in-line polarizer; PM, polarization maintaining; SMF, single mode fiber; PC, polarization controller; WDM, Wavelength Division Multiplexer; QWP, quarter waveplate; BS, beam splitter; DDL, dispersion delay line; M, filp mirror. . . . 65

4.2 Spectral filter transmission $T(\omega) = e^{(\delta-\beta\omega^2-\gamma\omega^4)}$ in the CQGLE model (dashed curve) with $\delta = 0$, $\beta = 0.012$ and $\gamma = 0$ and in the CSHE model (Solid curve) with $\delta =$ - 0.7133, $\beta =$ -0.0809 and $\gamma = 0.0023$ 68

4.3 Numerical simulation results (a) pulse evolution in the presence of the spectral filter with respect to roundtrips (b) The pulse energy after spectral filter along with round trip propagation for the laser cavity. The convergence to a steady state is achieved at N=20. (c)The steady state evolution after each component inside the cavity. Top row: the shape of the pulse. The pulse is asymmetric and moving. Center row: the spectral evolution. The spectrum at each location in the cavity is asymmetric. Bottom row: The chirp associated with the pulse. The chirp shows a clear sign of wavebraking at the edges of the pulse. 69

4.4 Numerical simulation results (a) asymmetric mode-locked spectrum (dashed blue curve) pertaining to the moving pulse solution in the first simulated case and more asymmetric mode-locked spectrum (solid black curve) related to different simulation parameters. The inset shows the asymmetry at the longer wavelength tail of the spectra (b) comparison with the two pulse profiles (c) temporal dynamics of the moving pulse solution related to the less asymmetric mode-locked spectrum pertaining to the first simulated case (d) amplitude contour plot for the pulses moving with a higher velocity associated with the more asymmetric spectrum. 71

4.5 Output of the fiber based filter and BPF combination (solid curve) with ASE (dashed line) as input. The dotted line depicts the output of fiber based filter only. 72

4.6 Experimental dataset recorded at 545 mW of input pump power (a) mode-locked spectrum at the PBS (solid curve) along with the spectral filter response (dashed curve) (b) spectrum obtained at the 20 % port of the fiber coupler (c) cross-correlation of the output pulse (d) pulse train (e) RF spectrum (f) autocorrelation. 74

4.7 Experimental dataset recorded at 571 mW of input pump power a) mode-locked spectrum with a spectral filter response (dashed curve) (b) cross-correlation of the output pulse (c) spectrum obtained at the 20 % port of the fiber coupler (d) autocorrelation. 75

4.8 Comparison between the two experimental datasets (a) asymmetry comparison between the two mode-locking states. The blue curve (spectrum 1) depicts the spectrum for the mode at 545 mW input pump power while the green curve (spectrum 2) denotes the spectrum for the mode measured at 571 mW. (b) repetition rate comparison between the two spectra. 76

4.9 Additional experimental dataset (a) spectral filter response (b) output spectrum through PBS (c) spectrum at the tap port (d) autocorrelation (e) cross-correlation. 78

4.10 Modified laser cavity setup where BS: Beam Sampler 79

4.11 Spectra at the indicated locations in the cavity (a) location A: tap port output (b) location B: After SA (c) location C: NPE ejection port (d) location D: sampled beam by the beam sampler (e) cross-correlation for the pulse at location C. 80

5.1 Schematic of the tunable fiber oscillator. PBS, polarizing beam splitter; HWP, half waveplate; QWP, quarter waveplate; SMF, single mode fiber. 85

5.2 Effect of temperature on a) mode-locked spectrum at 1100 nm without heating the gain fiber (b) mode-locked spectrum at 1100 nm with heating up the gain fiber to 125° C. 87

5.3 Experimental dataset 1 (a) tuned mode-locked spectra (b) AC (c) the pulse duration and BW versus the laser center wavelength (d) the pulse energy versus the laser center wavelength. 88

5.4 Experimental dataset 2 (a) tuned mode-locked spectra (b) AC (c) the pulse duration and BW versus the laser center wavelength (d) the pulse energy versus the laser center wavelength. 90

6.1 Conceptual schematic of the laser in [115]. SMF, single mode fiber; YDF, ytterbium doped fiber; PCF, photonic crystal fiber; SA, saturable absorber; SF, spectral filter. 93

6.2 Conceptual schematic of the self-similar laser. SMF, single mode fiber; YDF, ytterbium doped fiber; DDL, dispersion delay line; PCF, photonic crystal fiber; SA, saturable absorber; SF, spectral filter. 94

6.3 Simulation results a) octave spanning spectra. Inset shows the transform limited pulse duration b) Output pulse and corresponding chirp c) Evolution of pulse duration and spectral bandwidth through laser cavity. The spectral breathing ratio can be as large as ~ 86. 96

6.4 Experimental DC laser cavity. SMF, single mode fiber; HWP, half waveplate; QWP, quarter waveplate; PBS, polarizing beam splitter. 97

6.5 Experimental DC laser cavity results (a) output spectrum (b) autocorrelation. 98

6.6 Experimental laser cavity. HWP, half waveplate; QWP, quarter waveplate; PBS, polarizing beam splitter; DDL, dispersion delay line; PCF, photonic crystal fiber; L1, focusing lens; L2, collimating lens. 99

6.7 Experimental results a) Output spectrum b)Dechirped autocorrelation c) Calculated Fourier transform limited pulse profile. 100

7.1 Energy level diagram of Pr^{3+}. 105

7.2 Pr doped fiber emission spectrum. 108

7.3 Conceptual schematic of the Pr doped ANDi fiber laser. SA, saturable absorber; SF, spectral filter. 109

7.4 Mode-locked Pr doped ANDi fiber laser simulation results at 520 nm a) simulated output spectrum b) dechirped output pulse 110

7.5 Mode-locked Pr doped AS fiber laser simulation results at 520 nm a) simulated output spectrum b) dechirped output pulse 110

7.6 Mode-locked Pr doped AS fiber laser simulation results at 605 nm a) simulated output spectrum b) dechirped output pulse (~ 150 fs) 111

7.7 Mode-locked Pr doped AS fiber laser simulation results at 605 nm a) simulated output spectrum b) dechirped output pulse (~ 200 fs) 112

7.8 Conceptual schematic of the Pr doped modified AS fiber laser. PCF, photonic crystal fiber; SA, saturable absorber; SF, spectral filter. 112

7.9 Mode-locked Pr doped modified AS fiber laser simulation results at 635 nm a) simulated output spectrum b) dechirped output pulse (~ 350 fs). 113

7.10 Proposed experimental mode-locked Pr doped ANDi fiber laser. DM, dichroic mirror; L, lens; M, mirror; HWP, half waveplate; QWP, quarter waveplate; PBS, polarizing beam splitter; SF, spectral filter. 114

7.11 Measured far field pattern of NDB7K75. 115

7.12 Pump coupling optics configuration (a) using concave-convex cylindrical lens configuration (b) modified 4f system. 117

7.13 Pr: WPFG fiber with zirconia ferrule (L=105 mm). The inset shows the polished fiber end viewed through microscope. 118

7.14 Pr: WPFG fiber with zirconia ferrule (L=105 mm). The inset shows the polished fiber end viewed through the microscope. 119

7.15 Experimental linear CW Pr:WPFG fiber fiber laser cavity. DM, dichroic mirror; L, lens; M, mirror; PBS, polarizing beam splitter 120

7.16 Linear CW Pr,Yb: ZBLAN fiber fiber laser cavity. DM, dichroic mirror; L, lens; M, mirror; PBS, polarizing beam splitter. 121

7.17 CW oscillation at 635 nm for Pr,Yb: ZBLAN fiber laser. Unabsorbed pump at 442 nm is seen. 122

7.18 Experimental 635 nm Pr: ZBLAN CW fiber laser linear cavity. DM, dichroic mirror; L, lens; M, mirror; PBS, polarizing beam splitter; HWP, half waveplate; QWP, quarter waveplate (a) schematic (b) photograph. 123

7.19 Pr: ZBLAN fiber laser dataset (a) CW oscillation at 635 nm. Inset shows the close-up view of the optical spectra (b) input-output characteristics as a function of threshold absorbed pump power. 124

7.20 Connectorized Pr: ZBLAN fiber. The inset shows the polished fiber end viewed through a fiber microscope. 125

7.21 Experimental 635 nm Pr: ZBLAN CW fiber laser ring cavity. DM, dichroic mirror; L, lens; M, mirror; PBS, polarizing beam splitter; HWP, half waveplate; QWP, quarter waveplate (a) schematic (b) photograph. 126

7.22 Input-output power characteristics as a function of absorbed pump power for 635 nm Pr:ZBLAN fiber ring oscillator 127

8.1 Measured (a) spectral filter output (b) noise mode-locked spectra (c) intensity autocorrelation of NLP. Inset shows short range interferometric autocorrelation (d) pulse train for NLP (upper row) and ANDi mode-locking (lower row). . . . 133

8.2 Measured (a) spectral filter output (b) dual mode-locked spectra. 134

8.3 Measured (a) mode-locked spectra (b) spectral filter output (c) autocorrelation (d) pulse train. 135

8.4 Conceptual schematic of the Yb doped fiber laser with a higher order spectral filter. SMF, single mode fiber; SA, saturable absorber; SF, spectral filter. . . . 136

8.5 Higher order spectral filter transmission (pink curve) compared with a Gaussian spectral filter transmission (black curve) with approximately same FWHM. . . 137

8.6 Simulated mode-locked spectra for a fiber laser with a three peak spectral filter transmission profile after (a) SMF-I (b) gain (c) SMF-II (d) SA (output) (e) SF. 138

8.7 Simulated pulse for a fiber laser with a three peak spectral filter transmission profile after (a) SMF-I (b) gain (c) SMF-II (d) SA (output) (e) SF. 139

8.8 Simulation results for a fiber laser with (a) a complicated spectral filter transmission profile (b) output spectrum (c) output pulse. 140

A.1 Dispersion parameter distribution with respect to wavelength 155

A.2 GVD distribution with respect to frequency 156

A.3 Curve fitting window for the plot of GVD Vs frequency 156

B.1 Refractive index vs. wavelength for Pr:ZBLAN fiber 159

B.2 Material dispersion parameter for Pr:ZBLAN fiber 159

LIST OF TABLES

6.1 Parameters used for the numerical simulation 95

7.1 Parameters used for the numerical simulation of mode-locked Pr-doped ANDi fiber laser 109

7.2 Parameters used for the numerical simulation of mode-locked Pr doped modified AS fiber laser 113

7.3 Pr doped fiber specifications 116

A.1 Dispersion terms for the PCF 157

B.1 Sellmeier cofficient for Pr doped fiber 158

B.2 GVD cofficient for Pr doped ZBLAN fiber 160

CHAPTER I

INTRODUCTION

'To measure an event in time, one must use a shorter one' and this necessity led to the development of sources that can produce ultrashort pulses of light. A pulse is called an ultrashort or ultrafast if its time duration is of the order of a picosecond (10^{-12} second) or less. Lasers are the building blocks to generate ultrafast pulses which can then be used for measuring the short-lived processes in the field of physics, chemistry, and biology. Concurrently, the ultrafast lasers have ample industrial applications like material processing and the healthcare industry.

In the early 1990s, titanium doped sapphire (Ti:Sapphire) lasers became a popular tool for ultrafast pulse generation. Exceptional lasers and amplifiers were possible because of the huge gain bandwidth and other material properties of Ti:Sapphire. Even today, Ti: Sapphire lasers find its usage in scientific laboratories. In spite of the excellent performance, Ti:Sapphire lasers were not widely deployed commercially because of their size, complexity, poor stability and most importantly their cost. Mode-locked fiber lasers, on the other hand, are often utilized as a source of ultrafast pulses, since they have practical advantages of low cost, compactness, excellent beam quality, high average power, and stability. Because of these qualities ultrafast fiber lasers have been making continuous progress and expansion in their applications. Currently, there are more than 25 companies alone in the United States selling short-pulse fiber lasers for a range of applications, from micromachining, medical imaging, to precision metrology.

In the case of ultrafast fiber lasers, self-consistent pulses are formed as a result of several physical processes that act on the pulse envelope such as group-velocity dispersion (GVD), self-phase modulation (SPM), and amplitude modulation caused by a saturable absorber

(SA) and spectral filtering effect provided by gain bandwidth and also by a dedicated spectral filtering component introduced in the cavity.

The most common femtosecond (fs) lasers are based on soliton pulse formation when the operating wavelengths are greater than 1.3 μm. The pulse formation results from the balance between the phase shifts offered by GVD and SPM. The main disadvantage is that the pulse energy of soliton lasers is limited by the soliton area theorem. For wavelengths less than 1.3 μm, silica fibers have normal dispersion. Optical components like grating pairs, prism pairs, chirped mirrors or dispersion engineered fibers can add anomalous dispersion in the silica fiber laser cavities. This can make the average cavity dispersion anomalous and therefore allow the cavity to support soliton-like pulse formation. This principle gave birth to a new class of ultrafast fiber lasers called stretched pulse lasers or dispersion managed soliton lasers which could emit nanojoule (nJ) energy pulses. But dispersion managed solitons are not the only way to build mode-locked lasers at normal dispersion. Self-similar evolution and spectral filtering of chirped pulses are the other two mechanisms for building ultrafast fiber lasers at normal dispersion. Both the mechanisms rely on the use of a spectral filter to achieve a self-consistent pulse solution of the laser cavity. The development of these two types of lasers have revolutionized the world of high energy ultrafast fiber lasers. Recently, a fiber laser design called Mamyshev oscillator was developed at normal dispersion, the performance of which is now comparable with solid-state lasers. The Mamyshev oscillator can be considered as a cascaded self-similar fiber laser with offset spectral filters. Thus, the role of spectral filter in the performance of mode-locked fiber lasers is very crucial and this dissertation is the investigative report of the same. Recently, there is a growing interest in fiber based spectral filters as they facilitate construction of all-fiber laser oscillators. This dissertation explores a fiber based, tunable bandwidth, spectral filter in detail which can offer flexibility in the mode-locked output of a fiber laser. Further, the same spectral filter is used to control the multipulsing states of a fiber laser. Conventionally, the spectral filters used in the ultrafast fiber lasers have quadratic (single peak) response in the frequency domain. There are numerous possibilities proven theoretically if a fourth order (double peak) spectral filter is utilized in the cavity. So far, such filter is rarely implemented in a fiber laser. But our fiber based filter design facilitates the use of a fourth order spectral filter in the cavity which led to the discovery of a new type of dissipative solitons. We believe that this will open a new course in ultrafast fiber lasers research. Furthermore, in this dissertation a grating based spectral filter in self-similar evolution based fiber lasers is also studied to construct a tunable mode-locked fiber laser. Also, the concept of intracavity supercontinuum generation based on self-similar fiber lasers and Mamyshev oscillators is investigated. Offset spectral filtering in the Mamyshev oscillator along with an intracavity photonic crystal fiber (PCF) is built which results in the generation of the shortest pulse to date from an ytterbium (Yb) oscillator. Most of the work in this dissertation utilizes Yb as a gain medium but an attempt is also made to build a mode-locked fiber oscillator using praseodymium (Pr) as a gain medium at visible wavelengths. Although these experiments are met with a little success, they are included in this report as they have a potential to guide future development of ultrafast fiber lasers at visible wavelengths.

1.1 Original contributions and publications

- Design of an all-fiber tunable bandwidth (BW) spectral filter - Presented at 2019 Conference on Lasers and Electro-Optics (CLEO) [1]
- Implementation of the tunable BW filter in an all-normal dispersion (ANDi) fiber laser to generate distinct laser modes with different output spectral shapes and pulse evolutions - Results published in Optics Letters [2]
- Controlling multipulse dynamics of a fiber laser with the use of a simple spectral filter - Results published in Optics Letters [3]
- Demonstration of the Complex Swift Hohenberg Equation based dissipative soliton fiber laser - Results presented at 2021 CLEO Conference as well as published in Photonics Research [4]
- Simulation producing octave spanning spectra directly from Yb oscillator - Results presented at 2018 CLEO Conference [5]
- Constructing praseodymium doped ZBLAN fiber laser

1.2 Organization of thesis

Chapter I describes the basics of mode-locked lasers such as nonlinear Schrodinger equation and the pulse shaping mechanisms involved in different types of the mode-locked fiber lasers. Also, a summary of different components used in fiber lasers such as SA, spectral filter and various optical fibers is also included in Chapter I.

Chapter II investigates numerically and experimentally an all-fiber, bandwidth tunable spectral filter comprising birefringent fibers. This spectral filter is used in an Yb oscillator to generate distinct laser modes with different output spectral shapes and pulse evolution and those results are included in this chapter.

Chapter III reports an experimental study of multipulsing states in an Yb fiber laser using the modified design of the birefringent spectral filter described in Chapter II. The evidence of various multipulsing states such as harmonic mode-locking, soliton bunches, and non-periodic pulses are observed by tuning the spectral filter.

Chapter IV addresses the importance of realizing the complex Swift Hohenberg equation (CSHE) based fiber laser. It presents numerical simulation results for CSHE based Yb fiber laser. It also provides an experimental laser configuration which can act as a testbed to analyze these dissipative solitons and the key role played by the fiber based spectral filter is explained. As this is a pulse shaping mechanism based on a non-trivial spectral filter, possible new directions that can be pursued regarding this research are described in detail.

In Chapter V, the emphasis is on a self-similar fiber laser containing a sharp spectral filter. This chapter documents the experimental study of central wavelength tunabilty of Yb doped self-similar mode-locked fiber laser and this tunability is attributed to the narrow intracavity spectral filter.

Chapter VI describes numerical simulation results for ultrafast pulse generation from a self-similar laser with a very narrow intracavity spectral filter and PCF. The difficulties in experimentally realizing this design, led to the alternative design consisting of a Mamyshev oscillator with offset spectral filters and an intracavity PCF. The successful numerical and experimental results depicting generation of 17 fs pulses from an Yb oscillator are presented in this chapter.

Chapter VII dives into a complete different subject of building a mode-locked fiber oscillator at visible wavelengths. Here, Pr doped ZBLAN fiber was used to construct the oscillator. The promising numerical simulation results, as well as primitive experimental results, are presented here.

In Chapter VIII, future directions in terms of ultrafast fiber lasers are suggested.

1.3 Nonlinear Schrödinger equation

The nonlinear Schrödinger equation (NLSE) is the basic equation that governs the propagation optical pulses in optical fibers. The starting point to derive this equation is the electromagnetic wave equation and several simplifying assumptions are considered. The derivation can be found in [6]. The solutions of NLSE provide a deep understanding of the pulse propagation over the fibers. The equation for the nonlinear pulse propagation is given by

$$\frac{\partial A}{\partial z} = -\frac{\alpha}{2} - i\beta_2\frac{\partial^2 A}{\partial T^2} + i\frac{1}{6}\beta_3\frac{\partial^3 A}{\partial T^3} + i\gamma\left[|A|^2A + \frac{i}{\omega_0}\frac{\partial}{\partial T}|A|^2A - T_R A\frac{\partial |A|^2}{\partial T}\right] \tag{1.1}$$

where A is the normalized complex envelope of the optical field, z is the propagation distance and T is the retarded time. α acts as a gain or loss coefficient. $\beta(\omega)$ represents the propagation constant and origin of β_2 and β_3 in Equation 1.1 lies in the expansion of $\beta(\omega)$ via Taylor series about the carrier frequency ω_0 and it is given by

$$\beta(\omega) = \beta_0 - \beta_1(\omega-\omega_0) + \frac{1}{2}\beta_2(\omega-\omega_0)^2 + \frac{1}{6}\beta_3(\omega-\omega_0)^3 + ... \tag{1.2}$$

β_2 is called as a GVD parameter, β_3 is called as a third order dispersion (TOD) parameter, so on and so forth. The cubic and higher order dispersion effects are neglected if the spectral width is negligible than the carrier frequency, in other words, if pulse width $\geq$ 0.1 ps. If

β_2=0 for some specific ω_0 (in case of a zero dispersion wavelength of the fiber), it is necessary to include β_3. Hence, most of the cases of pulse propagation only β_2 is considered. γ is nonlinearity coefficient and is defined by

$$\gamma = \frac{n_2 \omega_0}{c A_{eff}} \tag{1.3}$$

where n_2 is nonlinear refractive index coefficient and A_{eff} is effective mode area. The quantity $i\gamma|A|^2A$ is called self-phase modulation. The terms $\frac{i}{\omega_0}\frac{\partial}{\partial T}|A|^2A$ and $T_R A\frac{\partial |A|^2}{\partial T}$ represent high order nonlinear effects namely self-steepening and Raman effects. Again, for the pulses of width greater than 0.1 ps, these higher order nonlinear effects can be neglected. In the case of α =0, Equation 1.1 is simplified and gets translated to well known NLSE and it is given by

$$\frac{\partial A}{\partial z} = -i\beta_2 \frac{\partial^2 A}{\partial T^2} + i\gamma |A|^2 A \tag{1.4}$$

1.4 Soliton solution of NLSE

An interesting solution to Equation 1.4 is possible when $\beta_2 < 0$ (anomalous dispersion) and positive nonlinearity (self-focusing). The phase shift due to the GVD and the SPM cancel each other and the pulse propagates without distortion. Such a solution is called a soliton. Soliton propagation in optical fiber was first predicted by Hasegawa *et al.* [7]. The analytical solution of this equation is a pulse with hyperbolic-secant intensity profile given as

$$A(z,T) = A_0 Sech\left(\frac{T}{T_0}\right) e^{\left(\frac{iz}{2}\right)} \tag{1.5}$$

The amplitude A_0 of the fundamental soliton is a function of β_2, γ and T_0 and the relation is expressed as

$$A_0 = \sqrt{\frac{|\beta_2|}{\gamma T_0^2}} \tag{1.6}$$

Equation 1.6 gives rise to a simple relation $A_0 T_0 =$ constant which is known as the soliton area theorem [7, 8]. It means that for a given pulse duration, the soliton energy is fundamentally limited. Whenever the accumulated nonlinear phase shift is too large to be balanced by the pulse dispersion, it leads to pulse breaking.

Since the fundamental soliton does not change its shape while it propagates, a soliton is a good candidate for pulses shaping mechanism in mode-locked fiber lasers. The first soliton laser was demonstrated experimentally by Mollenauer in 1984 using anomalous dispersion fibers [9]. The soliton fiber laser (Figure 1.1) typically consists of an anomalously dispersive fiber, a gain fiber which is also anomalously dispersive with positive nonlinearity and a SA. A SA is important to start the pulse formation but once soliton is formed, SA acts as a

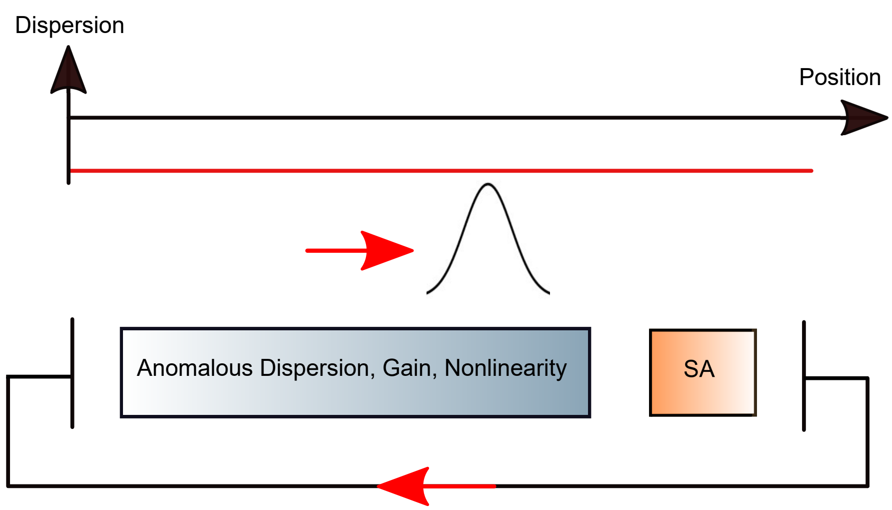

Figure 1.1: Schematic of a soliton fiber laser along with its dispersion map. The intracavity pulse shape is fairly constant.

small perturbation during each round trip. The function of SA in a mode-locked laser is explained in detail in Section 1.9. To start with, a soliton is formed as a natural solution of NLSE across anomalously dispersive fiber, propagates without distortion, encounters gain, gets amplified, suffers losses through SA and output coupling. After the output coupling, the remaining pulse goes back inside the cavity, evolves into a soliton again. The soliton fiber lasers are good for generating ultrafast pulses. However, the pulse energy from a soliton fiber laser is limited as explained earlier by the soliton area theorem (Equation 1.6). As a result, the typical pulse energies from fiber lasers are limited to ~ 0.1 nJ.

1.5 Dispersion managed soliton

Another important pulse in a fiber laser is the dispersion managed (DM) soliton. A DM soliton fiber laser consists of alternating segments of anomalous and normal dispersion. In such a dispersion map, the resulting pulse breathes (stretches and compresses) during one round trip. This fiber laser cavity shown in Figure 1.2 consists of a normally dispersive fiber and an anomalously dispersive fiber or component, with the net cavity dispersion close to zero. Again, SA is critical to start the operation of the laser. The pulse inside the cavity experiences two minima durations per round trip. The chirp across the pulse changes the sign twice per round trip. Because the chirp varies throughout the laser cavity, the output pulse usually has to be dechirped, unlike a soliton fiber laser. Tamura *et.al* [10] demonstrated this type of laser for the first time and called it a stretched pulse laser because of stretched pulse evolution inside the cavity. Again, the pulse forming mechanism is soliton-like in the anomalous dispersion segment. As pulses breathe, the nonlinear effects are reduced by increasing the average pulse duration and therefore, the pulse energy that can be obtained from DM fiber lasers is higher than soliton lasers (up to 1 nJ).

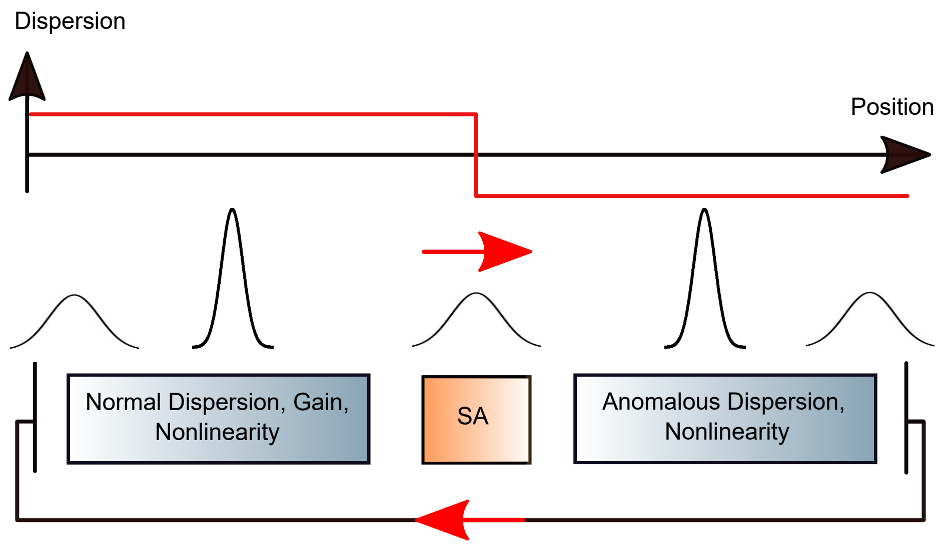

Figure 1.2: Schematic of a DM soliton fiber laser with intracavity dispersion map and pulse evolution.

1.6 Similaritons

In 1993, Anderson *et al.* showed that wave-breaking free pulses were possible in optical fibers with normal GVD and strong nonlinearity. They showed that pulses that had quadratic temporal distribution (parabolic pulses) with quadratic temporal phase (linear frequency chirp) can tolerate strong nonlinearity and will never experience wave-breaking unlike solitons [11]. Following this key point, Tamura and Nakazawa showed numerically that the self-similar evolution resulted in wave-breaking free pulses in normal dispersion fiber amplifier [12]. This predicted evolution was experimentally verified in the subsequent years by Fermann *et.al* in an Yb doped fiber amplifier with normal dispersion at 1 μm [13]. Apart from experimental evidence, they also provided theoretical analysis on the basis symmetry reduction to the NLSE with gain which is given as

$$\frac{\partial A}{\partial z} = \frac{g}{2}A - i\beta_2\frac{\partial^2 A}{\partial T^2} + i\gamma|A|^2 A \tag{1.7}$$

and the solution to this equation is a pulse with parabolic intensity profile

$$A(z,T) = \begin{cases} A_0(Z)\sqrt{1-(\frac{t}{T(z)})^2} & \text{if } |T| \leq T(z) \\ 0 & \text{if } |T| > T(z) \end{cases} \tag{1.8}$$

Such a pulse maintains its shape and is always a scaled version of itself which means it evolves self-similarly. Ferman demonstrated that a self-similar parabolic pulse is a strict asymptotic solution to NLSE with gain (given by Equation 1.7), indicating a kind of non-linear attractor towards which any arbitrarily shaped input pulse with a given energy would converge with sufficient distance. These self-similar pulses gained a popular name as 'similaritons' because of their closeness with the well known solitary wave behavior of solitons. This pulse forming mechanism is a good candidate for mode-locked fiber lasers since the pulse does not experience wave-breaking. Furthermore, as the similariton does not break up even at a very large nonlinear phase shift, a similariton fiber laser is expected to have much higher pulse energies.

1.6.1 Passive similariton

For building a similariton laser one might use the working prinicple of the similariton amplifier but spectral bandwidth increases monotonically in self-similar amplification, therefore, spectral filtering or spectral compression becomes necessary to restore original condition after each roundtrip. Ilday *et al.* demonstrated the first self-similar fiber laser using the above approach and it was based on self-similar evolution in passive fiber segment [14] shown in Figure 1.3(a). The schematic of this passive similariton laser is shown in Figure 1.4. The prominent pulse evolution takes place in the lengthy single mode fiber (SMF). The Yb gain fiber is kept short to avoid amplifier similariton formation. The gain fiber is followed by SA which initiates the mode-lock and also serves as an output port.

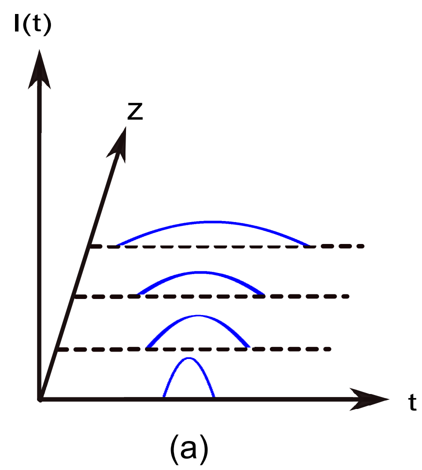

Figure 1.3: Self-similar evolution in (a) passive fiber (b) active fiber.

In the temporal domain, the accumulated chirp is compensated by dispersive delay line (DDL) and ensures a self-consistent solution before passing the pulses back into the SMF. In the frequency domain, the bandwidth generated is filtered by the gain medium to produce a self consistent solution in the resonator.

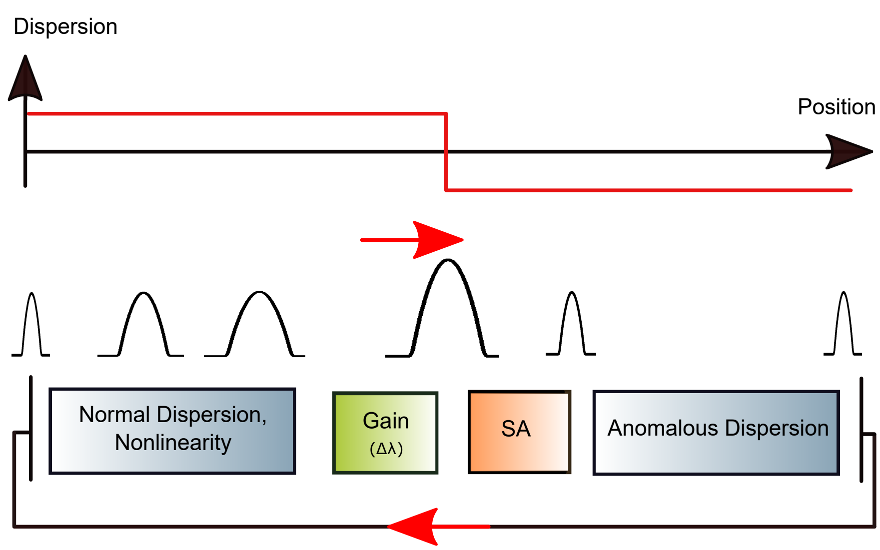

Figure 1.4: Schematic of a passive self-similar laser along with its dispersion map and intracavity pulse evolution.

1.6.2 Amplifier similariton

When the self-similar evolution occurs in the gain fiber, the resulting pulses are called amplifier similariton. The first demonstration of amplifier similariton laser was soliton-similariton laser where anomalous dispersion passive fiber was used to ensure self-consistency [15]. The laser schematic is shown in Figure 1.5. The erbium (Er) gain fiber has normal GVD where amplifier similariton is formed. The evolution in the gain fiber is illustrated by the Figure 1.3(b). A bandpass filter filters in both time and frequency domain due to the large chirp present. The pulse then evolves into a soliton in the long SMF segment with anomalous GVD. When the soliton re-enters the gain medium, it is shaped back into a similariton which is a strong attractor for any input pulse shape. The exciting result was presented by Renninger *et al.* where anomalous segment was not used at all [16]. Instead, a narrow spectral filter was used to stabilize the cavity. The long gain fiber helps the formation of amplifier similariton. The combination of a grating and fiber coupled collimating

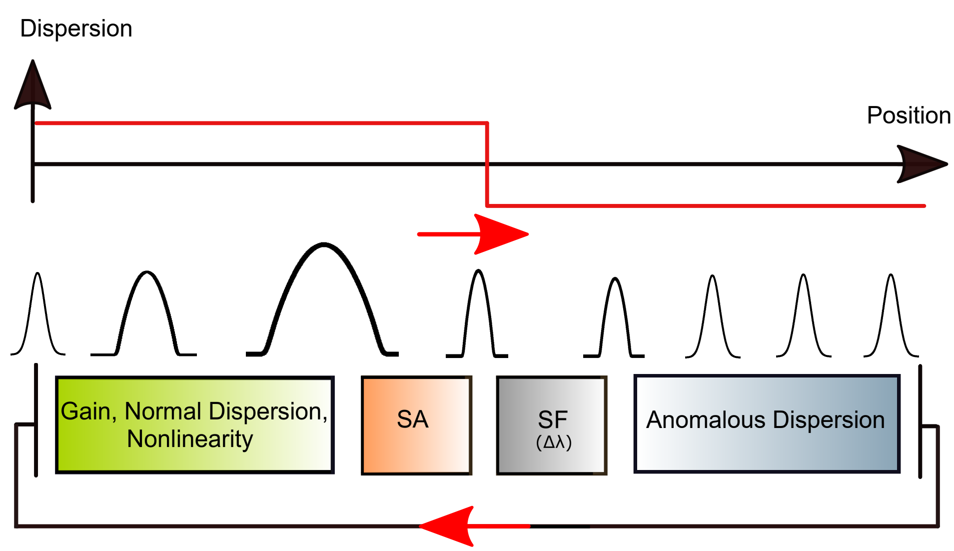

Figure 1.5: Schematic of a soliton-similariton fiber laser with dispersion map and intracavity pulse evolution.

lens formed the spectral filter. The laser schematic is given in Figure 1.6.

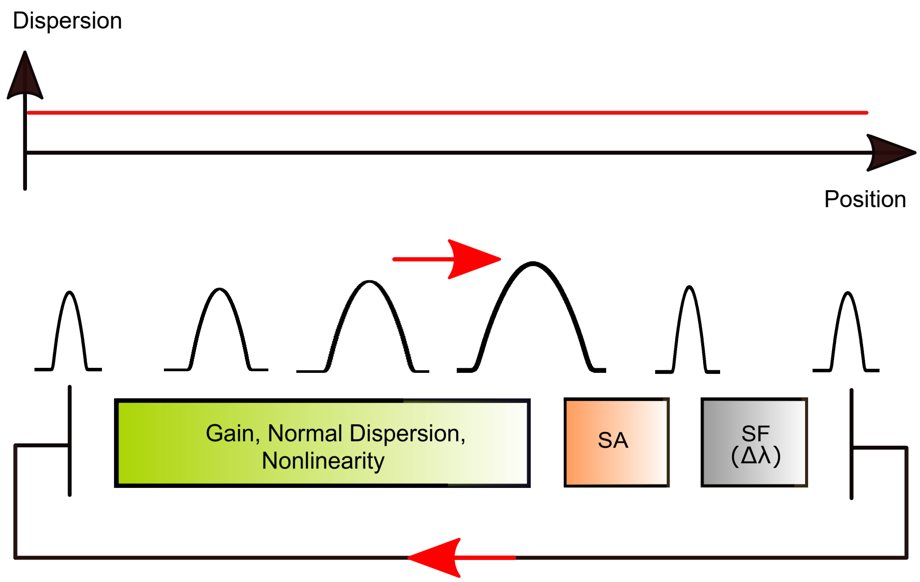

Figure 1.6: Schematic of an active self-similar laser without any anomalous dispersion component. Intracavity pulse evoluton is shown with the gain being a very strong attractor.

1.7 Ginzburg-Landau equation and dissipative solitons

NLSE can very well model the pulse propagation over the passive fiber. But a fiber laser has many components like gain, SA or a spectral filter. They offer amplitude modulation but NLSE considers only phase modulations offered by GVD and SPM. Therefore, more terms are added to NLSE to account for this amplitude modulation and to make the modelling of the laser cavity more realistic. The resulting differential equation is called a cubic Ginzburg Landau equation (CGLE) and is expressed as

$$\frac{\partial A}{\partial z} = gA + \left(\frac{1}{\Omega} - i\frac{\beta_2}{2}\right)\frac{\partial^2 A}{\partial T^2} + (\alpha + i\gamma)|A|^2 A \tag{1.9}$$

where g is the net gain which is the combination of the gain of the gain fiber and the losses in the laser cavity such as output coupling. Ω is related to the spectral amplitude modulation. It could be due to the gain bandwidth or the intracavity spectral filter or the combination of both. α is the intensity dependent amplitude modulation term which is related to the SA. With all these extra terms CGLE accounts qualitatively for the behavior of mode-locked fiber lasers. The general solution of the CGLE is a chirped hyper secant pulse described by the Equation 1.10

$$A(z,T) = A_0 Sech\left(\frac{t}{T}\right) e^{i\beta ln\left(Sech\left(\frac{t}{T}\right)\right)+i\theta z} \tag{1.10}$$

The solution of the CGLE is a dissipative soliton which is a stable, localized structure which lasts for an extended period of time, even though the pulse experiences dissipative effects such as gain and loss of energy. As in the fiber laser cavity, pulses experience the dissipative processes through spectral filtering, saturable absorption as well as output coupling, it is safe to assume that the dissipative soliton is the solution of a fiber laser cavity.

1.8 Cubic Quintic Ginzburg-Landau equation and all-normal dispersion fiber laser

Chong *et al.* built a fiber laser for the first time with only normal dispersion components, hence the name all-normal dispersion fiber laser (ANDi) and it is illustrated schematically in Figure 1.7 [17]. The laser cavity is comprised of a normally-dispersive passive fiber followed by gain and another, shorter passive fiber. A spectral filter was the basis of the feedback loop. The output pulses from the laser were positively chirped and the output spectrum exhibited cat-ear peaks at the edges also called as batman spectrum. But numerical modelling of ANDi laser with CGLE was unsuccessful and always resulted in the rectangular flat top spectrum and no combination of initial pulse parameters would result in batman spectrum.

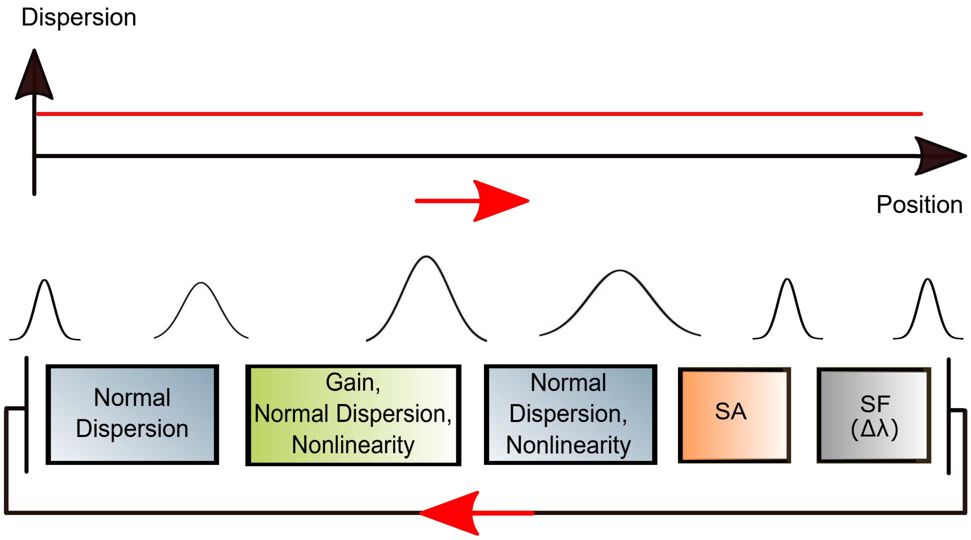

Figure 1.7: Schematic of the ANDi fiber laser with dispersion map and intracavity pulse evolution.

This difficulty was relived when a quintic term was added to the SA modelling and the resulting equation is called Cubic Quintic Ginzberg Landau Equation (CQGLE) which is given by

$$\frac{\partial A}{\partial z} = gA + \left(\frac{1}{\Omega} - i\frac{\beta_2}{2}\right)\frac{\partial^2 A}{\partial T^2} + (\alpha + i\gamma)|A|^2 A + \delta|A|^4 A \tag{1.11}$$

Where, $\delta|A|^4 A$ represents the quintic SA term. The general solution of CQGLE is unknown but it has a particular solution given by

$$A(z,T) = \sqrt{\frac{A}{Cosh(T) + B}} Sech\left(\frac{t}{T}\right) e^{i\frac{\beta}{2}ln\left(Cosh\left(\frac{t}{T}+B\right)\right)+i\theta z} \tag{1.12}$$

By varying the parameter B, it is possible to obtain a variety of spectra as a result of simulation including the batman spectrum matching to experimental spectra. Therefore, it is important to note that the CQGLE describes the operation of ANDi fiber laser better than CGLE. As ANDi fiber lasers can also tolerate high nonlinear phase accumulation, they can generate high energy ultrafast pulses, the top performance being 20 nJ, 200 fs pulses [18].

The question may arise about the differentiation between amplifier similariton and ANDi fiber laser operation. Like amplifier similariton, pulses are chirped throughout the cavity in ANDi lasers. But the striking difference between these two evolutions is the basis of the pulse shaping mechanism. Amplifier similariton is a local attractor in the gain segment while the ANDi laser pulse is not, it is rather a solution of the entire laser cavity. Also, the pulse breathing ratio in the self-similar type of cavities is much higher than that in ANDi laser cavities. In terms of the experiments, the only difference is that the amplifier similariton laser cavity uses a very narrow intracavity spectral filter (Full width half maximum (FWHM) of ~ 3 nm) while ANDi fiber laser utilizes a 10 nm FWHM bandwidth spectral filter. Also, the length of the gain fiber in amplifier similariton laser, plays an important role as the attractor is in the gain medium while in ANDi fiber laser, it does not.

Another perspective regarding all these different types ultrafast fiber lasers could be that as all of them have gain, loss, dispersion, gain bandwidth and SA, they should be modelled by CGLE/CQGLE and pulses should always be considered as dissipative solitons. Although this point of view is technically correct, it defies the principle behind the pulse formation. For soliton lasers, although a dissipative process like SA starts the pulse formation, phase modulations by GVD and SPM take the lead in establishing steady state solution and dissipative process, even though they exist, play a limited part. In the case of normal dispersion lasers, the basis of pulse formation is the spectral filtering of chirped pulses and dissipative effects are of comparable importance to phase modulations due to GVD and SPM.

1.9 Mamyshev Oscillator

Mamyshev oscillator is the newest type of ultrafast fiber laser which can provide a very high energy pulses, with megawatt peak power, an order magnitude higher than the previous fiber laser designs [19]. Although Regelskis *et al.* [20] and Samartsev *et al.* [21] were the first to demonstrate Mamyshev oscillator in the fiber format but the performance of their lasers was quite limited. Hence, the Mamyshev oscillator design by Liu *et. al.* stands out [19]. This oscillator design is based on the SPM induced spectral broadening and offset spectral filtering, as proposed by Mamyshev for optical signal regeneration in telecommunication systems [22] and its schematic is provided in Figure 1.8. Mamyshev oscillator can be thought of two self-similar arms, each with its own gain fiber, output coupler and offset spectral filter. The two non-overlapping spectral filters serve as an effective SA. An intense pulse experiences spectral broadening between each filter due to SPM. When this broadening is sufficient for significant pulse energy to pass through both spectral filters repeatedly, a stable, periodic evolution sets in.

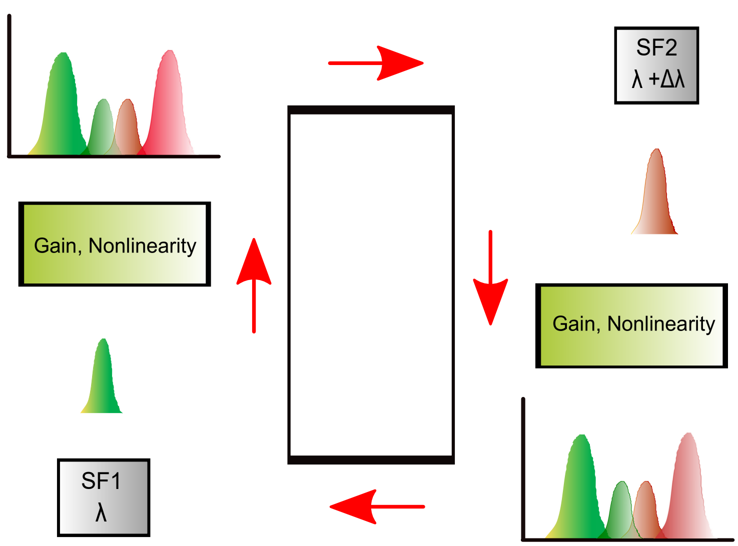

Figure 1.8: Schematic of a Mamyshev oscillator.

1.10 Saturable absorber

As described in earlier sections, SA is a vital component to initiate mode-locking. A SA is an element that exhibits a nonlinear loss which decreases as the incident light intensity increases as shown in Figure 1.9. Now in a laser, when a noisy electromagnetic field travels through a SA repeatedly in a cavity, a pulse with a high peak intensity and short duration is transmitted by SA and this serves as a start of mode-locking. There are multiple types of SA are available including semiconductor saturable absorber mirror (SESAM), carbon nanotubes (CNT), 2D materials, black phosphorous, nonlinear polarization evolution (NPE) based SA, etc. For all the experimental configurations mentioned in this dissertation, NPE based SA has been used. The NPE based SA configuration is shown in Figure 1.10. The light is first linearly polarized by the polarizer and then transformed into an elliptic polarization state by the quarter waveplate (QWP). Due to the Kerr nonlinearity of the fiber in the laser cavity, the polarization ellipse undergoes a rotation of its main axis proportional

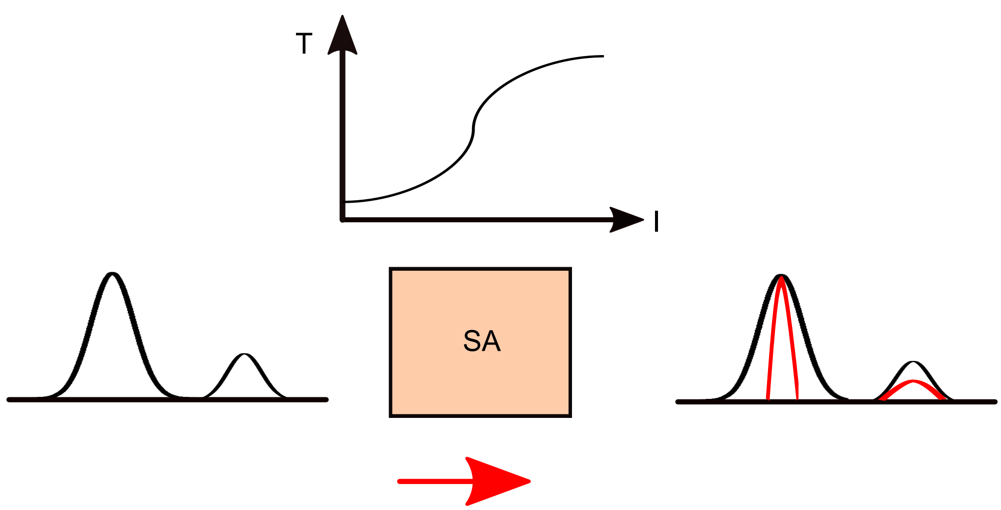

Figure 1.9: Working principle of a saturable absorber where T: transmittance of the saturable absorber and I: incident intensity.

to the intensity of the light. The higher the intensity, the more is the rotation of the polarization ellipse. Since the polarizer at the end transmits only the vertical component of the polarization, the transmission depends on the intensity of the signal which essentially performs the function of a SA and favors the formation of a pulse from noise. A combination of half waveplate (HWP) and a QWP acts as an analyzer which adjusts the polarization to match the axis of the second polarizer.

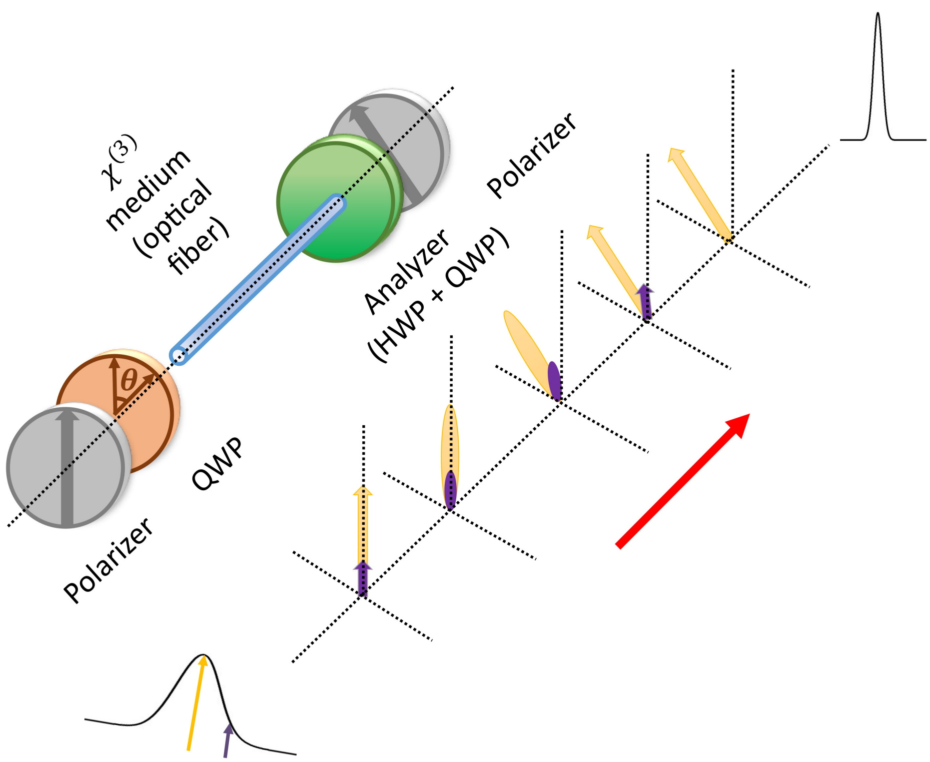

Figure 1.10: Nonlinear polarization based saturable absorber.

1.11 Spectral filter

As explained earlier, spectral filter is another type of amplitude modulation which is very critical to ensure self-consistent solution in dissipative soliton as well as similariton type of mode-locking. The spectral filters used in the experimental work pertaining to this dissertation are - birefringence based filter, interference filter and grating- collimator (dispersive element - waveguide) filter.

1.11.1 Birefringence based filter

The birefringence based filter used in this thesis is called Lyot filter, named after its inventor Bernard Lyot [23]. It is composed of two polarizers with a birefringent plate at an angle of 45° sandwiched in between as shown in Figure 1.11(a). The first polarizer imposes linear polarization on the input light, and it can be decomposed into orthogonal states as it couples to the fast and slow axes of the birefringent medium. As the light propagates through the birefringent medium, it accumulates relative phase shift depending on the birefringence and this phase shift is wavelength dependent and induces rotation of the polarization state.

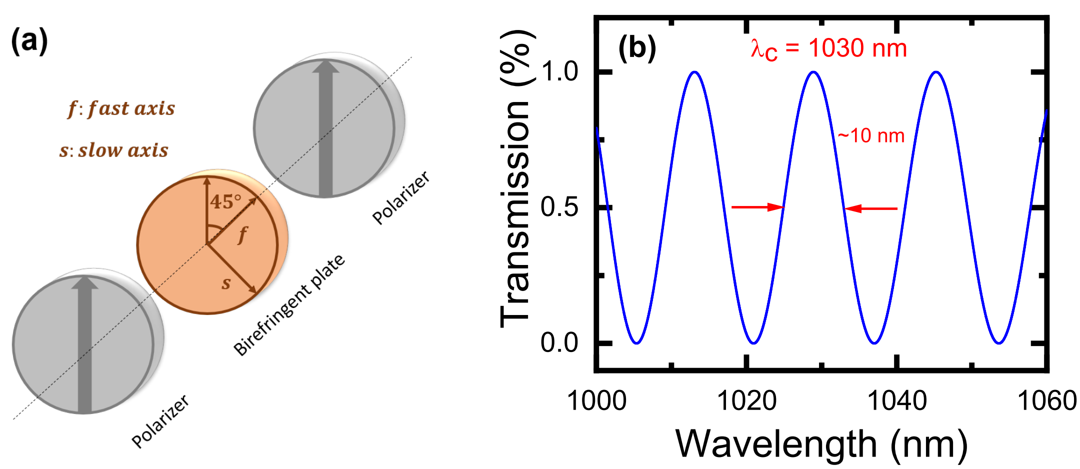

Figure 1.11: (a) Birefringent plate based spectral filter (b) Calculated filter transmission profile for the birefringent plate filter with the plate thickness d = 7.5 mm.

The second polarizer converts this wavelength-dependent rotation into amplitude modulation, which gives rise to a sinusoidal transmission curve given by

$$T = cos^2\left(\frac{\Delta\phi}{2}\right) \tag{1.13}$$

where, $\Delta\phi$ is relative phase shift

$$\Delta\phi = \frac{2\pi}{\lambda}\left(n_e - n_o\right)d \tag{1.14}$$

where, n_o and n_e are the ordinary and extra-ordinary refractive indices for the birefringent medium. The Equations (1.13) and (1.14) show that the FWHM bandwidth of this filter depends on the birefringence of the plate as well as the thickness of it. To achieve $\sim$ 10 nm FWHM bandwidth spectral filter at 1030 nm, a quartz plate (n_o = 1.53514 and n_e = 1.54392), approximately 7.5 mm thick plate is required and its transmission curve is shown in Figure 1.11(b).

The same filter can be manufactured entirely in the fiber format where birefringent plate is replaced by a birefringent fiber such as polarization maintaining (PM) fiber and bulk polarizers can be replaced by in-line fiber polarizers. The transmission axis of the in-line polarizer is adjusted and spliced at a 45 $^\circ$ angle with respect to the slow axis of the PM fiber. The schematic of such filter is shown in Figure 1.12(a). To achieve $\sim$ 10 nm FWHM bandwidth at 1030 nm, a PM fiber (n_e - n_o= 3.629 $\times$ 10^{-4}), approximately $\sim$ 15 cm of the PM fiber is required and this simulated transmission profile is shown in Figure 1.12(b).

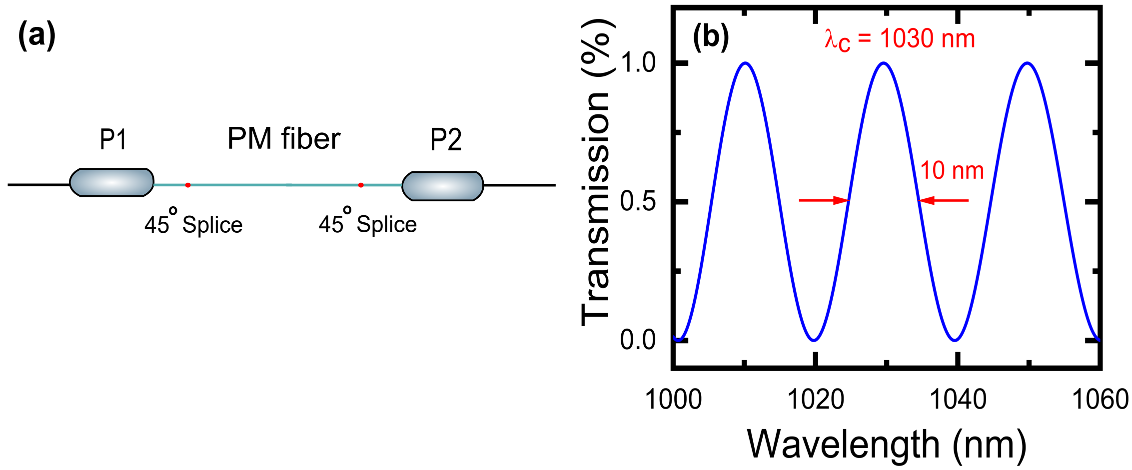

Figure 1.12: An all-fiber Lyot Filter (a) schematic of the filter (b) Calculated transmission profile with the PM fiber length = 14.75 cm. P: in-line polarizer.

1.11.2 Interference filter

Interference filters use the phenomenon of interference in order to transmit or reflect particular ranges of wavelengths of electromagnetic radiation. This is achieved by depositing a large number of thin coatings with different refractive indices on a piece of glass. Although there are various kind of interference filters such as high-pass, low-pass, and band-pass filters (BPF), in this dissertation, a BPF is used. A BPF is a narrowband interference filter which can be treated as a Fabry-Perot interferometer. A Fabry-Perot is a simple interferometer which relies on the interference of multiple reflected beams as shown in Figure 1.13. Incident light suffers multiple reflections between thin-film coated surfaces which define the cavity. When there is no phase difference between transmitted wavefronts, the output produces a transmission maximum and this happens when the optical path difference is an integral multiple of the wavelength and this relationship is given by

$$m\lambda = 2tcos\theta \tag{1.15}$$

where m is an integer, λ is the wavelength of the incident light, t is the optical thickness and θ is the angle of incidence. Upon failing to satisfy this equation leads to a destructive interference and zero transmission. The wavelength of peak transmittance in terms of angle of incidence is given by

$$\lambda_c = \lambda_{max}\sqrt{1-\left(\frac{n_o}{n_e}\right)^2 sin^2\theta} \tag{1.16}$$

where, λ_c is the center wavelength of the filter transmission curve, λ_0 is the filter center wavelength at the normal incidence, and n is the refractive index of the dielectric material between the mirrors. The λ_c is always shorter than λ_0. It is very difficult to get a very narrow bandpass filter of a specific shape and they are also lossy. The measured transmission curve of such interference filter is shown in Figure 1.14.

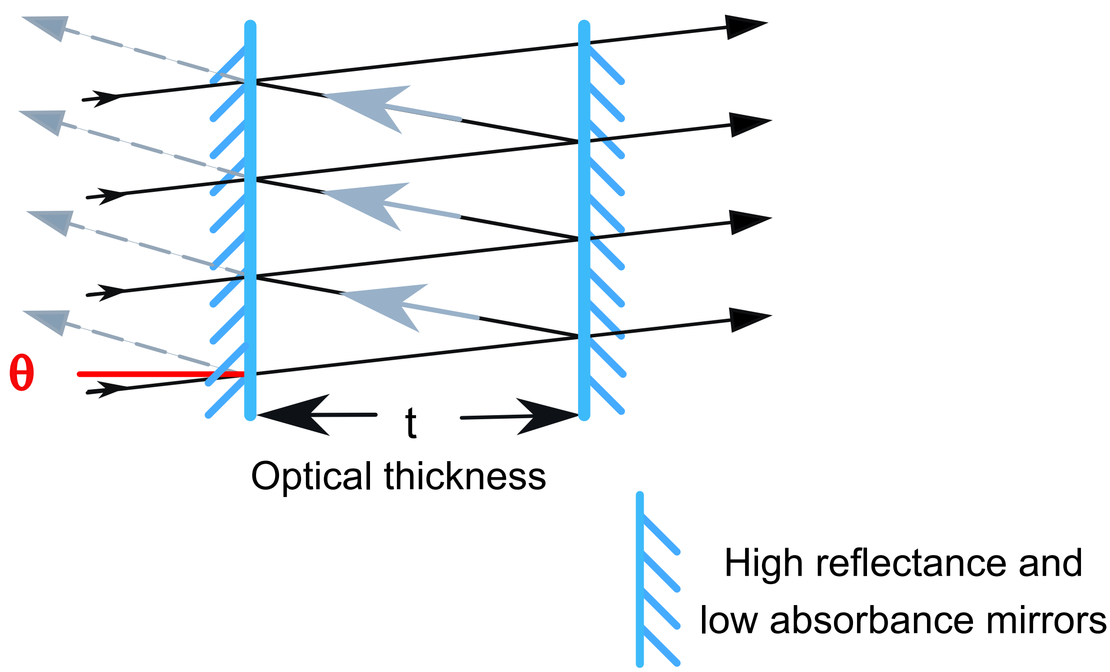

Figure 1.13: Schematic of a Fabry-Perot bandpass filter. The incident angle is denoted by θ.

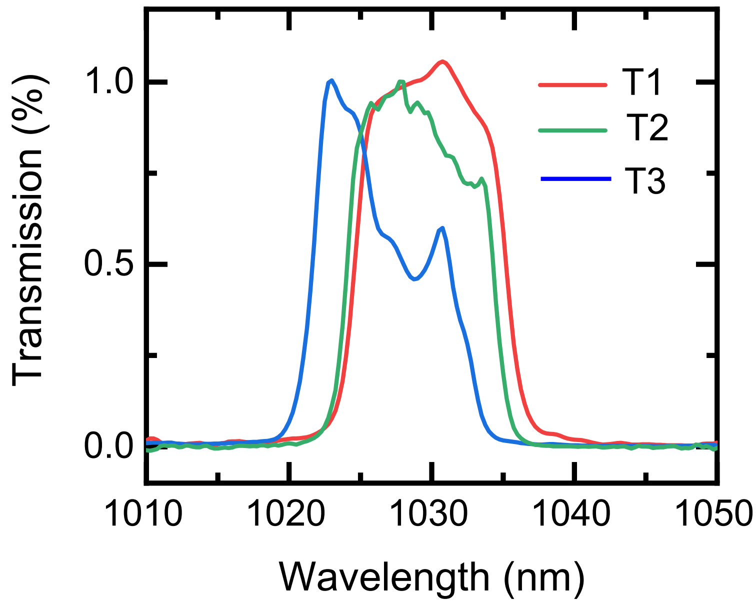

Figure 1.14: Recorded transmission of an interference filter at the central wavelength of 1030 nm (T1), 1028 nm (T2) and 1026 nm (T3) by tuning the angle of the filter with respect to the incident beam. As the center wavelength deviates from 1030 nm, the transmission curve exhibits complex structures.

1.11.3 Dispersive element - waveguide filter

Mode-locked fiber lasers like self-similar fiber lasers require narrow bandwidth filters ($\sim$ 4 nm). In this case, birefringent filters are not good choices because of they have a multipeak transmission curve. Also, numerical simulations show better performance are generated from the laser cavities with Gaussian filters [16, 19]. Gaussian shape filter can be created by the combination of a dispersive element and a collimator (fiber and a lens) as shown in Figure 1.15. The overlap of the wavelength dependant spatial beam with the mode of the single mode fiber results into Gaussian shape spectral filter. The bandwidth of this filter can be designed by careful calculation using ABCD matrices [24]. It is a function of grating constant, input beam diameter, fiber mode field diameter and focal length of

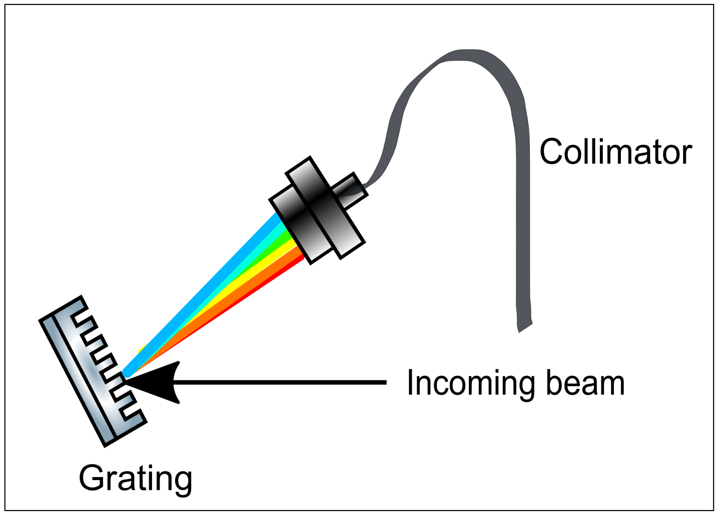

Figure 1.15: Schematic of a grating-collimator filter.

the collimator lens. A 300 lines/mm grating with 1 mm input beam diameter and 6 μm fiber mode field diameter and with 4.5 mm collimator lens focal length results in 4 nm FWHM bandwidth Gaussian spectral filter at 1030 nm.

1.12 Optical fibers

The experimental work in this thesis utilizes different types of fibers - single mode, single clad fibers, double clad (DC) fibers, large mode area (LMA) fibers and polarization maintaining (PM) fibers. This section will briefly touch upon all these types of fiber.

1.12.1 Single mode and multimode fibers

A fiber is called a single mode if it has V number $= \frac{2.\pi.a.NA}{\lambda_0} < 2.405$ with a being core radius and NA being numerical aperture. Hence, when the fiber core radius is small, only one spatial mode can exist and it is invariant upon propagation. When the core size becomes larger, it can support more than one mode and the fibers are called multimode fibers (MMF). All these modes travel at different velocities along the fiber and hence pulse spreads faster in MMFs. Although MMFs have a larger core which means they can carry more power, if such fibers are used to construct a laser or an amplifier, its output will be a speckle pattern instead of a nice beam quality obtained from SMF based fiber lasers and amplifiers. As explained in previous sections, enormous progress has been made toward controlling the interactions of longitudinal modes in lasers with a single transverse mode. In terms of locking multiple longitudinal as well as transverse modes of an MMF to create ultrafast pulse presents its own challenge. But in 2017, the first MMF spatiotemporal mode-locking was achieved in a complete MMF cavity which shows a promising route to high power ultrafast MMF lasers [25].

1.12.2 Double clad fibers

A fiber laser or amplifier based on SMFs can generate a diffraction-limited output, but it restricts the pump sources to the SMF coupled pump diodes and thus normally to those with low powers. On the other hand, the use of MMFs usually leads to poor beam quality. This problem has been resolved with the invention of DC fibers [26], a class of optical fiber with a structure consisting of three layers of optical material instead of the usual two as shown in Figure 1.16. The inner-most layer is called the core. It is surrounded by the inner cladding, which is surrounded by the outer cladding. The inner cladding has a significantly larger area and typically a much higher numerical aperture, so that it can support a large number of propagation modes, allowing the efficient launch of the output, e.g. of high-power laser diodes despite their poor beam quality. The pump light is restricted to the inner cladding by an outer cladding with a lower refractive index, and the pump light also partly propagates in the single-mode core, where it can be absorbed by the rear earth dopant

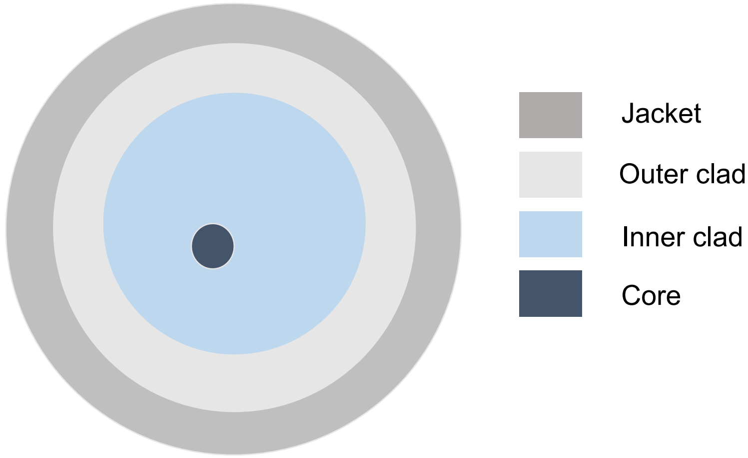

Figure 1.16: Cross-section of a DC fiber with offset core.

ions as shown in the Figure 1.17. There are a variety of different designs of double-clad fibers so that propagation modes of the inner cladding have good overlap with the core so that the pump light can be efficiently absorbed. This thesis deals with DC fibers with off-centered core and double D-shaped core designs.

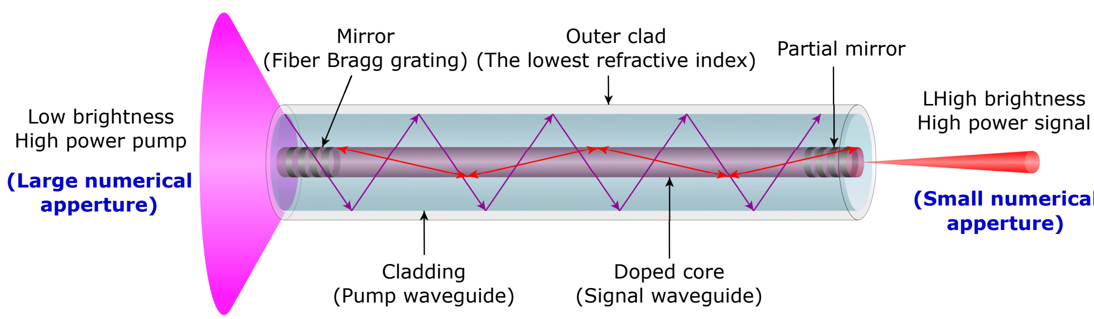

Figure 1.17: Schematic diagram of a cladding pumped double-clad fiber laser [27].

1.12.3 Large mode area fibers

Standard SMFs [Figure 1.18(a)] have a mode area below 100 μm^2 whereas LMA fibers have a mode area values of hundreds or thousands of μm^2 as shown in Figure 1.18(b). Due to the very small core area in standard SMFs, the power density is high enough to induce nonlinear effects and/or fiber damage. In order to reduce power density, the mode area of LMAs is designed to be larger, while maintaining single-mode performance, by reducing the NA and increasing the core diameter. This means that higher powers can be handled before nonlinear effects occur. This makes them suitable for certain applications like the amplification of intense pulses in fiber amplifiers, or as passive fibers for delivery of intense light.

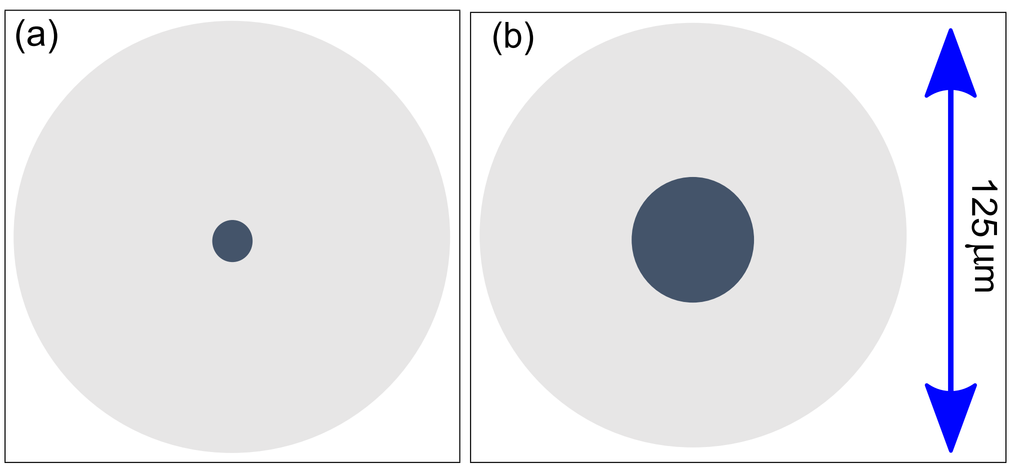

Figure 1.18: Comparison between uncoated a) standard SMF and b) LMA fiber. The dark blue circle represents core.

1.12.4 Polarization maintaining fibers

The standard SMFs always have some degree of birefringence, even if they exhibit a perfect circular symmetry, because there is always some amount of mechanical stress acting on the fiber. As a result, the polarization of light propagating in the fiber gradually changes, which is an undesired effect in some applications. This problem can be solved by using a PM fiber, a specialty fiber with a strong built-in birefringence so that there are two well-defined polarization modes which propagate along the fiber with very distinct phase velocities. Hence, if the polarization of light launched into the fiber is aligned with one of the birefringent axes, this polarization state will be preserved even if the fiber is bent. A commonly used method for introducing strong birefringence is to include two stress rods of a modified glass composition in the preform on opposite sides of the core as shown in Figure 1.19(a). This thesis uses a PANDA fiber structure, although the same experiments can be done with a bow-tie geometry [Figure 1.19(b)].

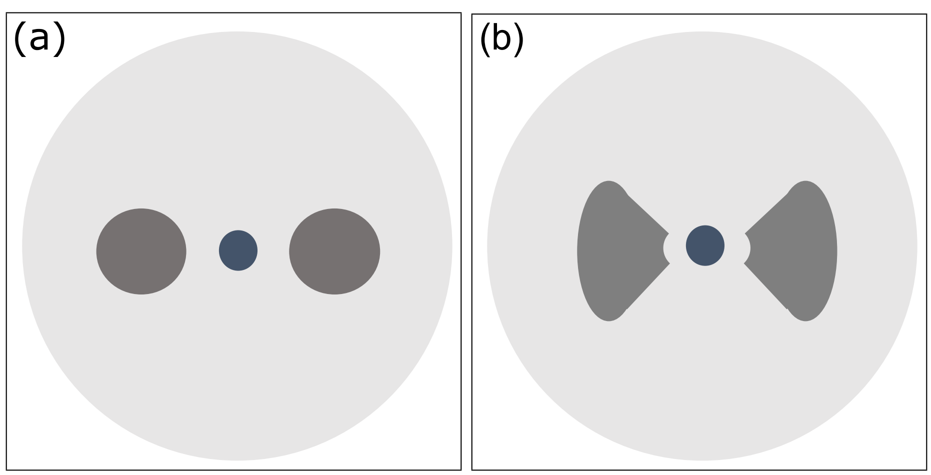

Figure 1.19: Types of PM fibers a) PANDA fiber b) bow-tie fiber. The dark blue circle represents the core while dark gray features are the stress elements.

1.12.5 Photonic crystal fibers

Philip Russell [28] coined the term PCF and his idea dates to unpublished work in 1991. Standard optical fibers guide light by total internal reflection (TIR) between core with high refractive index (Ge doped silica) and comparative low refractive index cladding (F doped silica). The index difference in PCFs is obtained by air voids running along the length of the fiber. PCFs can be divided into two categories, high index guiding fibers and low index guiding fibers. In the high index guiding fibers shown in Figure 1.20 (a), the light is guided in a solid core by the TIR caused by the lower effective index of air filled microstructured cladding. The refractive index of the microstructured cladding in PCFs exhibits a wavelength dependency distinctively different property than that from pure silica. As a result, this type of PCFs have very unique properties. For example, the design of endlessly single-mode fibers is possible, where only a single mode is supported regardless of the optical wavelength. Furthermore, it is possible to alter the dispersion properties of the fibers. By designing the fibers with a combination of a small core and phase matching dispersion properties close to available pump sources, the PCF technology makes it possible

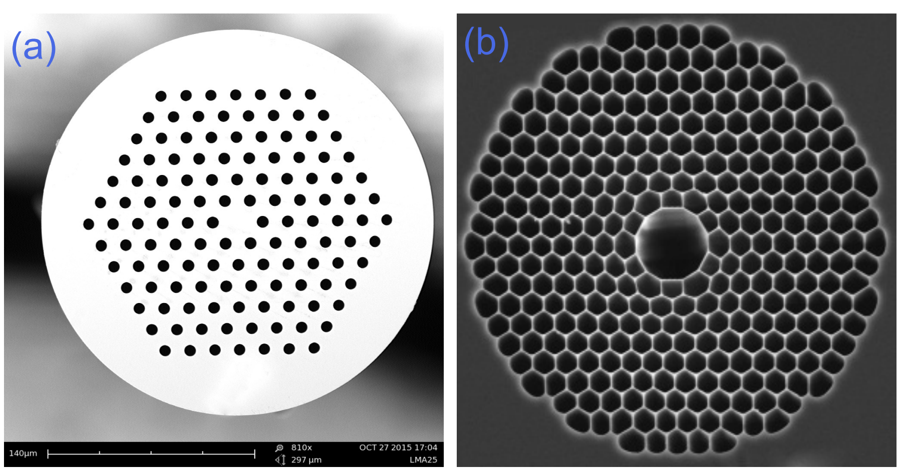

Figure 1.20: Types of PCFs a) high index PCF [29] b) low index PCF [30].

to create very efficient supercontinuum generation. Also, fibers with extremely large mode field diameters (LMA-PCFs) are possible, supporting high beam quality fiber guidance and amplification or lasing. It is also possible to achieve strong birefringence with an asymmetric arrangement of holes in the cladding. In low index guiding fibers shown in Figure 1.20 (b), the light is guided by photonic bandgap (PBG) effect. The periodic structures in the fiber cladding have a bandgap that prohibits passing certain frequency of light. Now, the refractive index of the core can be lesser than the cladding. The core can be hollow (air). These PCFs can be used to guide light that has high absorption in the glass e.g. CO_2 laser light. It can also be used for the delivery of high power laser beams. Because of the weak nonlinearity, they are also good candidates for nonlinear pulse compression.

1.12.6 Fluoride fibers

These optical fibers are based on fluoride glasses, e.g. fluoroaluminate or fluorozirconate glasses. The fibers drawn from fluorozirconate glasses are called ZBLAN (ZrF_4-BaF_2-LaF_3-AlF_3-NaF) fibers. These fibers exhibit high transparency in mid- infrared (IR) region where standard silica fibers are very lossy. These fibers can be doped with a number of rare earth ions and can be used as gain media for fiber lasers and amplifiers [31]. Some fluoride fibers are used for supercontinuum generation in the mid-infrared region [32, 33]. Problems with fluoride fibers are that they are often expensive and difficult to handle due to their fragility. They have limited chemical stability and are hygroscopic. In this dissertation, a Pr doped ZBLAN fiber is used for building a fiber laser in the visible region.

CHAPTER II

AN ALL-FIBER BANDWIDTH TUNABLE SPECTRAL FILTER

In this chapter, two ways to build an all-fiber, bandwidth (BW) tunable spectral filter are presented. Both the designs are based on birefringent fibers and the successful design is implemented in all-normal dispersion (ANDi) fiber laser to generate distinct laser modes with different output spectral shapes and pulse evolutions.

2.1 Introduction

The behavior of mode-locked ANDi fiber lasers is determined by three main parameters, namely, nonlinear phase shift, group velocity dispersion (GVD), and BW of the spectral filter [34]. Even though spectral filter BW can alter the laser output significantly, tuning the filter BW is inconvenient. For example, in ANDi lasers with bulk birefringent filters, the spectral filter BW can be tuned by inserting a birefringent plate of a different thickness in the laser cavity which requires realignment of the laser cavity [35]. Fiber based spectral filtering solutions, on the other hand, lead to misalignment free fiber oscillator designs [36, 37, 38, 39, 40, 41]. All these all-fiber oscillators can generate nanojoule (nJ) pulses with the pulse duration ranging from picosecond (ps) to femtosecond (fs). Despite the fact that the idea of a fiber based spectral filter is well explored, these filters do not have tunable BW. It is believed that a fiber based spectral filter with a tunable BW will provide a user-friendly fiber laser design to adjust the laser output conveniently.

As already explained in Chapter I, a promising approach towards a tunable BW spectral filter is a birefringent fiber based spectral filter [41], a fiber analogy to a Lyot filter [23]. This filter provides sinusoidal transmission and the full width half maximum (FWHM) BW of the transmission can be expressed as

$$\Delta\lambda \cong \frac{\lambda^2}{2L\Delta n} \tag{2.1}$$

where $\Delta\lambda$ is FWHM BW, λ is the wavelength, L is the length of polarization maintaining (PM) fiber and $\Delta n = n_{fast}$ - n_{slow} is the fiber birefringence with n_{fast} and n_{slow} are the effective refractive indices of the fast and slow axes of the PM fiber. Although this filter is very simple to implement, in order to change the filter BW, the filter needs to be reconstructed since the length of the PM fiber has to be adjusted. Fedotov *et al.* proposed that introducing a segment of PM fiber into a standard single mode fiber (SMF) based laser cavity leads to the creation of the Lyot filter with variable modulation depth instead of adjustable BW. The variation in the output pulse duration and spectral width was possible only when a new length of the PM fiber was spliced in the fiber cavity. Moreover, the laser had a relatively low average output power and low pulse energy which is insufficient for practical applications [42, 43]. Similarly, Wang *et al.* demonstrated a similariton-dissipative soliton laser claiming that the mode-locking transition was due to an adjustable BW filter but in actuality the modulation depth of the spectral filter was adjusted [44]. Therefore, designing a true BW tunable filter is an interesting problem to handle. The two designs are discussed in the following sections. The first design is based on twisted PM fiber and the filter is completely made up of PM fibers while the other is modification to the fiber based Lyot filter.

2.2 Twisted PM fiber based spectral filter

The schematic of the fiber based spectral filter is shown in Figure 2.1. It consists of a PM fiber spliced between two in-line polarizers at an angle of 45°. The part of the PM fiber section is twisted using bare fiber rotator. The first polarizer imposes linear polarization

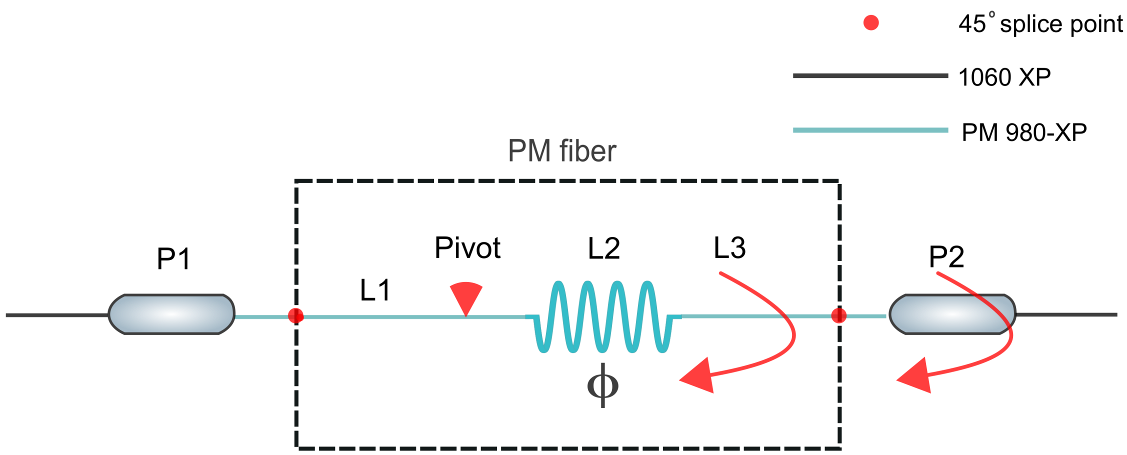

Figure 2.1: Schematic of twisted fiber based spectral filter. P: polarizer, PM: polarization maintaining fiber, L1: unrotated, non-twisted PM fiber, L2: twisted PM fiber with ϕ as a twist angle, L3: rotated PM fiber. The arrows indicate parts under rotation.

on the input light which then propagates along the PM fiber. As discussed in Chapter I, PM fiber preserves the state of polarization of input light due to strong built-in linear birefringence. But as the PM fiber is subjected to twist, shear strain in the twisted fiber gives rise to circular birefringence. The combination of this circular birefringence along with the linear birefringence rotates the state of polarization [45]. The second polarizer converts this wavelength dependent rotation into amplitude modulation which gives rise to a sinusoidal transmission curve. Hence, the total birefringence and therefore the filter BW can be tuned significantly by adjusting the twist applied to the PM fiber. It should be noted that only a part of the PM fiber is twisted. So, a single PM fiber can be considered as a combination of three sections say, L1, L2 and L3 as shown in Figure 2.1. L1 is the section of the PM fiber which remains untwisted. At the section of L1, the PM fiber is clamped and a fiber rotator starts rotating the remaining fiber. Only the section L2 experiences a twist (defined by the twist angle ϕ) while the section L3 undergoes only rotation. As the entire filter is fiberized, the second polarizer also rotates. The rotation angles for L3 and the second polarizer roughly takes up the value of the twist angle. The transmission spectrum of such filter can be simulated using Jones calculus and is given by

$$T = P(\psi) \cdot M_{L3} \cdot R(-\phi) \cdot M_{L2} \cdot R(\phi) \cdot M_{L1} \cdot P(\theta) \tag{2.2}$$

where, P(θ) is the Jones matrix for the polarizer with the axis of transmission making an angle θ with the PM fibers and depicted by Equation 2.3. In this case, θ is 45°. As explained earlier, the total rotation angle ψ is the addition of θ i.e. 45 ° to the twist angle and therefore, it can be defined as ψ = 45°+ ϕ.

$$P(\theta) = \begin{pmatrix} \cos^2\theta & \frac{1}{2}\sin 2\theta \\ \frac{1}{2}\sin 2\theta & \sin^2\theta \end{pmatrix} \tag{2.3}$$

ML_1 and ML_3 can be expressed as

$$\begin{pmatrix} e^{-i\frac{\Gamma}{2}} & 0 \\ 0 & e^{i\frac{\Gamma}{2}} \end{pmatrix} \tag{2.4}$$

where, $\Gamma = \frac{2\pi}{\lambda}\Delta n L$ is the phase shift acquired in the PM fibers. The state of polarization of light propagating through the twisted PM fiber (L2) can be described by a Jones matrix M_{L2} and is given by [46]

$$M_{L2} = R(\phi) \begin{pmatrix} \cos X - i\frac{\Gamma_2}{2}\frac{\sin X}{X} & -\phi\frac{\sin X}{X} \\ \phi\frac{\sin X}{X} & \cos X + i\frac{\Gamma_2}{2}\frac{\sin X}{X} \end{pmatrix} \tag{2.5}$$

where, X = $\sqrt{\phi^2 + (\frac{\Gamma_2}{2})^2}$ and $\Gamma_2 = \frac{2\pi}{\lambda}\Delta n L2$ and the rotator matrix is given by

$$R(\phi) = \begin{pmatrix} \cos\phi & \sin\phi \\ -\sin\phi & \cos\phi \end{pmatrix} \tag{2.6}$$

A few sample simulated transmission spectra of the proposed spectral filter are shown in Figure 2.2(a). The lengths of the PM fiber sections in this filter are 8.5 cm (L1), 7.7 mm (L2), and 29.4 cm (L3). After promising simulation results, the filter is constructed but the

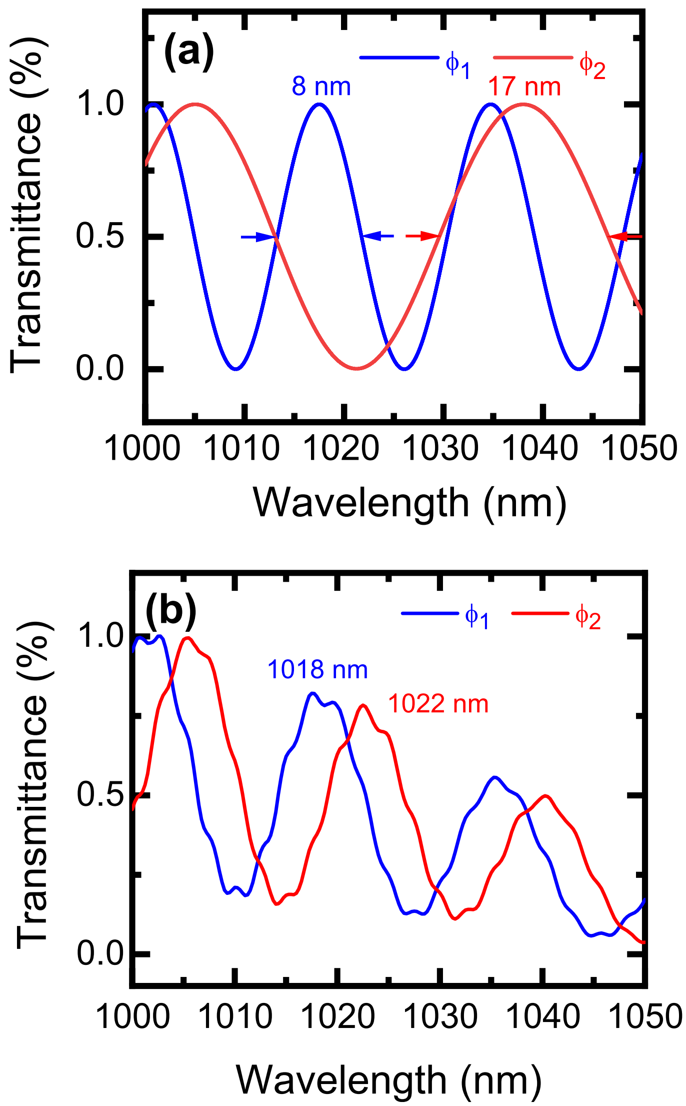

Figure 2.2: Twisted fiber filter results (a) calculated transmission spectra of the filter for different twist angles, $\phi = 0\ ^{\circ}$ (blue curve) and $\phi = 45\ ^{\circ}$ (red curve), respectively (b) measured experimental transmittance with different twist angles.

twisting mechanism using a fiber rotator is not able to produce a reasonable twist, which in turn affects the filter BW tunability. Figure 2.2(b) depicts that the central wavelength of the filter transmission is tunable but BW almost stays the same. During the primary experimentation, it is realized that rotating entire polarizer along with L3, will not be feasible in a fiber laser cavity. Hence, the alternate design for the filter is considered.

2.3 PM-SMF-PM spectral filter

The schematic of this fiber based spectral filter is shown in Figure 3.1. It consists of a single mode fiber (SMF) spliced between two PM fibers that are spliced to in-line polarizers at an angle of 45°. The polarization controller (PC1) can be tuned to create a stress induced birefringence in the SMF. The first polarizer imposes linear polarization on the input light which then propagates along PM1, SMF, and PM2 accumulating relative phase shift in each fiber depending on their birefringence. This phase shift is wavelength dependent and induces rotation of the polarization state. The second polarizer converts this wavelength dependent rotation into amplitude modulation which gives rise to a sinusoidal transmission curve. Hence, the total birefringence and therefore the filter BW can be tuned significantly by adjusting the stress birefringence in the SMF. For example, one can control the stress induced birefringence of SMF such that it produces polarization rotation of mπ (where m is an integer) and the birefringence of PM1 is added to the birefringence of PM2 to end up with a narrower filter BW. On the other hand, the stress induced birefringence in the SMF can be adjusted to rotate the polarization by (2m+1)$\pi/2$, so that the birefringence of PM1 is compensated by that of PM2 [47]. When the length of PM2 is longer than that of PM1, the uncompensated birefringence of PM2 generates a spectral filter with wide BW. When

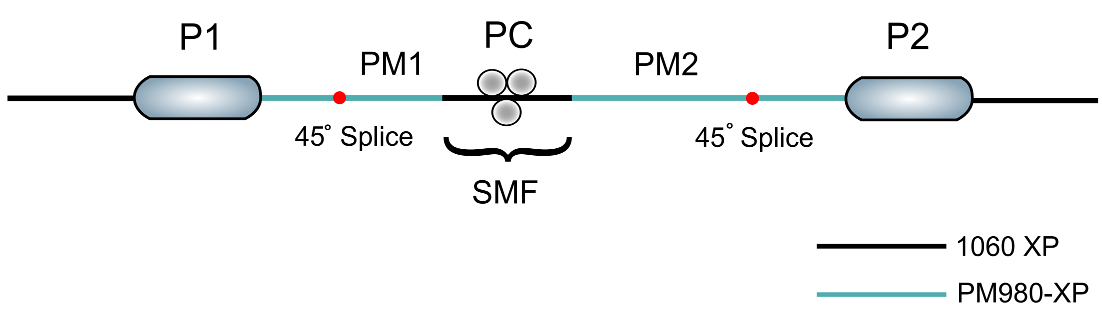

Figure 2.3: Schematic of fiber based spectral filter. P: polarizer, PC: polarization controller, PM: polarization maintaining fiber, SMF: single mode fiber.

the stress induced birefringence in the SMF produces a polarization rotation which is neither mπ nor (2m+1)π/2, it can lead to a variety of transmission profiles. Although one may find such filter transmission interesting, it is not suitable for mode-locking a fiber laser as it severely deviates from Gaussian profile which is widely used as a spectral filter in ANDi lasers. By taking all experimental considerations into account, the lengths of SMF, PM1 and PM2 are approximately 14.5 cm, 10 cm, and 20 cm, respectively. Again, the transmission spectrum of the filter can be simulated using Jones calculus and it is given by

$$T = P(\theta_2) \cdot M_{PM2} \cdot R(-\phi) \cdot M_{SMF} \cdot R(\phi) \cdot M_{PM1} \cdot P(\theta_1) \tag{2.7}$$

Based on Equation 2.7, the simulated transmission spectra of the proposed spectral filter are shown in Figure 2.4. The filter BW changes from 4.5 nm to 10.8 nm, owing to the fact

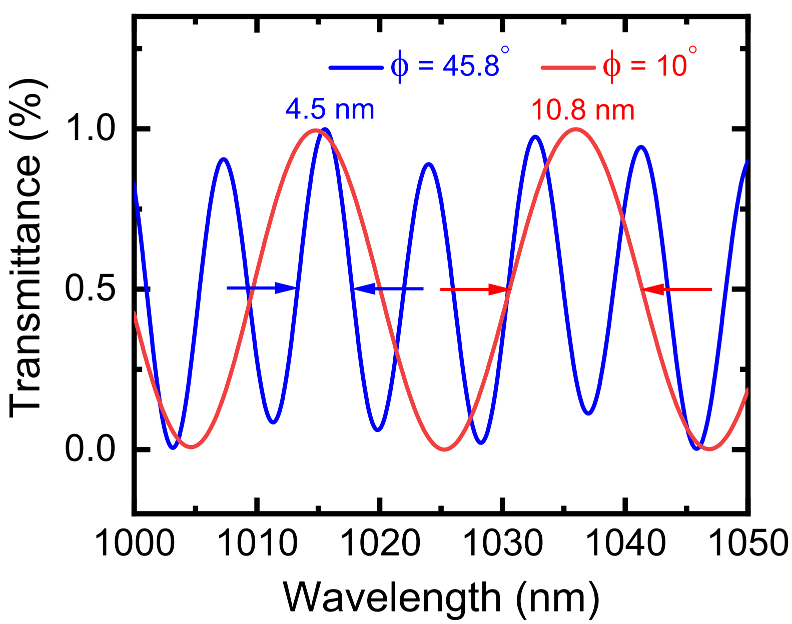

Figure 2.4: Calculated transmission spectra of the filter for different angles of rotation of polarization inside the SMF, namely, $\phi = 45.8°$ (red curve) and $\phi = 10°$ (blue curve). The values for the birefringence assumed are $\Delta n_1 = \Delta n_3 = 3.6 \times 10^{-4}$ and $\Delta n_2 = 3.8 \times 10^{-6}$ for the PM fibers and the SMF, respectively.

that PM2 is approximately twice as long as PM1. The filter can generate three distinct BWs if another SMF-PM section is added to the existing filter design. The transmission spectra of such a spectral filter are depicted in Figure 2.5. The lengths of the PM fibers in this filter are 10 cm, 23 cm, and 5 cm, respectively. The length of the SMF sections is 14.5 cm each. The narrowest BW is due to the birefringence addition of all the three PM fibers, whereas the intermediate BW is due to birefringence compensation of PM1 by PM2, and the widest BW is due to the compensation of PM1 and PM3 by PM2. Furthermore, one can generate a number of discrete bandwidths by introducing additional SMF-PM sections in the existing filter design.

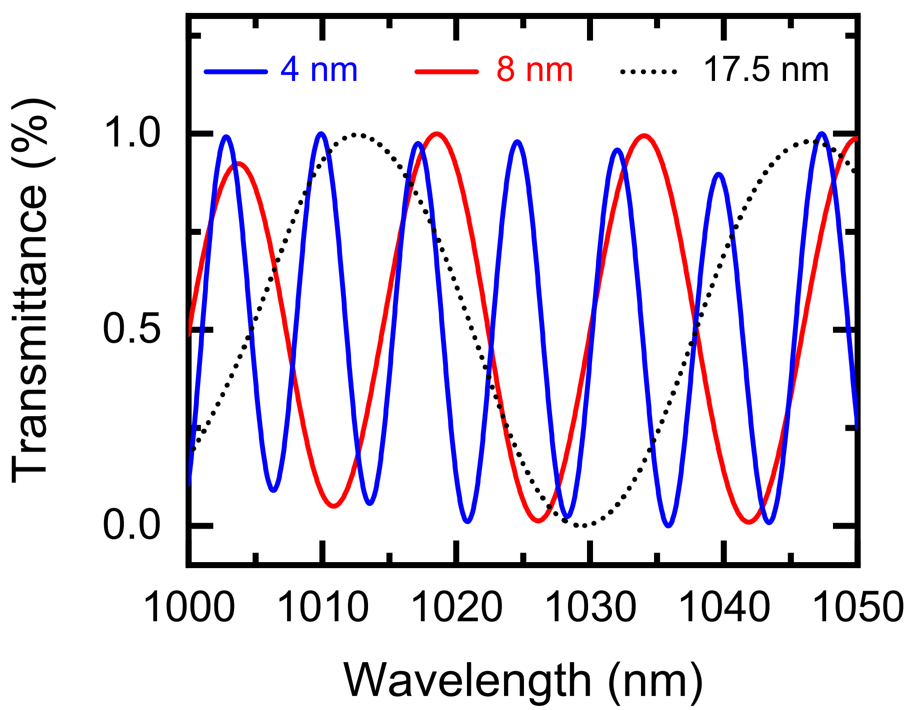

Figure 2.5: Calculated transmission spectra of the PM1-SMF1-PM2-SMF2-PM3 filter with FWHM BW of 4 nm (blue curve), 8 nm (red curve) and 17.5 nm (dotted black curve), respectively.

2.4 Experimental results

After promising simulation results, the PM1-SMF-PM2 filter (Figure 2.4) is constructed and introduced in a Yb laser cavity. The experimental configuration of the oscillator is schematically illustrated in Figure 2.6. A wavelength division multiplexer (WDM) couples a 976 nm pump into a 55 cm of Yb gain fiber followed by $\sim$ 1 m of SMF. A polarization controller (PC2), a half waveplate (HWP), a quarter waveplate (QWP), and a polarizing beam splitter (PBS) serve as a nonlinear polarization evolution (NPE) based saturable absorber to initiate the mode-locking process. An isolator ensures unidirectional operation. A HWP after the isolator adjusts the polarization to maximize the transmission through the first in-line polarizer. A 80/20 fused coupler is used to monitor the spectrum after the spectral filter. The total length of the fibers in the cavity is 5.24 m and the total cavity dispersion is 0.12 ps^2.

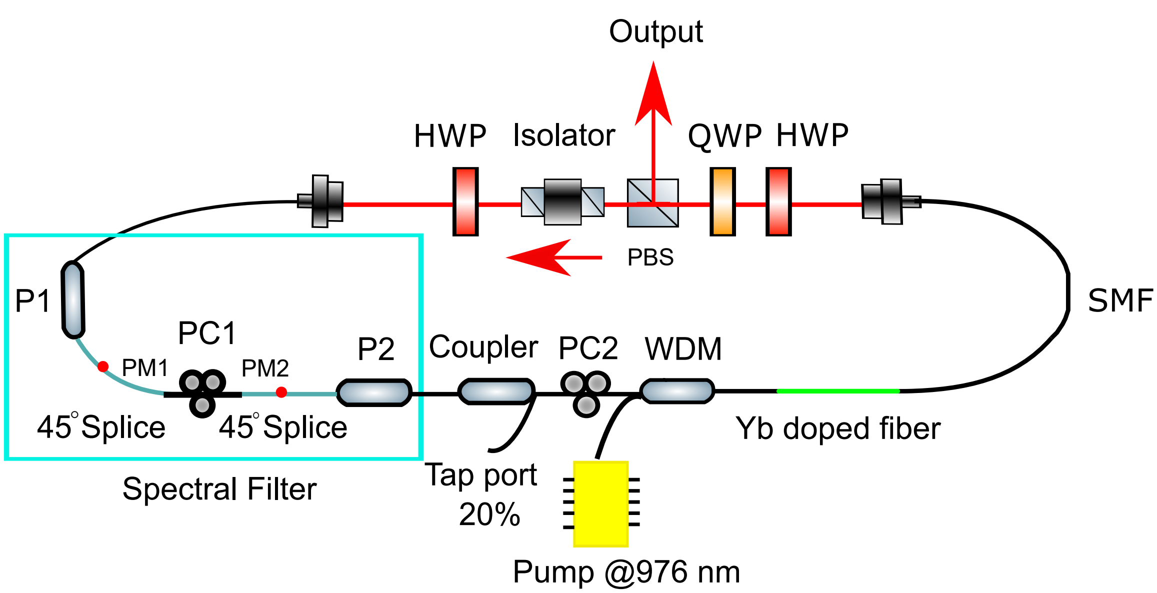

Figure 2.6: The experimental set-up of the fiber laser. PC: polarization controller, HWP:Half waveplate, QWP: Quarter Waveplate, PBS: Polarizing beam splitter.

The transmission characteristics of the proposed spectral filter are experimentally verified by operating the cavity below the lasing threshold at a very low pump power (∼50 mW). A broadband amplified spontaneous emission (ASE) [shown in Figure 2.7(a)] is coupled into the spectral filter and the filter output can be observed through the 20% port of the coupler. The PC1 is carefully tuned so that the output of the spectral filter mimics the BW of the simulated transmission spectra [shown in Figure 2.7(b)]. Figures 2.7(c) and 2.7(d) show the comparison between experimental and simulated transmission spectra of

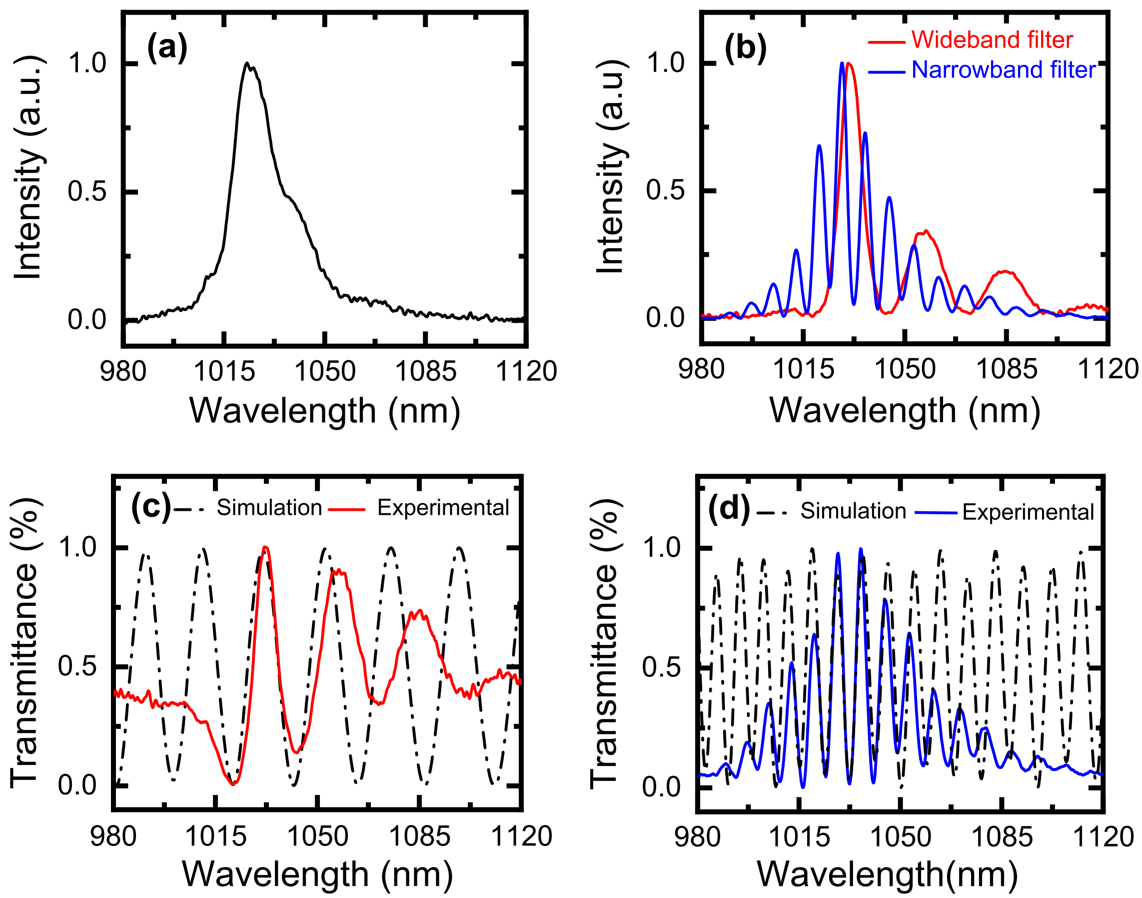

Figure 2.7: The experimental (a) ASE (b) transmission spectra of wideband (red curve) and narrowband (blue curve) filter at different settings of PC1 (c) theoretical (dashed line) and experimental (solid line) transmittance of wideband filter (d) theoretical (dashed line) and experimental (solid line) transmittance of narrowband filter.

the filter. The full width half maximum (FWHM) BWs match very well in the region of 1030 nm. The mismatch between these spectra at longer wavelengths can be due to the change in beat length at these wavelengths.

Initially, the PC1 is adjusted to obtain the 10.8 nm BW spectral filter by operating the cavity below the lasing threshold to observe the filter transmission of ASE through the 20 % port of the coupler. Then, the pump power is increased and a self-starting mode-locking is achieved by rotating intracavity waveplates and tuning PC2 (PC1 is left untouched) at a pump power of 350 mW. A typical output spectrum ejected by the PBS is shown in Figure 2.8(a). The spectrum has FWHM BW of 14.3 nm at the center wavelength of 1032 nm and it exhibits the typical steep edges as a characteristic of the ANDi laser spectrum. The optical spectrum taken at the 20% port of the fiber coupler is also shown in Figure 2.8(b) which shows FWHM BW of 8.5 nm. The laser produces a stable pulse train with 35 MHz repetition rate. The average mode-locked output power is 60 mW, which corresponds to a pulse energy of 1.7 nJ. Figure 2.8(c) depicts the radio frequency (RF) spectrum measured with a photodiode with a rise time of 50 ps and a high resolution RF spectrum analyzer (Agilent N9914A). There is no indication of residual sidebands at least 80 dB below the carrier. Additionally, stable single pulsing is verified with a photodiode (rise time of 1 ns) and by monitoring the interferometric autocorrelation (AC) to the delay of 100 ps. The laser generates chirped pulses, which are de-chirped to 230 fs duration with a grating pair outside the cavity (Figure 2.8(d)).

To achieve a 4.5 nm BW spectral filter, the pump power is set below the lasing threshold and the PC1 is tuned. The pump power is then increased and a self-starting mode-locking is achieved by tuning waveplates and the PC2 at the pump power of 220 mW. The spectrum (Figure 2.9(a)) has a FWHM BW of 6.6 nm at the center wavelength of 1028 nm. The

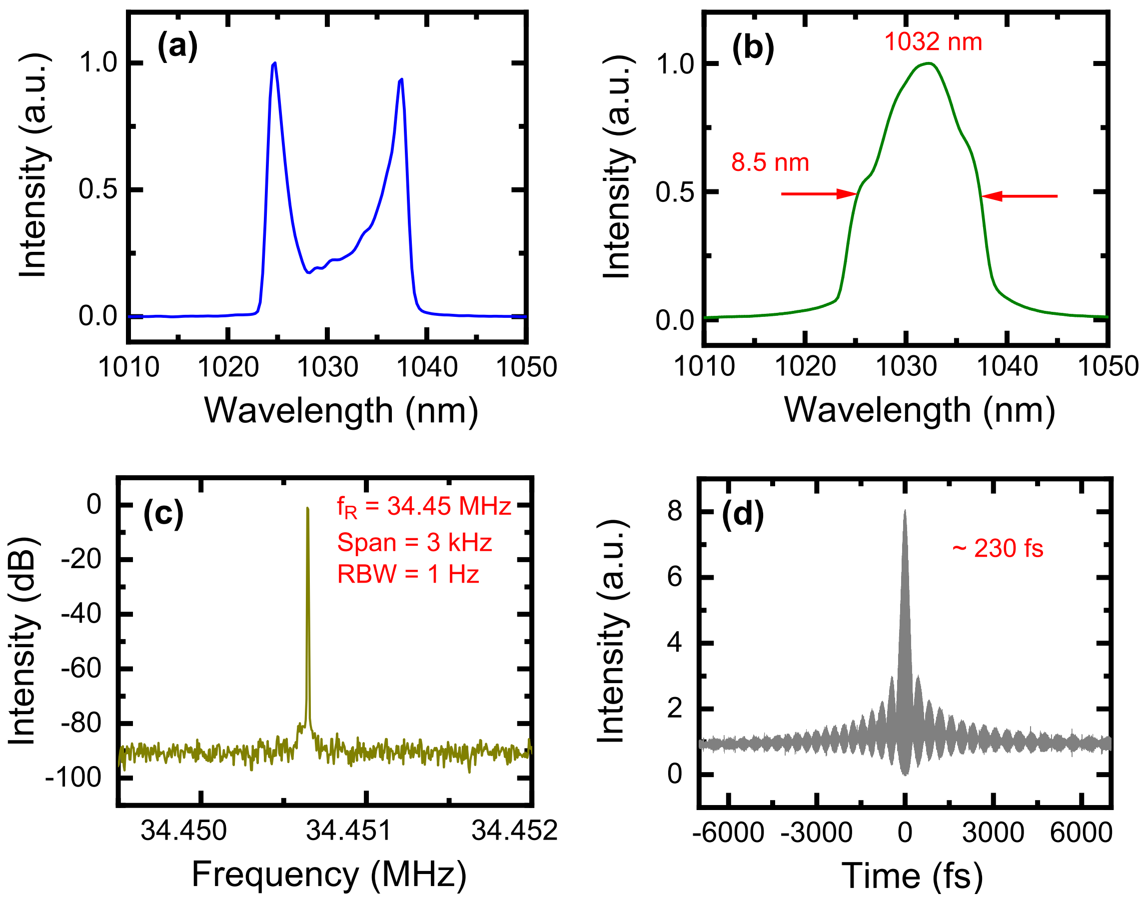

Figure 2.8: Experimental (a) spectrum at the PBS at 350 mW input pump power. (b) spectrum at the 20% port. (c) radio frequency spectrum; f_R: repetition frequency, RBW: resolution bandwidth. (d) Interferometric AC.

distinct difference between the tap port output (Figure 2.9(b)) and the spectrum emitted at PBS is the evidence of the influence of the spectral filter on the pulse circulating inside the cavity. The laser produces a de-chirped pulse duration of 337 fs and the corresponding AC is shown in Figure 2.9(c). The shape of the output spectrum clearly shows the effect of a narrow spectral filter. The output power of the laser is 90 mW. However, the laser is multi-pulsing even at the small input pump power and it can be verified with the RF spectrum analyzer (Figure 2.9(d)). We attribute this behavior to the sinusoidal structure present in the filter transmission (blue curve in Figure 2.7(b)) instead of having a single

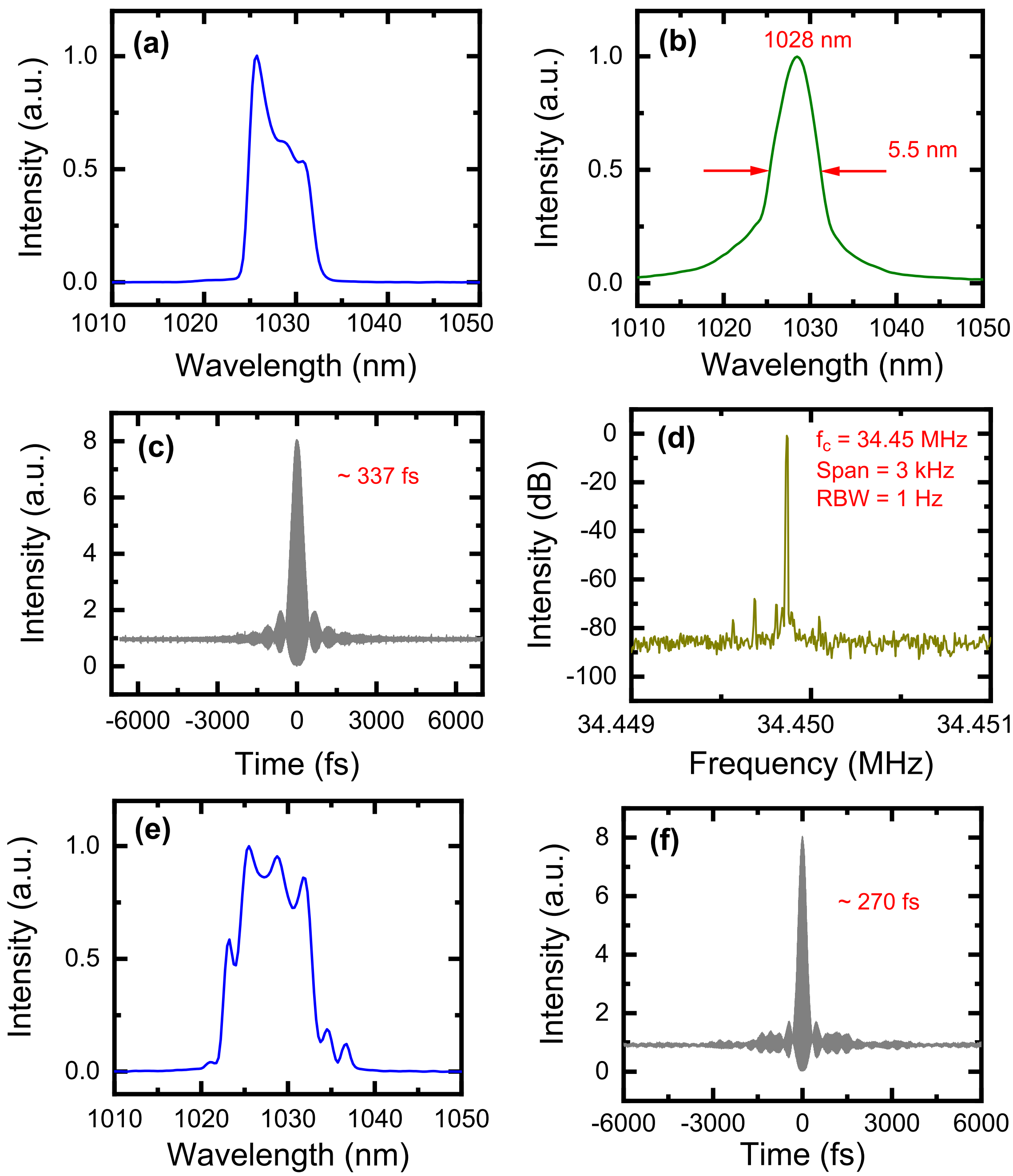

Figure 2.9: Experimental (a) spectrum at the PBS at 220 mW input pump power (b) spectrum at the 20% port (c) AC for the spectrum in (a) (d) RF spectrum showing sidebands as the evidence of multipulsing (e) spectrum at the PBS at 350 mW input pump power (f) AC for the spectrum in (e).

lobe transmission at the laser operating wavelength. Although the spectrum (Figure 2.9(a)) shows steep edges, there is a reduction in them and the spectrum starts developing side lobes at a higher pump power. As the spectral filter is very narrow, it is able to facilitate self-similar mode-locking [16]. Figures 2.9(e) and 2.9(f) show an example of a self-similar spectrum and its AC. The lack of secondary structure in the AC (Figures 2.9(c) and 2.9(f)) compared to the heavy secondary structure in the AC of ANDi spectrum (Figure 4.7(d)) emphasizes that the spectrum obtained with 4.5 nm BW filter is indeed self-similar. This laser operates quite stably, and mode-locking is retained for many hours. If the pump laser is switched off and on again, the laser is able to self start.

It is worth noting that our spectral filter characteristics are dependent on the short PM-SMF-PM section rather than the entire fiber cavities as in Refs. [42, 43, 44]. This supposedly helps to reduce the drift in the filter transmission profile compared to the filters referenced earlier. In the experiments also, we observe that the spectral filter transmission stays the same for several days. One concern is NL effects in the spectral filter when the laser is mode-locked but the experimental observation proves that there is no significant change in the filter transmission when the laser is mode-locked or operated below lasing threshold. Therefore, the linear analysis of spectral filter using Jones calculus is sufficient to predict filter characteristics.

2.5 Temperature sensitivity of the spectral filter

It is known that the birefringence of PM fiber and stressed SMF changes with respect to temperature [48, 49, 50, 51]. Hence, it is important to estimate the temperature sensitivity of our spectral filter. For PM fiber, the birefringence change with temperature is $\sim -1 \times 10^{-7}/^{\circ}$C [49, 51]. For SMF, it is calculated to be $-5.4 \times 10^{-12}/^{\circ}$C using formulas in [48].

The simulation results for the transmission spectra for wideband filter and narrowband filter using these changed birefringence values are shown in Figures 2.10(a) and 2.10(b), respectively. The filter BW remains constant but the center wavelength exhibits a slight blueshift of ~ 0.3 nm /°C as temperature increases. As the experiments are conducted at a fairly constant temperature, they are not affected by the center wavelength shift.

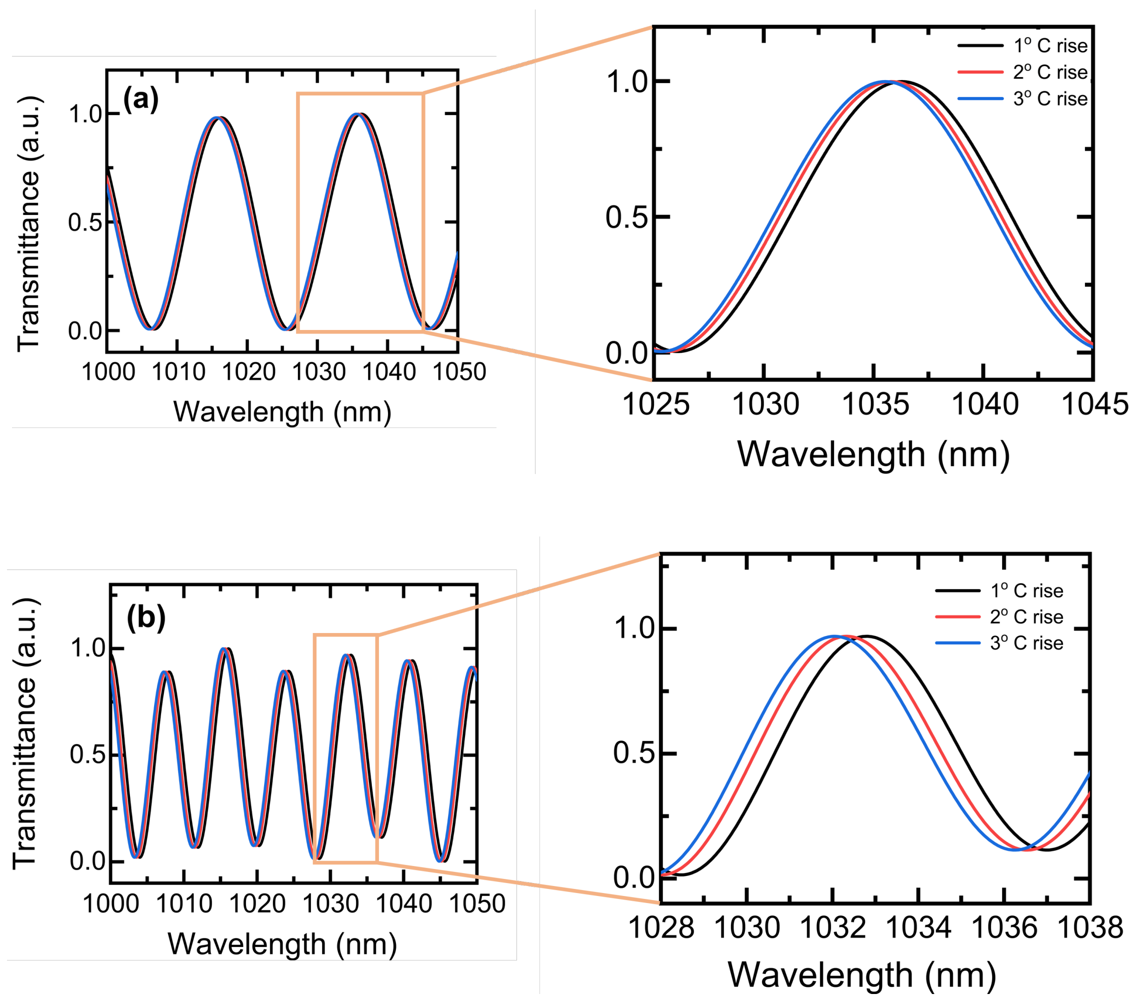

Figure 2.10: Calculated transmission spectra of (a) wideband filter and (b) narrowband filter as a function of temperature. Black, red and blue curves denote the transmission spectra at room temperature, 1 °C, and 2 °C rise in temperature, respectively.

2.5.1 Conclusion

In conclusion, we have designed an all-fiber, tunable BW spectral filter. The tunabilty of the filter BW is based on the birefringence compensation in a fiber based Lyot filter by simply tuning the PC. To the best of our knowledge, this is the first fiber based filter design which can provide BW tunability without rebuilding the filter. We have also used this spectral filter in a Yb laser cavity to generate energetic ultra-short pulses. The laser can demonstrate ANDi operation for wideband filter and even jumps into self-similar operation when the filter BW is narrow. The filter BW discrete tunability can be extended by simply adding more PM-SMF sections. We believe that this simple, compact fiber based filter will play an important role in all-fiber mode-locked lasers to generate versatile output.

CHAPTER III

AN ALL FIBER SPECTRAL FILTER FOR MULTIPULSE STATES MANAGEMENT IN FIBER LASERS

In this chapter, a modified version of the birefringent fiber based filter from Chapter II to control the multipulse dynamics of a fiber laser. Various multipulsing states like harmonic mode-locking and soliton bunches are observed by tuning the spectral filter and the results are presented in this chapter. The interesting point is that the multipulse evolution in this laser relies only on the spectral filter characteristics and it is independent of input pump power and saturable absorber effect.

3.1 Introduction

Controlling the number of ultrafast pulses and the separation between them is important for various applications. For example, in optical communication, the bit rate of digital communication depends on the proximity of individual pulses [52]. For instance, managing a burst of optical pulses is critical in improving the ablation rate in ultrafast micromachining, or producing electron bunches in an accelerator architecture. For such applications, multipulsing states of a mode-locked laser can be useful sources [53]. Multipulsing operations, which are related to the soliton energy quantization, are studied theoretically as well as experimentally extensively. [54, 55, 56, 57]. In the case of ANDi fiber lasers, the pulses can be understood as the dissipative solitons in a normally dispersive medium with a gain and spectral filtering. These lasers can still generate multiple pulses due to pulse energy quantization [35]. The interaction between these pulses is of great interest as they can lead to phenomena like harmonic mode-locking, bound solitons and soliton rains [58, 59, 60, 61, 62, 63].

Soto - Crespo *et al.* showed that a structured shape of a spectral filter could lead to a multipulse phenomenon like bound state solitons [64]. Komarov *et al.* theoretically demonstrated that the interaction between multiple pulses in an ANDi fiber laser can be controlled by introducing an additional narrow spectral selection of intracavity radiation [65]. Haboucha *et al.* identified the spectral gain filtering as a mechanism of multiple pulse formation in passively mode-locked fiber lasers and proposed the idea of introducing a spectral filter with variable bandwidth (BW) in the cavity as to generate multiple pulses [66]. Bao *et al.* implemented the idea of intracavity narrow spectral selection in the form of a dual filter to obtain soliton rains in an ANDi fiber laser. They also observed other multipulsing phenomena by varying multiple parameters such as input pump power, saturable absorber (SA) action and by tuning the dual spectral filter transmission. Hence, there was no clear demonstration that only spectral filter was responsible for all these multipulsing states. The laser had a maximum average output power of 13.28 mW with chirped pulse duration of 3.63 ps [62]. Huang *et al.* also used a dual spectral filter in an all-fiber ANDi laser cavity with graphene oxide as an SA but the formation of multiple pulses was always associated with the simultaneous tuning of the pump power and spectral filter transmission. The average output power of this laser was 0.19 mW and with the repetition period of 933 ns, the overall energy was 0.2 nJ. The energy per pulse can be calculated to be lower than this which is not useful for practical applications [63].

In this chapter, experimental verification of the contribution of a single parameter, spectral filter transmission, in multipulse generation in a mode-locked fiber laser by isolating the effects of other parameters such as pump power and SA is presented. The birefringent fiber-based filter used in these experiments can yield a variety of transmission profiles which eliminates the need for a dual filter used in [62, 63]. Moreover, the performance of this laser is superior (~ 300 fs pulses with 300 mW average output power and > 1 nJ energy per pulse) compared to previous research. Since the control of the multipulsing states is convenient by adjusting the spectral filter transmission, this laser design will certainly find its usage in a variety of applications that require burst mode operation of pulsed lasers.

3.2 The spectral filter design

The spectral filter (shown in Figure 3.1) consists of a section of single mode fiber (SMF), polarization maintaining (PM) fiber and another SMF (SMF1-PM2-SMF2) spliced between two PM fibers that are spliced to in-line polarizers at an angle of 45°. The PCs can be tuned to create a stress induced birefringence in the SMFs. This stress induced birefringence produces a polarization rotation which leads to a variety of transmission profiles. The transmission spectrum of the filter can be simulated using Jones calculus and the transmittance is given by

$$
\begin{aligned}
T = P(\theta_2) \cdot W(\Delta\phi_5) \cdot R(-\Theta_2) \cdot W(\Delta\phi_4) \cdot R(\Theta_2) \cdot W(\Delta\phi_3) \cdot \\
R(-\Theta_1) \cdot W(\Delta\phi_2) \cdot R(\Theta_1) \cdot W(\Delta\phi_1) \cdot P(\theta_1) \quad (3.1)
\end{aligned}
$$

where $P(\theta)$ is the Jones matrix for the polarizer with the axis of transmission making an angle θ with the PM fibers (in this case, 45°). The Jones matrices for PM fibers and SMF are denoted by

$$
W(\Delta\phi) = \begin{pmatrix} e^{-i\frac{\Delta\phi}{2}} & 0 \\ 0 & e^{i\frac{\Delta\phi}{2}} \end{pmatrix} \quad (3.2)
$$

with $\Delta\phi_1$, $\Delta\phi_2$, $\Delta\phi_3$, $\Delta\phi_4$, and $\Delta\phi_5$ being the the phase difference between light propagating between slow and fast axes PM1, SMF1, PM2, SMF2, and PM3, respectively. As SMFs are treated as rotated waveplates for this analysis, a rotator matrix R(Θ) has been used where Θ_1 and Θ_2 are the angles of rotation of polarization inside the SMF1 and SMF2,

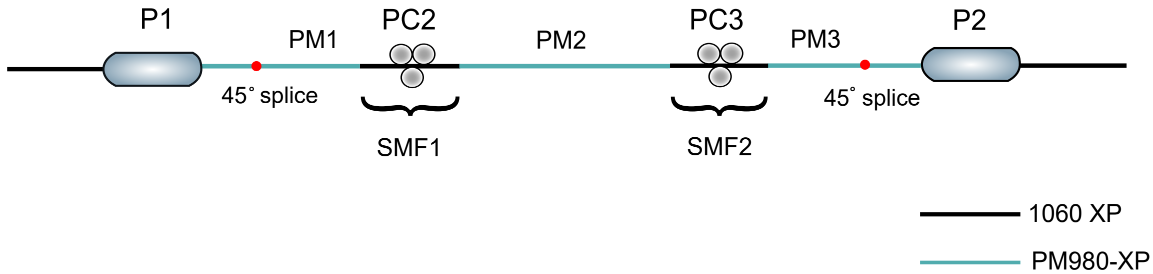

Figure 3.1: Schematic of fiber based spectral filter. P: polarizer, PC: polarization controller, PM: polarization maintaining fiber, SMF: single mode fiber.

respectively. Experimentally, by rotating or squeezing the PCs, the parameters $\Delta\phi_2$, $\Delta\phi_4$, Θ_1, and Θ_2 in Equation 3.1 change and so does the transmission of the filter. A few sample simulated transmission spectra of the proposed spectral filter are shown in Figure 3.2. The lengths of the PM fibers in this filter are 10 cm, 25 cm, and 10 cm, respectively. The length of SMF sections is 14.5 cm each.

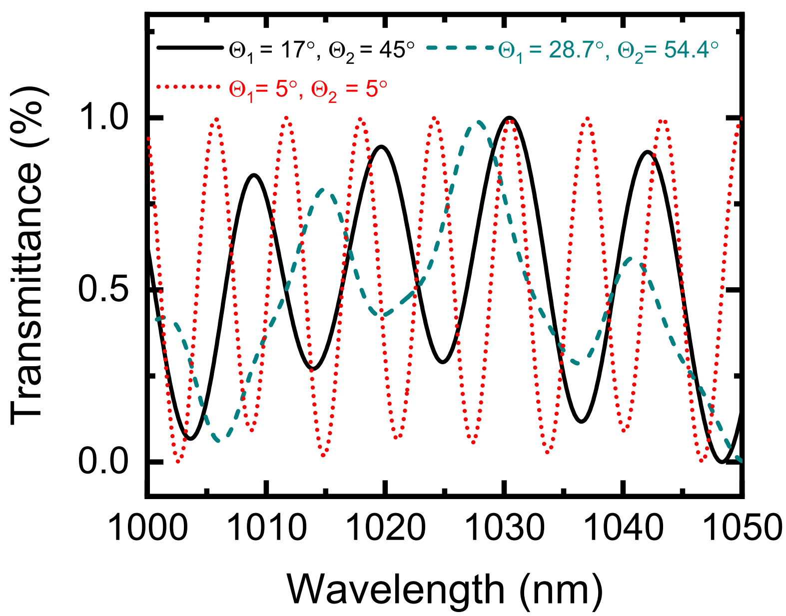

Figure 3.2: Simulated transmission spectra of the filter. The calculated birefringence values for the PM fibers are $\Delta n_1 = \Delta n_3 = \Delta n_5 = 3.6 \times 10^{-4}$. Birefringence values for SMFs (Δn_2 and Δn_5) and the rotation angles (Θ_1 and Θ_2) are variable.

3.3 Experimental results

The experimental configuration of the oscillator is similar to that in Chapter II and is shown in Figure 3.3. The only change in the cavity is regarding spectral filter. The addition of a SMF-PM-SMF section increases the length of the fibers in the cavity. The total length of the fibers in the cavity is 5.54 m and the total cavity dispersion is 0.127 ps^2.

The transmission characteristics of the spectral filter are experimentally observed by following the same method as described in Chapter II. The laser cavity is operated below the lasing threshold at a very low pump power (50 mW). A broadband amplified spontaneous emission (ASE) (shown by a dashed curve in Figure 3.4) is coupled into the spectral filter and the filter output can be observed through the 20% port of the coupler. The PC2 and PC3 are carefully tuned so that the output of the spectral filter has a narrow BW as suggested by Haboucha *et al.* [66]. The solid curve in Figure 3.4 shows the filter output while the inset shows the transmittance of the filter and it closely follows the shape predicted by the simulation (curve T2 in Figure 3.2). Then, harmonic mode-locked operation (3rd

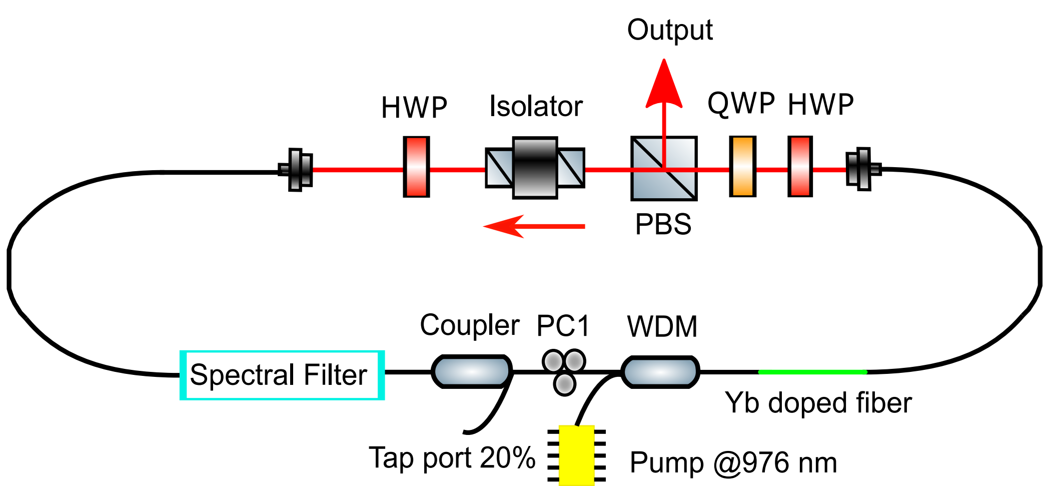

Figure 3.3: The experimental set-up of the fiber laser. PC: polarization controller, HWP: Half waveplate, QWP: Quarter Waveplate, PBS: Polarizing beam splitter.

harmonic) is achieved by rotating intracavity waveplates and tuning PC1 at a pump power of 650 mW. A high input pump power is used to facilitate the observation of multipulsing [57]. A typical output spectrum ejected by the PBS is shown in Figure 3.5(a). The optical spectrum taken at the 20% port of the fiber coupler (Figure 3.5(b)) shows FWHM BW of 6.5 nm. The laser produces a stable pulse train (Figure 3.5(c)) with a 112 MHz repetition rate which is measured by a 650 MHz oscilloscope together with a 1 GHz photodetector. To observe the pulse dynamics more carefully, we used a 6 GHz oscilloscope together with a 20 GHz photodetector and the results are shown in Figure 3.5(d). Figure 3.5(e) represents a radio frequency (RF) spectrum measured with a 500 MHz span and 1 kHz resolution BW. The main peaks occur at the pulse repetition rate (112 MHz) whereas smaller peaks are separated by the fundamental frequency of 37.5 MHz. The laser generates chirped pulses,

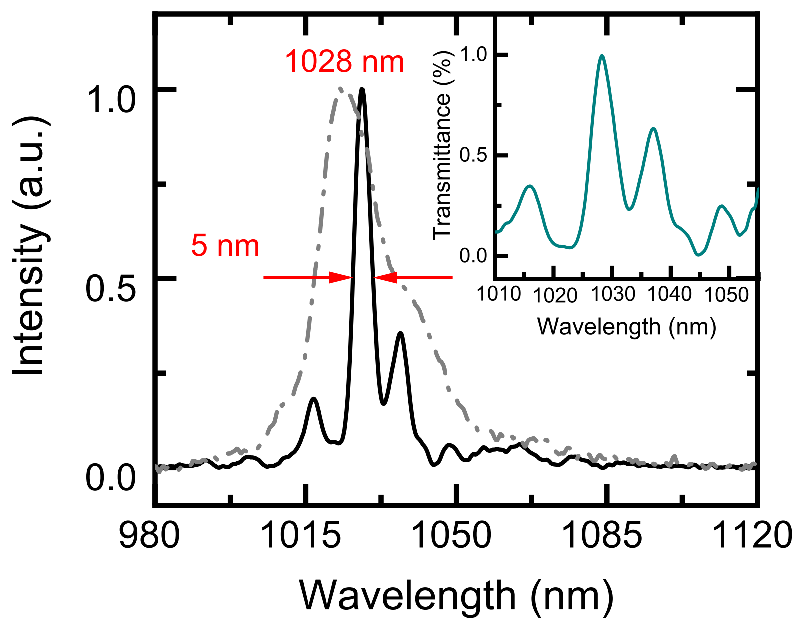

Figure 3.4: Output spectrum of the spectral filter with ASE (dashed line) as input. The inset shows experimental transmittance of the spectral filter.

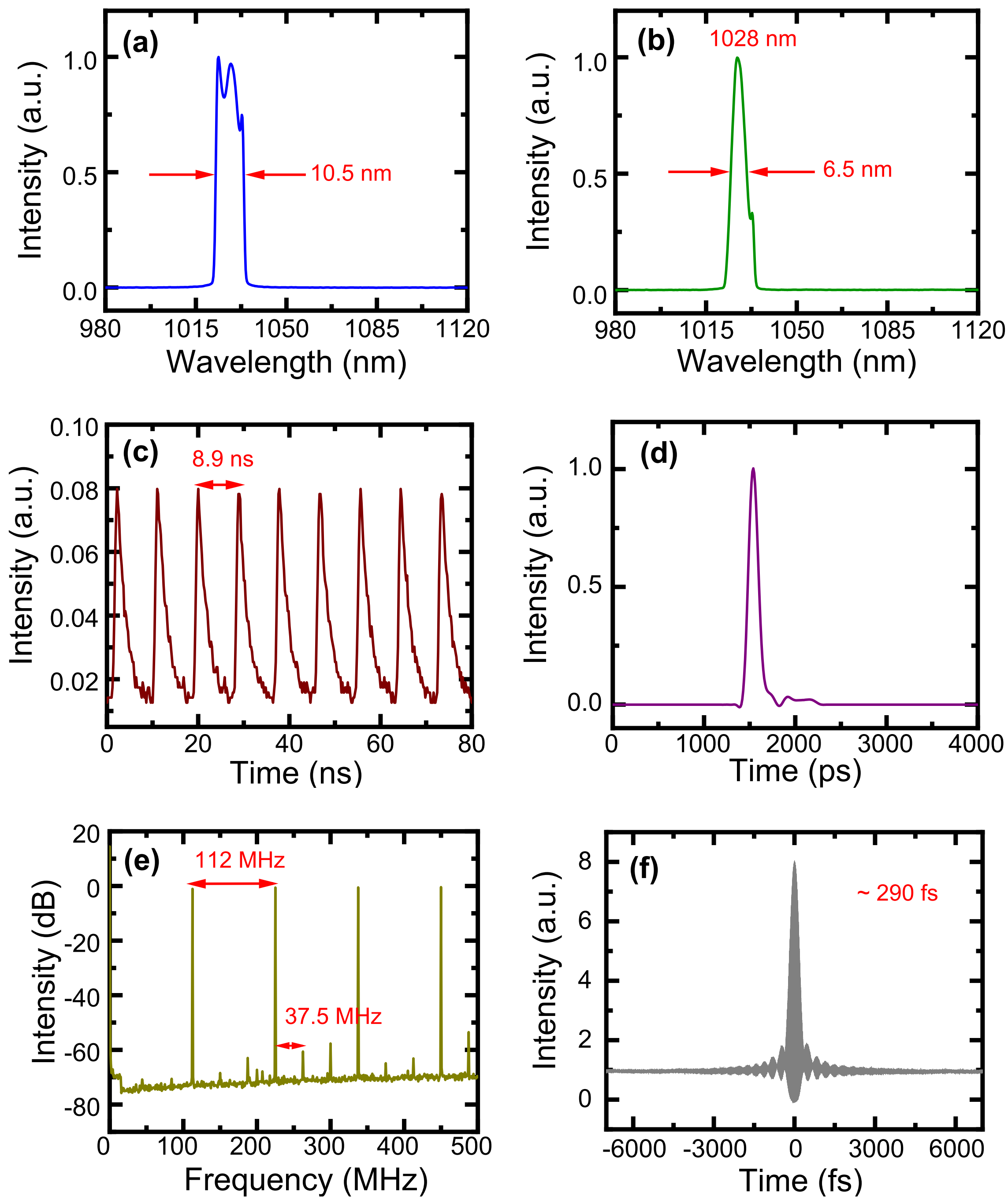

Figure 3.5: Experimental data for the harmonic mode-locking (a) mode-locked spectrum (b) spectrum at the 20% port (c) long range pulse train (d) short range pulse train (e) RF spectrum; span: 500 MHz, RBW: 1 kHz (f) autocorrelation.

which are de-chirped to 290 fs duration with a grating pair outside the cavity (Figure 3.5(g)). The average mode-locked output power is 300 mW, which corresponds to an energy of 2.67 nJ per pulse.

From this mode-locked operation by gradually tuning PC3, the harmonic mode-locking slowly converts in soliton bunch (Figure 3.6(a)). A video depicting the same process is presented in [3]. Now the laser mode-locks at the fundamental repetition rate of the cavity i.e. 37.5 MHz and the corresponding pulse train is shown in Figure 3.6(b). Figures 3.6(c) and 3.6(d) show the RF spectrum with two different spans. Figures 3.6(e) and 3.6(f) show the subtle changes in the spectrum and 20 % port output. Tuning PC3 not only changes the central wavelength of the filter transmission but also BW and the shape of the filter (shown in Figure 3.7) which leads to soliton bunch formation [64, 66]. The inset shows the comparison between filter transmittance when the laser is harmonically mode-locked and when it operating at the fundamental repetition rate. The average mode-locked power stays the same. As there is no significant difference in the spectral BW, the pulse duration is almost the same. From this mode, the number of pulses in a bunch can be varied by tuning either PC2 or PC3 carefully as shown in the video presented in [3]. Up to six pulses obtained are shown in Figure 3.8(a) although the average output power and the repetition rate of the laser remain the same. The corresponding spectra, 20% port output and shape of the spectral filter are shown in Figures 3.8(b), 3.8(c) and 3.8(d), respectively. For any modes, the pulses have a fixed separation value of $\sim$ 285 ps. Figure 3.8(e) shows a clear difference in the shape of the filter transmittance as the number of pulses in the bunch is altered. Sometimes a soliton bunch with hybrid pulse separation is also observed by tuning PC2 or PC3 and a few example pulse trains are shown in Figures 3.9(a) and 3.9(b). Apart from dissipative soliton bunch and harmonic mode-locking, other states can also be

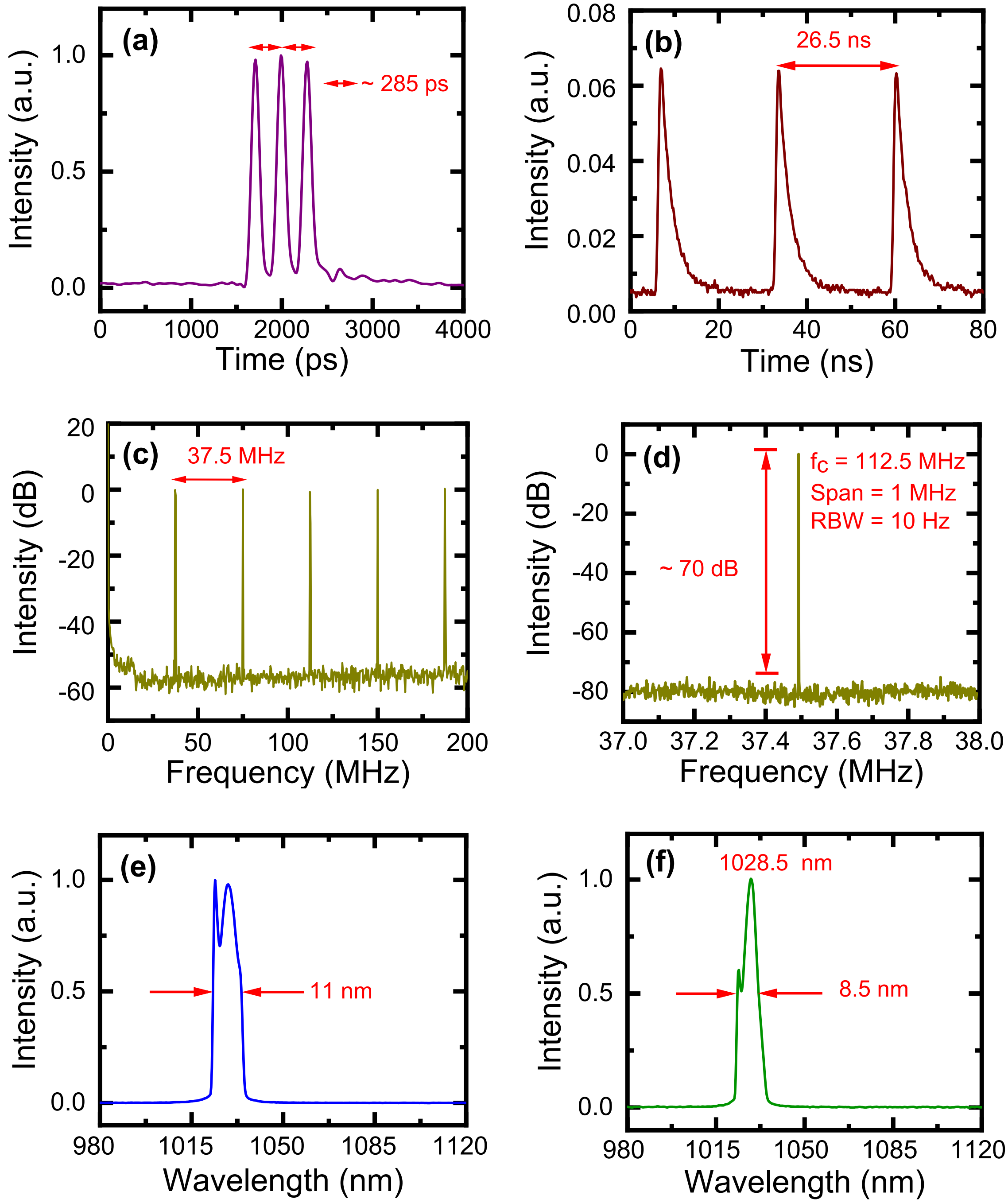

Figure 3.6: Experimental data for the fundamental mode-locking (a) short range pulse train (b) long range pulse train (c) RF spectrum; span: 200 MHz, RBW: 1 kHz (d) RF spectrum over 1 MHz span (e) mode-locked spectrum (f) spectrum at the 20% port.

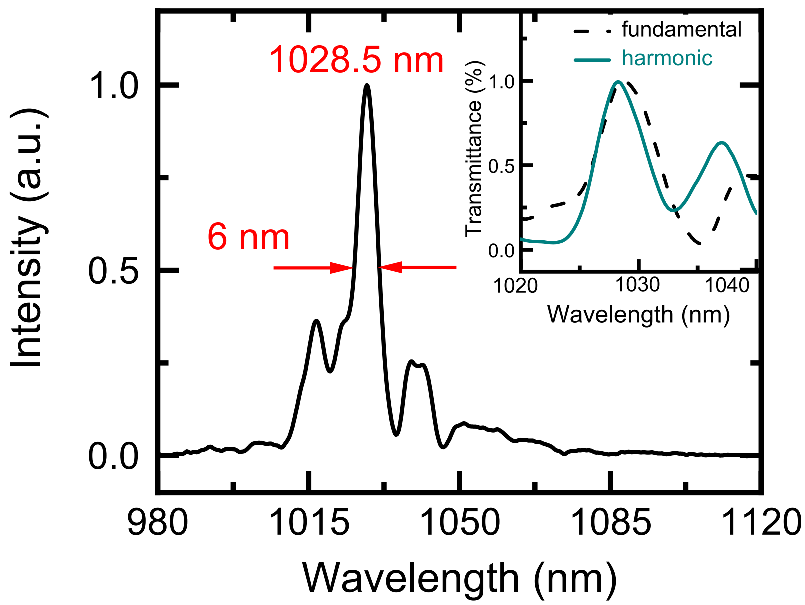

Figure 3.7: Output spectrum of the filter with ASE as input. Inset shows the change in the transmittance of the filter.

observed where multiple pulses exist in the cavity but the separation between them is not constant. The long range and short range pulse train for such non-periodic multipulsing state are shown in Figures 3.10(a) and 3.10(b). The short range pulse train shows that each individual pulse can be a bunch of dissipative solitons. Corresponding spectrum, 20% output, Spectral filter output and the transmittance of the spectral filter are shown in Figures 3.10(c), 3.10(d), 3.10(e) and 3.10(f) respectively.

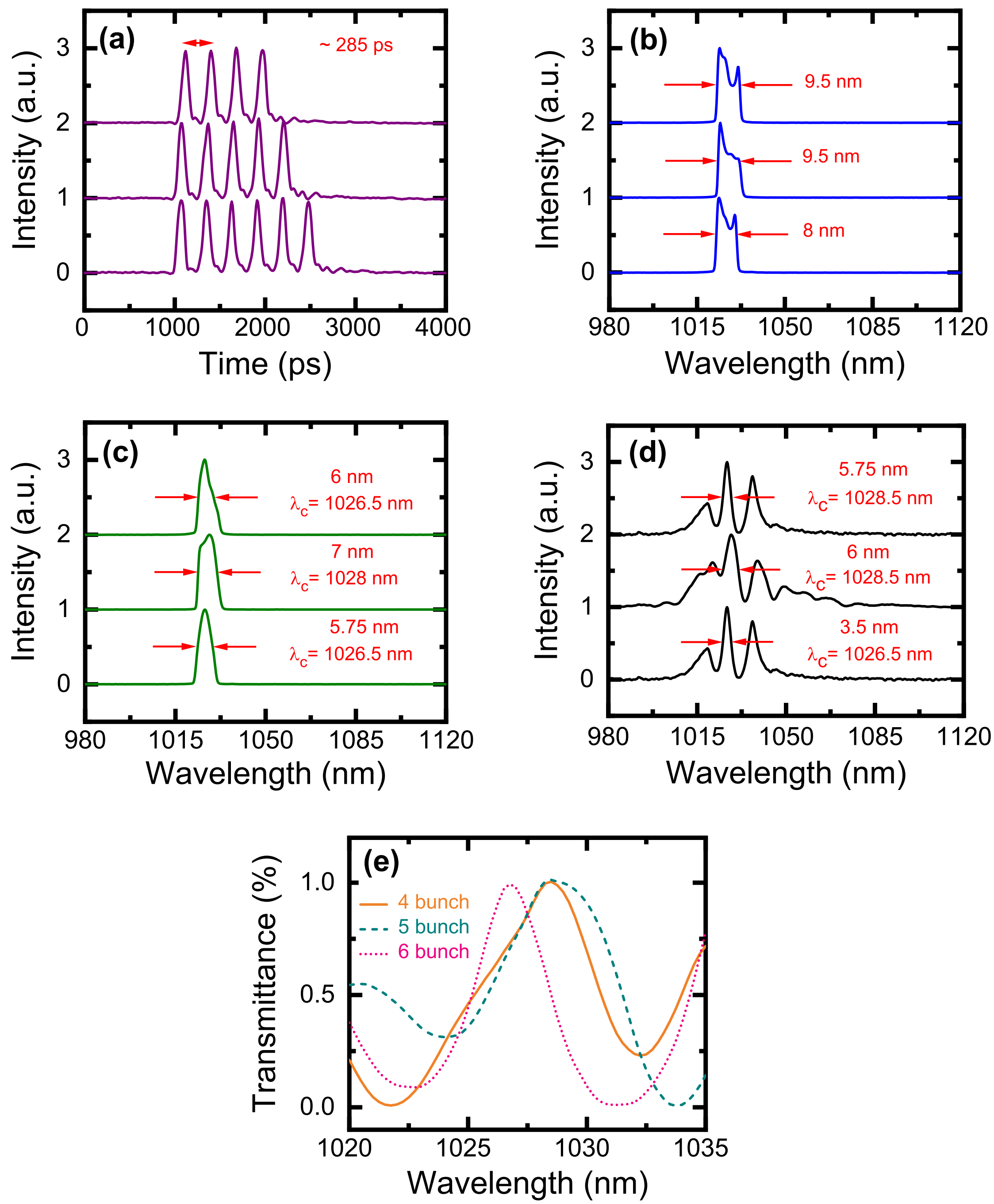

Figure 3.8: Experimental data for the soliton bunch mode-locking (a) short range pulse train (b) mode-locked spectrum at the PBS at 650 mW input power (c) spectrum at 20% port (d) spectral filter output with ASE as input (e) transmittance of the spectral filter.

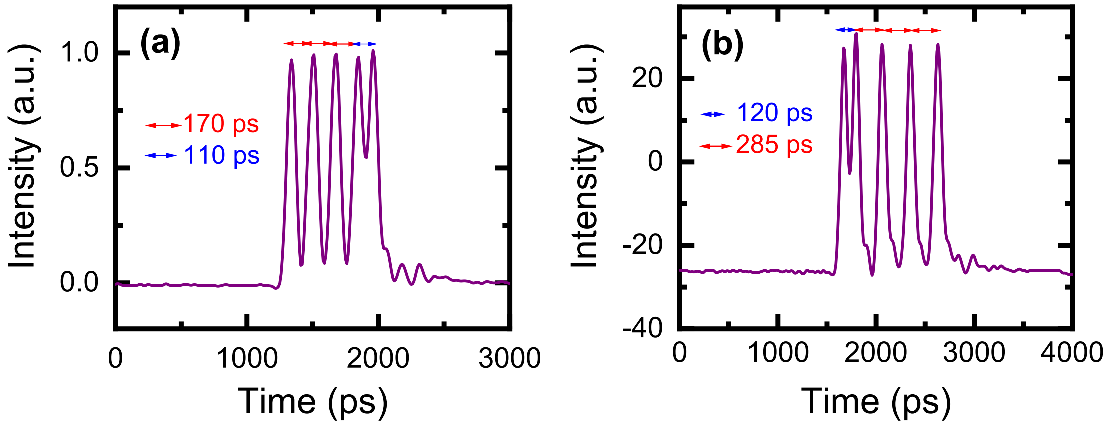

Figure 3.9: Dissipative soliton bunch with hybrid pulse separation of (a) 170 ps and 110 ps (b) 120 ps and 285 ps

3.4 Conclusion

In conclusion, multipulsing operation in an ANDi fiber laser using an all-fiber birefringent spectral filter is demonstrated. By tuning the spectral filter, a harmonically mode-locked state converts into a dissipative soliton bunch and vice versa. The multipulse evolution is clearly due to the change in the transmission characteristics of the spectral filter, especially the BW and the shape, as the laser was operated at a constant pump power and without any changes in the SA. The ability of this laser to produce energetic multiple pulses by controlling a single parameter in the laser cavity will surely make it useful for practical applications.

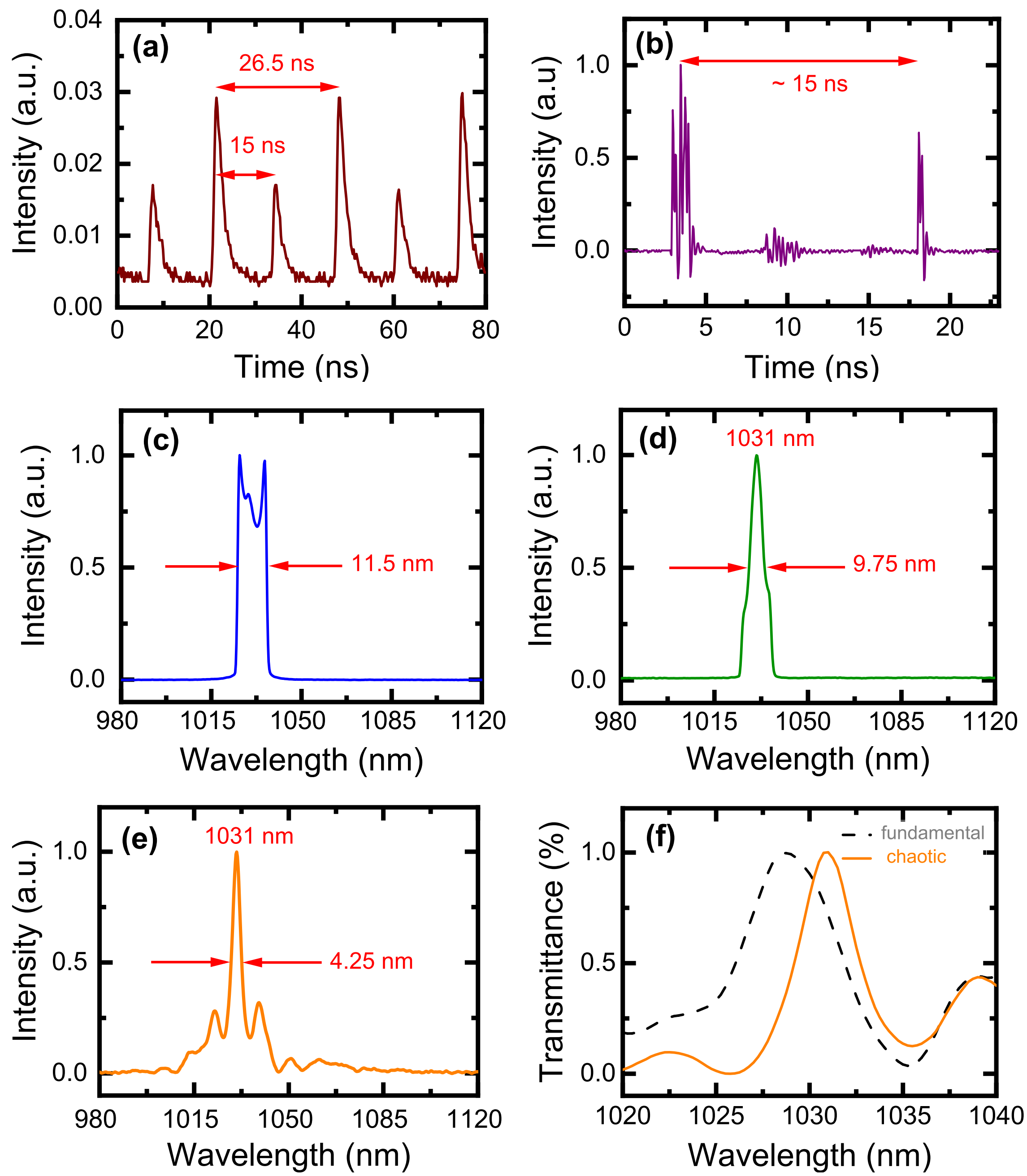

Figure 3.10: Experimental data for the non-periodic mode-locked pulses (a) long range pulse train (b) short range pulse train (c) mode-locked spectrum (d) spectrum at the 20% port (e) output spectrum of the spectral filter with ASE as input (f) Comparison of the spectral filter transmittance.

CHAPTER IV

COMPLEX SWIFT HOHENBERG EQUATION BASED DISSIPATIVE SOLITON FIBER LASER

Complex Swift Hohenberg Equation (CSHE) has attracted intensive research interest over the years as it enables realistic modeling of mode-locked lasers with saturable absorbers by adding a fourth order term to the spectral response. Many researchers have reported a variety of numerical solutions of CSHE which reveal interesting pulse patterns and structures. In this chapter, a CSHE dissipative soliton fiber laser is demonstrated experimentally using combination of the birefringent spectral filter described in Chapter III and a bandpass filter (BPF). Also, numerical simulations are performed and the behavior and performance of the laser agree qualitatively with these numerical simulations. These findings bring insight into dissipative soliton dynamics and make our mode-locked laser a powerful testbed for observing dissipative solitons of CSHE, which may open a new course in ultrafast fiber lasers research.

4.1 Introduction

The cubic quintic Ginzberg Landau equation (CQGLE) can undoubtedly be used to describe a vast number of systems such as passively mode-locked lasers with fast saturable absorbers, parametric oscillators, wide aperture lasers, nonlinear optical transmission lines and nonlinear cavities with the external pump [67, 68, 69]. In the CQGLE model, spectral filter transmission can be described by a quadratic term which leads to a Gaussian response. In the reality, the spectral filtering effect in mode-locked fiber lasers is a combination of gain spectrum and physical spectral filtering element inserted in the cavity and the gain spectrum can exhibit non-uniform features. Therefore, to represent this condition it is necessary to include higher order terms while defining the profile of the spectral filter. The addition of a fourth order spectral filtering term in the CQGLE model converts it into the complex Swift Hohenberg equation (CSHE).

The CSHE has played an important role in outlining pulse dynamics of various nonlinear optical systems like large aspect lasers [70], photorefractive materials [71], semiconductor lasers [72], and passively mode-locked ultrafast lasers [73]. Despite the fact that some of the exact solutions of the CSHE can be obtained analytically [74], it seems that the CSHE can mainly be analyzed using numerical simulations [68, 64, 75]. Soto-Crespo *et al.* employed a fourth order spectral filter in numerical simulations and found a great variety of soliton solutions such as composite pulses and moving solitons at anomalous dispersion [64]. In 2016, Latas reported numerical high energy soliton solutions of CSHE in both normal and anomalous dispersion regimes [76]. The energy of conventional solitons generated in anomalous dispersion laser cavities is fundamentally limited according to the soliton area theorem [8, 7]. These conventional solitons suffer pulse break-up in the case of excessive nonlinearity. The solution of CSHE at anomalous dispersion is dissipative solitons which are less susceptible to the optical nonlinearities avoiding pulse breaking, thus can have high energy compared to the conventional solitons. Moreover, they possess linear chirp which can be easily compensated to obtain ultrafast pulses. Therefore, the numerical result regarding high energy dissipative solitons at anomalous dispersion in Ref. [76] is particularly encouraging. Latas *et al.* also numerically analyzed erupting soliton solutions of CSHE by tuning the parameters of the spectral filter profile and higher order effects [77]. In another noticeable effort, Zhao *et al.* numerically simulated a ytterbium (Yb) doped fiber laser cavity with a fourth order spectral filter to obtain dissipative soliton resonance pulses [78]. Although extensive work has been already done numerically analyzing CSHE, very few efforts have been carried out for experimentally implementing a CSHE dissipative soliton fiber laser. Bao *et al.* were successful in observing switching dynamics of two dissipative soliton solutions of an erbium (Er) mode-locked fiber laser and they discovered that the spectral filter with multiple transmission peaks was one of the critical parameters for the presence of this bistability [79]. Zhou *et al.* used composite filtering effect in an Er, Yb co-doped mode-locked fiber laser to observe the mode-locked output to switch from a single soliton to a bound soliton state [80]. Both the papers focused more on the effect of a higher order spectral filter on the pulse switching dynamics, but they did not analyze the mode-locked spectrum or pulse further to verify whether the laser output exhibited any similarity to the dissipative solitons of CSHE.

One of the obstacles in realizing a CSHE fiber laser is the unavailability of a commercial fourth order spectral filter. In Ref. [80], three filters were combined to produce a composite filtering effect and implementing such a complicated filter in a ring resonator is not feasible. Recently, we reported a birefringent fiber based bandwidth tunable spectral filter which can generate a variety of transmission profiles [2, 3]. This filter can control the value of the minimum in the spectral dip, the distance between the two maxima in the spectral response as well as asymmetric maxima which can not be easily duplicated in a thin film dielectric optical filter. In this research, the same fiber based spectral filter is used along with a BPF to produce a higher order spectral filter response which is then used in a Yb doped fiber laser cavity that generates stable mode-locked pulses. These pulses are believed to be the moving soliton solutions of the CSHE as they depict asymmetric temporal profile as well as a highly asymmetric spectrum as predicted by Soto - Crespo *et al.* [64]. To the best of our knowledge, this is the first demonstration of CSHE dissipative soliton fiber laser thus a first step in studying the effects of higher order spectral filtering in mode-locked fiber lasers. This laser will provide an excellent platform to study the rich dynamics of dissipative solitons of CSHE.

4.2 Experimental Setup

The experimental setup for the CSHE dissipative soliton fiber laser is sketched in Figure 4.1. A wavelength division multiplexer (WDM) couples a 976 nm pump into a 55 cm of Yb gain fiber followed by 1 m of single mode fiber (SMF). The mode-locking relies on a

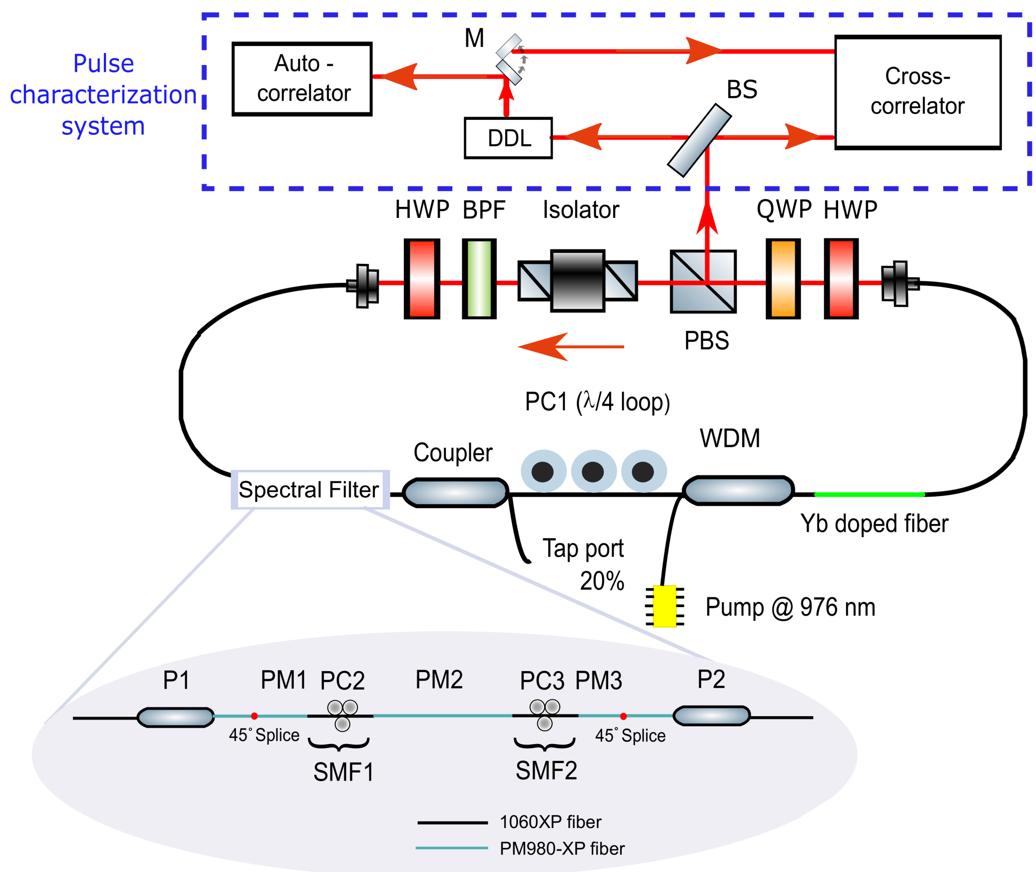

Figure 4.1: Schematic of the fiber oscillator along with the pulse characterization system. PBS, polarizing beam splitter; BPF, bandpass filter; HWP, half wave plate; P, in-line polarizer; PM, polarization maintaining; SMF, single mode fiber; PC, polarization controller; WDM, Wavelength Division Multiplexer; QWP, quarter waveplate; BS, beam splitter; DDL, dispersion delay line; M, filp mirror.

nonlinear polarization evolution based saturable absorber in the form of a polarization controller (PC1), a half waveplate (HWP), a quarter waveplate (QWP), and a polarizing beam splitter (PBS). An isolator ensures the unidirectional operation of the laser. In order to create a fourth order spectral filter transmission, a dual filter combination was used. The first filter is a birefringent fiber based bandwidth tunable spectral filter (shown in Figure 4.1). The lengths of the polarization maintaining (PM) fibers in this filter are 10 cm, 25 cm, and 10 cm, respectively and the length of SMF sections is 14.5 cm each. This spectral filter combined with a 10 nm full width half maximum (FWHM) BPF gives a spectral response with two maxima. An 80/20 fused coupler is used to verify this spectral response. The total length of the fibers in the cavity is 5.54 m and the total cavity dispersion is 0.127 ps^2.

4.3 Numerical simulation results

In this section, numerical simulations are performed for the laser configuration shown in Figure 4.1. This cavity is best described by CSHE given by Equation 4.1 as it contains a fourth order filter. Readers may want to compare results of this simulation to the CQGLE fiber laser simulation. They may refer to [34] for such simulation results of a normal dispersion fiber laser with a Gaussian spectral filter.

$$\frac{\partial A}{\partial z} = -i\frac{\beta_2}{2}\frac{\partial^2 A}{\partial T^2} + \frac{\beta_3}{6}\frac{\partial^3 A}{\partial T^3} + i\gamma_2|A|^2A + i\nu|A|^4A + \epsilon|A|^2A + \mu|A|^4A + gA + \left[\delta A + \beta\frac{\partial^2 A}{\partial T^2}A_{tt} + \gamma\frac{\partial^4 A}{\partial T^4}\right] \quad (4.1)$$

where $|A|$ is proportional to the electric field envelope of the pulse such that $|A|^2$ is its power, z is the propagation distance and t is the retarded time. β_2 is the group velocity dispersion coefficient while β_3 is the third order dispersion coefficient of the fiber. γ_2 represents the Kerr self-focusing nonlinearity, ν is the quintic nonlinearity, which is set to zero in this case.

ϵ and μ are related to saturable absorption. g is the gain saturation and it is given by

$$g = \frac{g_0}{1 + \frac{E}{E_{sat}}} \tag{4.2}$$

where E is the pulse energy given by

$$E = \int_{\frac{-T_R}{2}}^{\frac{T_R}{2}} |A|^2 dt \tag{4.3}$$

where T_R is the cavity round trip time, E_{sat} is the saturation energy, and g_0 is the small signal gain. The terms containing δ, β, and γ describe the spectral response, the transmission of which is given by

$$T(\omega) = e^{(\delta - \beta\omega^2 + \gamma\omega^4)}. \tag{4.4}$$

The main difference between the CSHE and the CQGLE lies in the fourth order spectral filtering term with γ. With γ set to zero and with a positive β, a single peak spectral filter can be obtained whereas a positive γ and a negative β yield a spectral response with two maxima. Figure 4.2 shows the parameters of the spectral filter used in the simulation along with the spectral filter in the CQGLE model with the same bandwidth as the former one.

We assume the initial pulse shape to be hyperbolic secant for our simulations. The fiber parameters considered for the simulation roughly follow the experimental condition and they are: $\gamma_2 = 0.0047$ W$^{-1}m^{-1}$ for SMFs and YDFs and $\beta_2 = 23fs^2$/mm and $\beta_3 = 63.8fs^3$/mm for SMFs and YDFs. The other simulation parameters are g_0 which corresponds to 30 dB of small signal gain and E_{sat} = 900 pJ. The output coupler has a 70 : 30 coupling ratio. The saturable absorber used in the simulation is a monotonic saturable absorber with the transmittance $T = 1 - q_0/[1 + P(t)/P_{sat}]$ where q_0= 1 is the modulation depth, P(t) is the instantaneous pulse power and P_{sat} = 0.7 kW is the saturation power. Figure 4.3(a) shows the result of propagating the initial pulse profile over the number of roundtrips (N) which quickly converges to a pulse profile that is asymmetric in shape with unequal

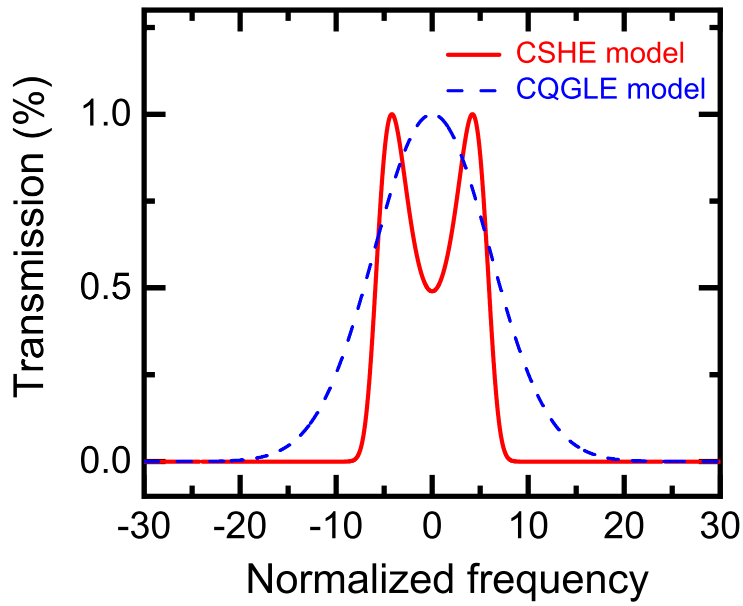

Figure 4.2: Spectral filter transmission $T(\omega) = e^{(\delta-\beta\omega^2-\gamma\omega^4)}$ in the CQGLE model (dashed curve) with δ = 0, β = 0.012 and γ = 0 and in the CSHE model (Solid curve) with δ = -0.7133, β = -0.0809 and γ = 0.0023

shoulders. Interestingly, this is a moving pulse solution depicted in [64]. The pulse energy after spectral filter as a function of round trip propagation is plotted in Figure 4.3(b) and this figure implies that the pulse quickly converges to a steady state. The pulse, spectrum and chirp evolution inside the cavity at some specific locations is shown is shown in Figure 4.3(c). OC represents output coupler which is essentially the signal ejected by the PBS.

By slightly changing the saturable energy of the gain fiber and saturation power of the saturable absorber, it is possible to get a slight different steady state solution. It is important for us to observe the pulse evolution at the output (Location: OC) and therefore, the pulse evolution throughout the entire cavity is not shown here. Instead, Figures 4.4(a) and 4.4(b) shows the comparison between these two steady state output spectra and pulses, respectively. The spectrum associated with the second steady state evolution shown by the

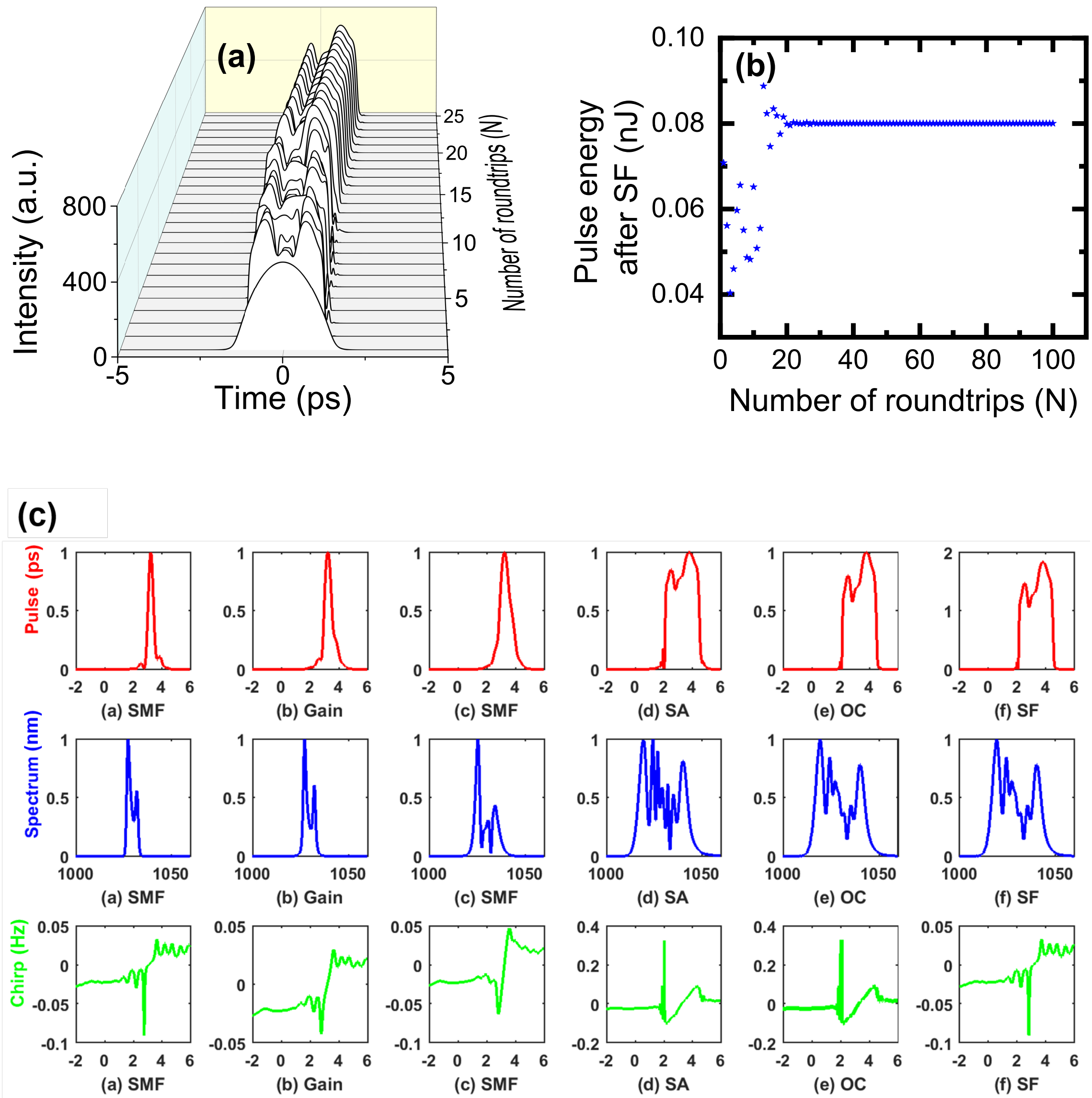

Figure 4.3: Numerical simulation results (a) pulse evolution in the presence of the spectral filter with respect to roundtrips (b) The pulse energy after spectral filter along with round trip propagation for the laser cavity. The convergence to a steady state is achieved at N=20. (c)The steady state evolution after each component inside the cavity. Top row: the shape of the pulse. The pulse is asymmetric and moving. Center row: the spectral evolution. The spectrum at each location in the cavity is asymmetric. Bottom row: The chirp associated with the pulse. The chirp shows a clear sign of wavebraking at the edges of the pulse.

solid black curve in Figure 4.4(a)] is more asymmetric than the first simulated case. It is also noted that the pulses associated with this spectrum [shown by the black curve in Figure 4.4(b)] are moving a little slower (more negative velocity) than the pulse from the first simulated case shown [depicted by blue curve in Figure 4.4(b)]. Figures 4.4(c) and 4.4(d) present the same conclusion. This behavior agrees with the observation in [64] that the greater the asymmetry of the spectrum, the higher is the velocity of moving pulses irrespective of the sign of the velocity.

It should be noted that β_3 is considered in this simulation to trigger the asymmetric pulse generation. In the absence of β_3, the initial symmetric pulse does not evolve into an asymmetric pulse. Alternatively, one can use an initial simulation condition similar to [64] i.e. hyperbolic secant pulse profile with an asymmetric phase (i.e. a pulse with an initial velocity) which will result in an asymmetric output pulse. We prefer β_3 to be the asymmetry trigger over the initial pulse with asymmetric phase as it is a better match to the experimental conditions. One may think that the β_3 is the cause of temporal and spectral asymmetry in the CSHE simulation results presented in Figure 4.3. On the contrary, fourth order spectral filter is the main reason for the output pulse and spectrum to be asymmetric. It is already studied that including β_3 in the CQGLE simulation has very little or no influence on the output pulse [81]. This proves that a filter with Gaussian response is incapable of generating an asymmetric moving pulse solution even if the β_3 is taken into account and therefore, asymmetric moving soliton solution can be tied to the fourth order spectral filter.

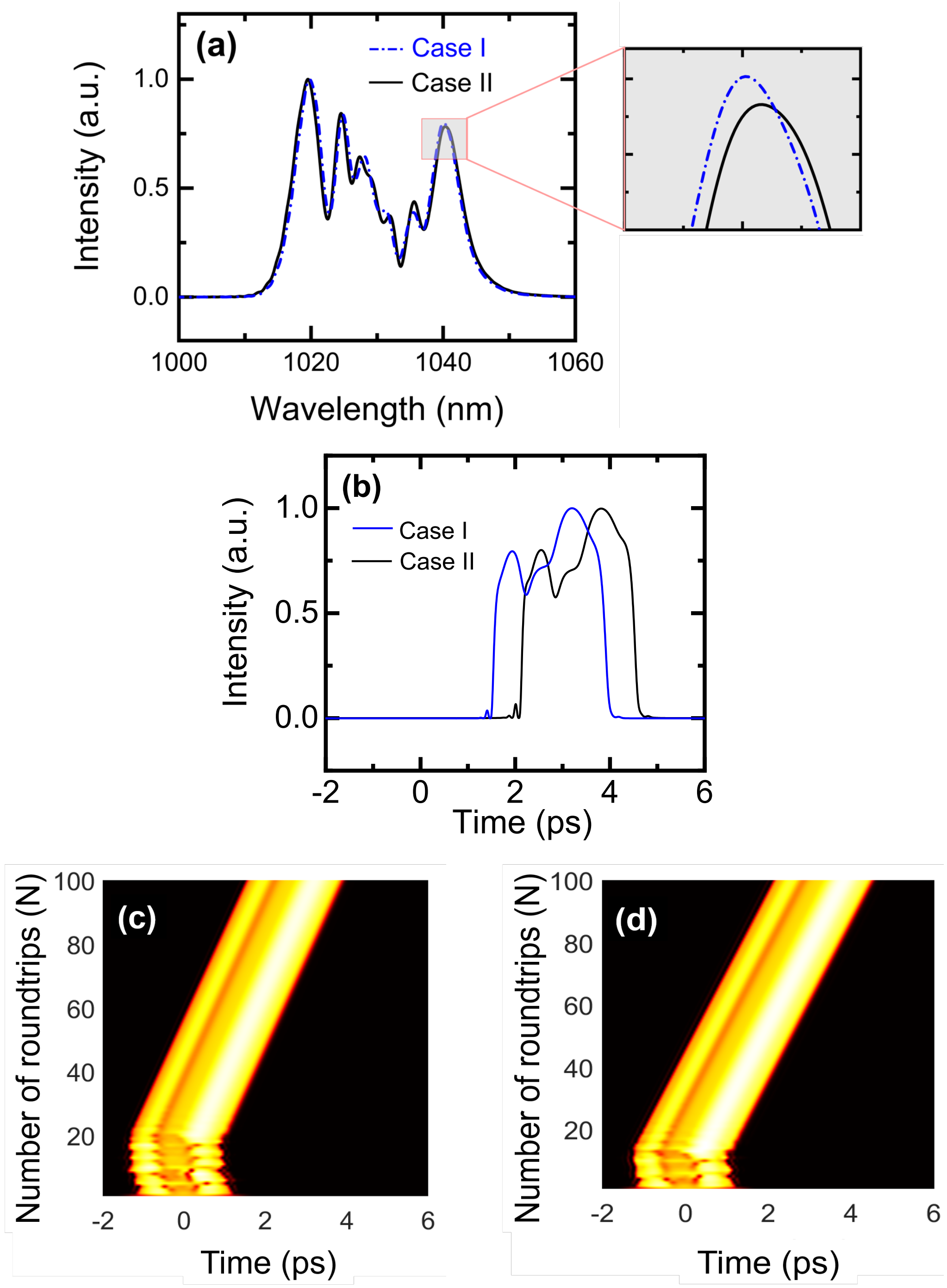

Figure 4.4: Numerical simulation results (a) asymmetric mode-locked spectrum (dashed blue curve) pertaining to the moving pulse solution in the first simulated case and more asymmetric mode-locked spectrum (solid black curve) related to different simulation parameters. The inset shows the asymmetry at the longer wavelength tail of the spectra (b) comparison with the two pulse profiles (c) temporal dynamics of the moving pulse solution related to the less asymmetric mode-locked spectrum pertaining to the first simulated case (d) amplitude contour plot for the pulses moving with a higher velocity associated with the more asymmetric spectrum.

Initially, the laser cavity is operated below the lasing threshold at a pump power of 50 mW to observe the transmission profile of the spectral filter by coupling amplified spontaneous emission (ASE) (shown by a dashed curve in Figure 4.5) into the spectral filter and observing the filter output through the 20 % port of the fiber coupler. The PC2 and PC3 are carefully tuned so that the output of the spectral filter exhibits a multiple peak structure with a dip at 1030 nm (dotted curve in Figure 4.5). Although this spectral filter transmission shows multiple peaks around 1030 nm, the laser fails to mode-lock using such a filter. It could be attributed to the two factors - the wide bandwidth of the filter transmission and the presence of unwanted sinusoidal structure in the filter transmission. To mitigate this problem, a BPF with 10 nm FWHM bandwidth is introduced in the cavity

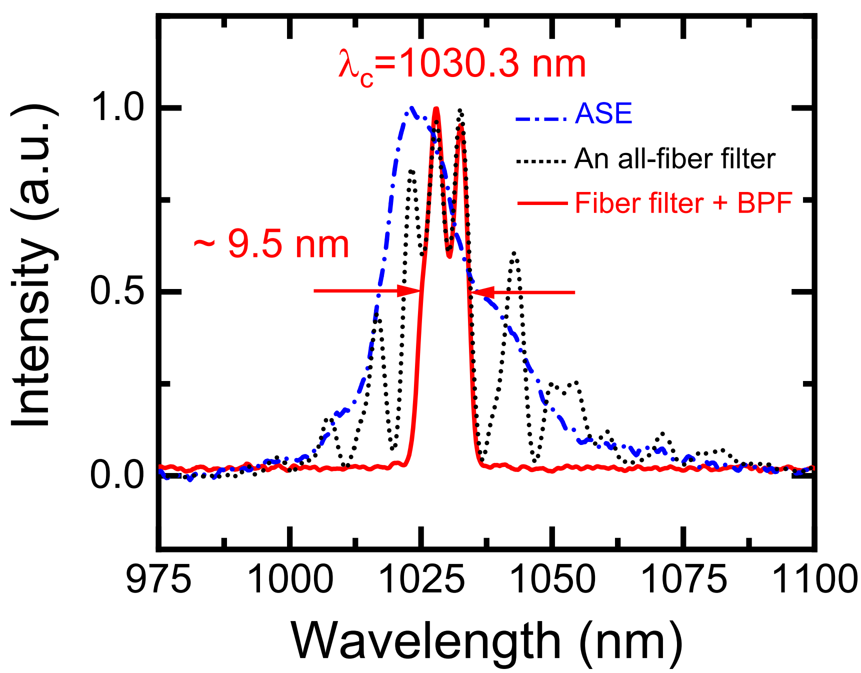

Figure 4.5: Output of the fiber based filter and BPF combination (solid curve) with ASE (dashed line) as input. The dotted line depicts the output of fiber based filter only.

to select a double peak transmission out of the multi-peak structure and the resulting shape of the spectral filter is presented by the solid curve in Figure 4.5. The same spectral filter response is used in all the experiments discussed in this work.

The initial mode-locking is obtained by rotating intracavity waveplates and by adjusting PC1 at a pump power of ~ 400 mW. But this initial mode-locked spectrum is not very stable for the long duration of the experiments and hence the pump power is increased. A stable mode-locking is achieved at 545 mW of input pump power and the output spectrum ejected by the PBS is recorded and shown in Figure 4.6(a) and as predicted by simulation, it is asymmetric and much wider than the spectral filter. The optical spectrum taken at the 20 % port of the fiber coupler is displayed in Figure 4.6(b) and it proves that the spectrum circulating the laser cavity always remains asymmetric. The output pulse profile is measured performing a cross-correlation between the chirped pulse directly emitted from the laser and the de-chirped pulse obtained from a grating pair compressor and it is presented in Figure 4.6(c). It matches with the numerical simulation in terms of the asymmetric structure with the unequal shoulders. The laser produces a stable pulse train [Figure 4.6(d)] with ~ 37.5 MHz repetition rate. The average mode-locked output power is 75 mW, which corresponds to a pulse energy of ~ 2 nJ. Figure 4.6(e) depicts a radio frequency (RF) spectrum measured with a high-resolution RF spectrum analyzer (Agilent N9914A). There are no residual sidebands at least 70 dB below the carrier. Also, stable single pulsing is verified with a ns photodiode and by monitoring the interferometric autocorrelation. The de-chirped pulse duration is ~ 125 fs [Figure 4.6(f)]. Another mode-locked spectrum is obtained by slightly changing the orientation of the HWP from the saturable absorber and at an increased pump power. This slightly broad mode-locked spectrum is illustrated in

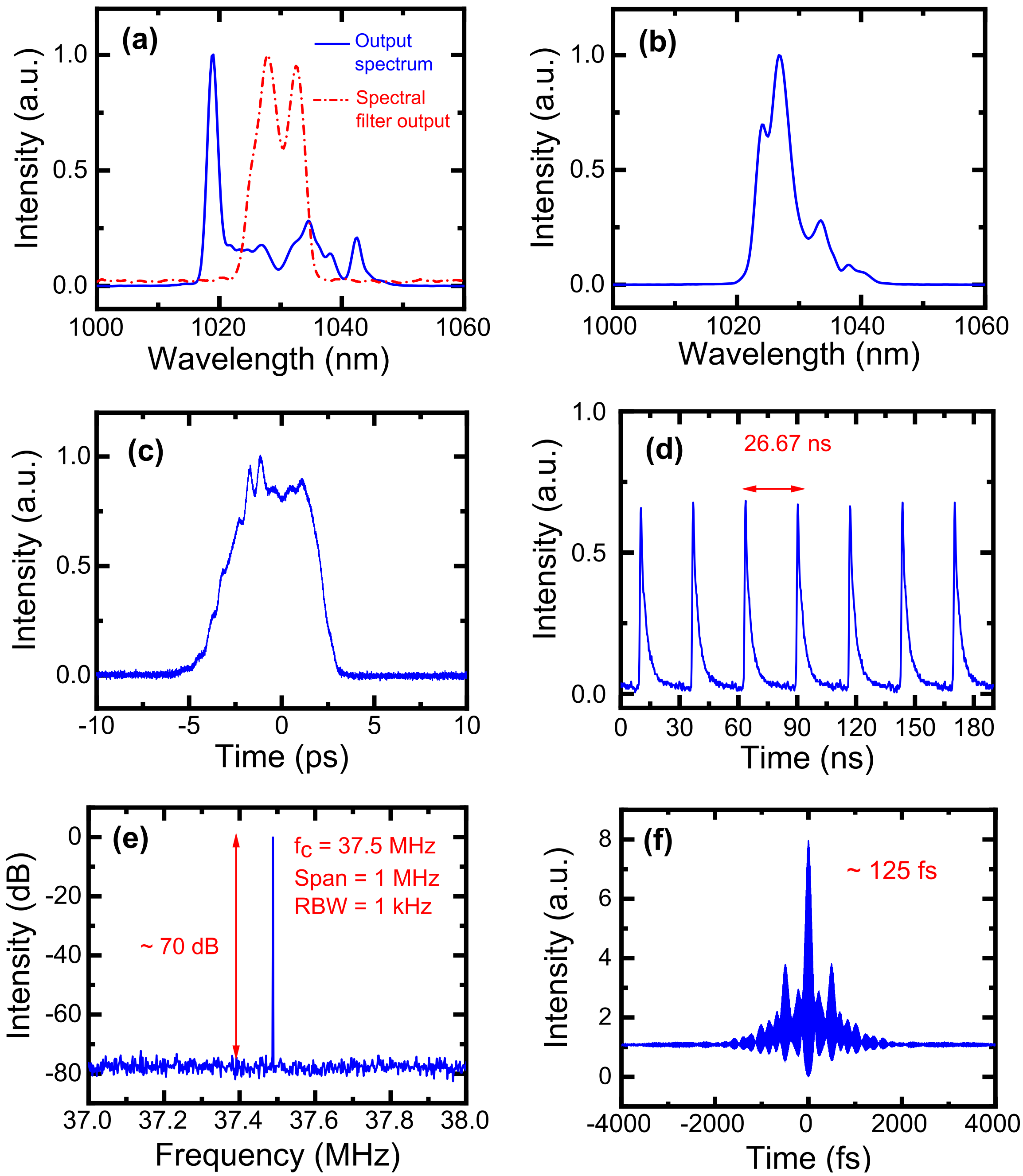

Figure 4.6: Experimental dataset recorded at 545 mW of input pump power (a) mode-locked spectrum at the PBS (solid curve) along with the spectral filter response (dashed curve) (b) spectrum obtained at the 20 % port of the fiber coupler (c) cross-correlation of the output pulse (d) pulse train (e) RF spectrum (f) autocorrelation.

Figure 4.7 (a) at the maximum pump power of 571 mW. It is important to note that the spectrum and pulse [Figure 4.7(b)] still retain their asymmetric profiles. Figure 4.7(c) displays the spectrum at the 20 % port of the coupler. The interferometric autocorrelation in Figure 4.7(d) shows that the pulse width has narrowed down a little to $\sim$ 110 fs. The average mode-locked output power is 105 mW which corresponds to a pulse energy of $\sim$ 2.8 nJ.

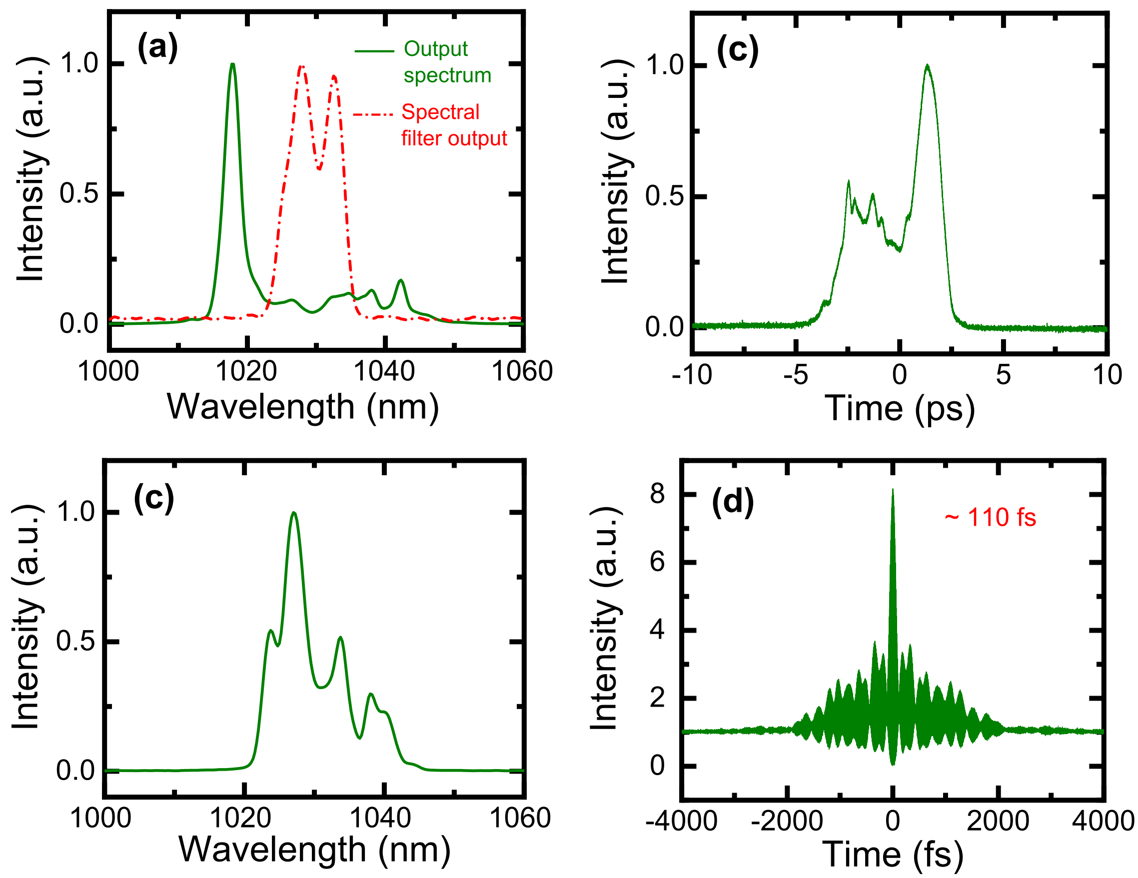

Figure 4.7: Experimental dataset recorded at 571 mW of input pump power a) mode-locked spectrum with a spectral filter response (dashed curve) (b) cross-correlation of the output pulse (c) spectrum obtained at the 20 % port of the fiber coupler (d) autocorrelation.

Figure 4.8(a) offers insight into the asymmetry between the two mode-locked spectra. Spectrum 1 is less asymmetric than the spectrum 2, therefore it is expected that the solitons associated with the spectrum 1 will move slightly faster than the ones associated with the spectrum 2. This is verified by observing change in the repetition rate of the laser.

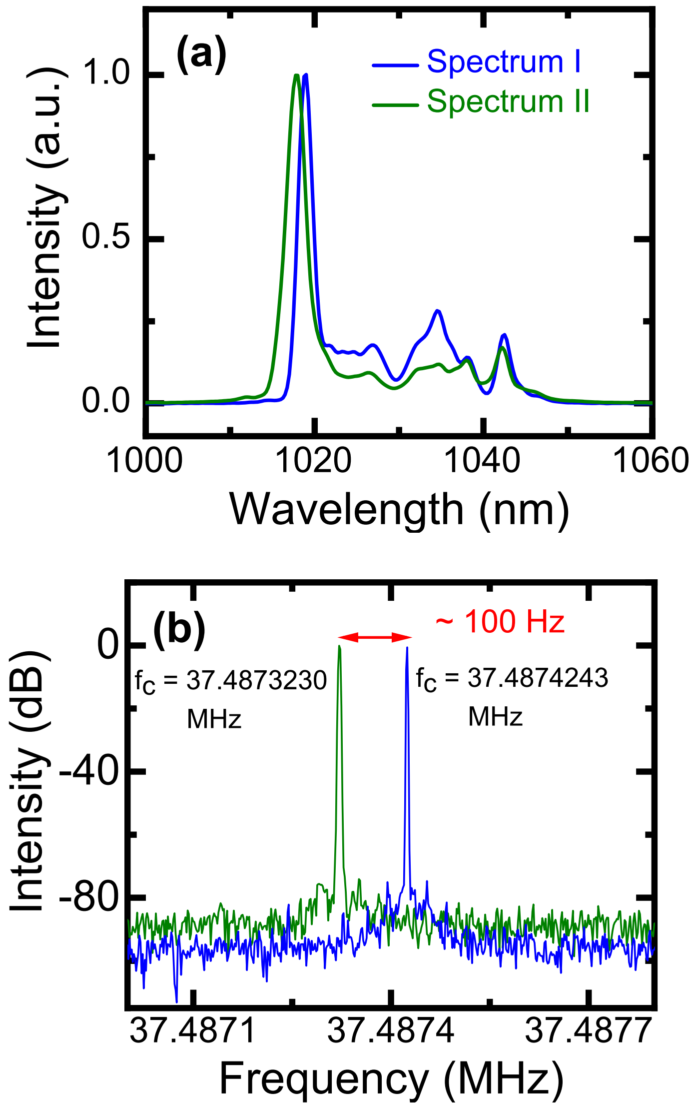

Figure 4.8: Comparison between the two experimental datasets (a) asymmetry comparison between the two mode-locking states. The blue curve (spectrum 1) depicts the spectrum for the mode at 545 mW input pump power while the green curve (spectrum 2) denotes the spectrum for the mode measured at 571 mW. (b) repetition rate comparison between the two spectra.

A short span of 1 kHz and a high resolution bandwidth of 1 Hz are used to record the RF spectra for these two modes and the results are shown in Figure 4.8(b). The repetition rate corresponding to the mode-locked spectrum 1 is higher by $\sim$ 100 Hz than that of spectrum 2. This matches with our theoretical prediction that the higher asymmetric spectrum travels slower which results in the reduced repetition rate of the laser.

4.5 Additional experimental dataset

In this experiment, viability of mode-locking the laser using another double peak spectral response is tested. Again, initially, the laser is operated below the lasing threshold to observe the output of the spectral filter through the 20 % port of the fiber coupler by coupling amplified spontaneous emission (ASE) into the spectral filter. The PC2 and PC3 are carefully tuned so that the output of the spectral filter exhibits a multiple peak structure. This time the BPF is rotated such that it selects a two peak spectral response at central wavelength other than 1030 nm. For example, the sample spectral response shown in Figure 4.9(a) has a dip around 1025 nm and the bandwidth is also different i.e. $\sim$ 7 nm. Once the specific shape of the filter is selected, the pump power is increased and mode-locking is obtained by rotating intracavity waveplates. The output spectrum ejected by PBS is shown in Figure 4.9(b) and the power is $\sim$ 100 mW. The output spectrum at the tap port of the coupler is shown in Figure 4.9(c). The autocorrelation [shown in Figure 4.9(d)] shows that the laser generates sub 150 fs pulses. The RF spectrum in Figure 4.9(e) depicts a good signal to noise ratio. The cross-correlation data in Figure 4.9(f) shows that the pulse has a complex structure.

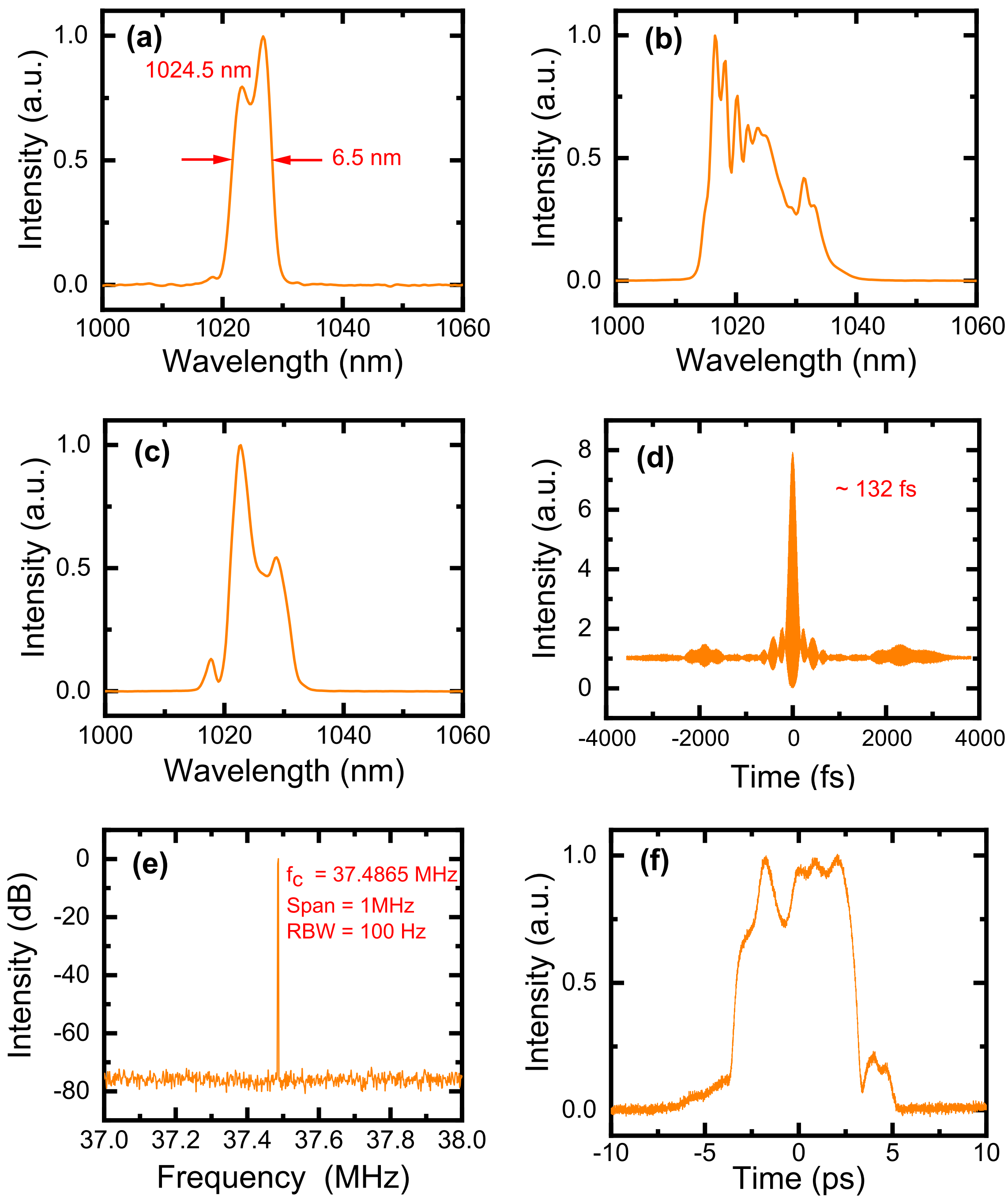

Figure 4.9: Additional experimental dataset (a) spectral filter response (b) output spectrum through PBS (c) spectrum at the tap port (d) autocorrelation (e) cross-correlation.

4.6 Modification to the laser cavity

A beam sampler plate is included in the cavity to observe the spectrum that enters the cavity after being ejected through the PBS. Obviously, after this addition, the cavity is realigned. The modified cavity diagram is shown in Figure 4.10. Now, the shape of the filter is adjusted by repeating the procedure explained in the Section 1.4 and Section 4.5 and this time the dip is adjusted to be around 1030 nm. After increasing the pump power and adjusting waveplates, the laser mode-locks at the pump power of 435 mW . The spectra at the different locations in the cavity are illustrated in Figure 4.11 (a)-(d). It shows that spectrum is truly asymmetric at every location in the cavity. Also, the difference between the spectra transmitted (location C) and rejected (location D) by the NPE port implies that the NPE plays an important role in this laser. The cross-correlation of the pulse is shown in Figure 4.11 (e).

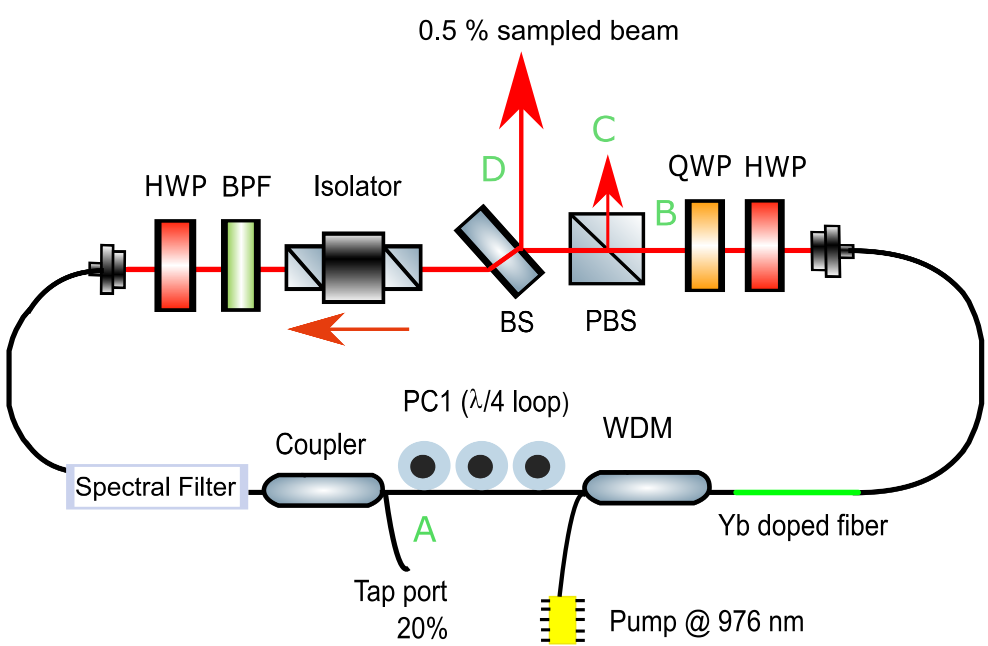

Figure 4.10: Modified laser cavity setup where BS: Beam Sampler

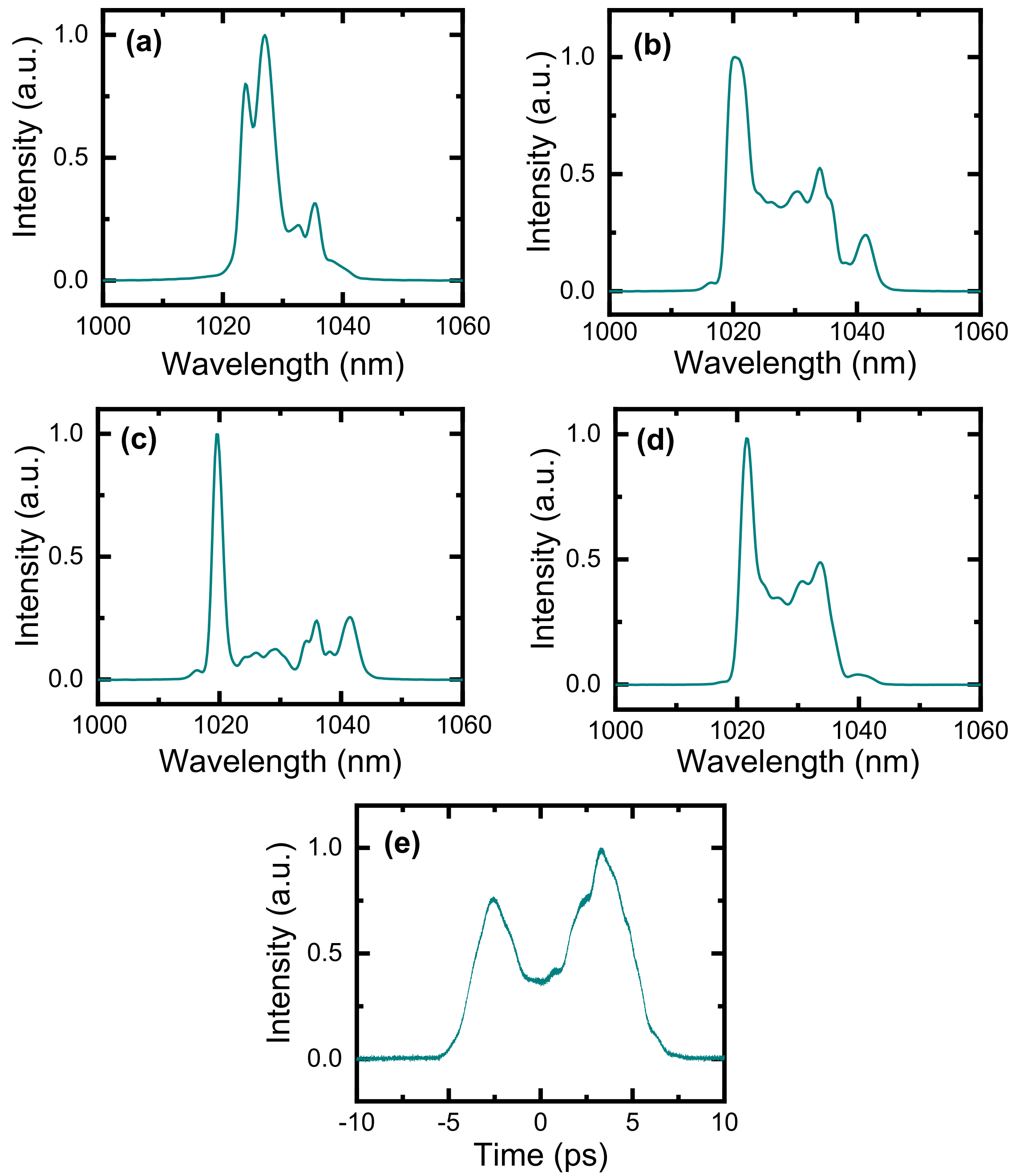

Figure 4.11: Spectra at the indicated locations in the cavity (a) location A: tap port output (b) location B: After SA (c) location C: NPE ejection port (d) location D: sampled beam by the beam sampler (e) cross-correlation for the pulse at location C.

4.7 Discussion

Our simulation and experimental results can be a starting point to explore this pulse shaping mechanism based on the fourth order spectral filtering in the mode-locked fiber lasers. We were successful in realizing dissipative solitons of CSHE fiber lasers with a strong indication of the moving pulse solution of CSHE, characterized by an asymmetric pulse profile with an asymmetric spectrum. In this paper, for the numerical simulations as well as the experiment, we have considered only one spectral filter response, defined by specific values of δ, β, and γ. However, the prospects of finding other solutions of the CSHE in mode-locked fiber lasers using different spectral filter responses are very promising. In the experiments, an all-fiber based spectral filter along with the BPF is perfectly capable of producing a spectral filter transmission not only of the fourth order but also higher orders. Studying the effects of such a higher order spectral filter in mode-locked fiber lasers will be interesting.

It is well known that pulse energy is one of the most important performance parameters of the ultrafast fiber lasers. In our experiments, the pulse energy can reach up to 3 nJ but is limited by the input pump power. We believe that the pulse energy can be improved significantly by realizing the same laser cavity using double clad fibers. It has already proven numerically that CSHE can have high energy solutions at both normal and anomalous dispersion [76]. For the mode-locked lasers at anomalous dispersion, the generated conventional solitons have limited applications due to low pulse energies. Therefore, there is an increasing interest in researching whether high performance dissipative solitons can be experimentally obtained in anomalous dispersion regime [82, 83] and realizing CSHE fiber laser at anomalous dispersion may be a possible way to achieve this goal.

4.8 Conclusion

In conclusion, the first observation of dissipative solitons of CSHE in a passively mode-locked fiber laser is reported here. A dual filter in the form of unique fiber based filter along with a BPF easily produces a fourth order spectral response. The generated pulses have complex asymmetric profiles and the laser spectrum is highly asymmetric with the pulse energy approaching 3 nJ and pulse duration of ~ 100 fs. Much work still remains to optimize the performance of this laser, but these studies found the basis for further investigation of pulse dynamics in mode-locked fiber laser systems with higher order spectral filtering.

CHAPTER V

A WIDELY TUNABLE FIBER LASER USING GRATING COLLIMATOR SPECTRAL FILTER

It is believed that the self-similar/ amplifier similariton (AS) fiber laser design is suitable for wide wavelength tuning. As discussed in Chapter I the self-similar evolution in a laser cavity relies on a very narrow spectral filter bandwidth (BW) and the center wavelength tuning is easily achieved by adjusting this narrow intracavity spectral filter. This chapter demonstrates the most widely tunable AS fiber laser to date.

5.1 Introduction

Wavelength tunable, high-quality mode-locked pulses are essential for various applications such as nonlinear microscopy and telecommunication [84, 85, 86, 87, 88]. Instead of conventional solid-state mode-locked lasers such as a Ti: Sapphire laser, tunable mode-locked fiber lasers which are compact and low cost can be utilized as light sources for tunability demanding applications mentioned above. Yb doped fiber lasers are suitable to generate widely tunable energetic femtosecond pulses since Yb doped fiber has a broad emission spectrum with a capacity to achieve a high output power. In fact, tunable mode-locked Yb doped fiber lasers with a wavelength around 1 μm can be quite useful, especially for medical and biological research [89, 90, 91].

Responding to such demands, tunable Yb doped mode-locked fiber lasers have been investigated in many laser designs. Okhotnikov *et al.* reported a broad range tunable (980–1070 nm) Yb doped fiber laser with a 915 nm pump. However, its performance was quite limited with 1.6 – 2 ps pulse duration and 3 mW average output power across the entire tuning range [92]. The all-normal dispersion (ANDi) fiber laser, which is designed to have strong pulse shaping based on an intracavity spectral filter, can generate femtosecond pulses with high energies. In an ANDi laser, the wavelength tunability can be achieved easily by tuning the intracavity spectral filter. Yang *et al.* reported 6.7 ps and 1.4 nJ pulses from an ANDi laser with a tuning range of 46.3 nm (1024.5 – 1070.8 nm) by tuning a birefringent filter in the cavity [93]. Similarly, Ouyang *et al.* demonstrated a tunable (1032 – 1052 nm) 580 fs and 3 nJ pulse. ANDi laser [94]. Schultz *et al.* also reported a tunable (1015 – 1050 nm) 145 fs with 2.0 nJ pulses from a Yb doped ANDi fiber laser [95].

In 2004, a novel nonlinear pulse evolution, the self-similar evolution, was adapted in fiber lasers [14]. In 2010, many researchers observed the self-similar amplifier pulse in normally dispersive fiber lasers, which are referred to as amplifier similariton fiber lasers [16, 15, 96]. AS lasers demonstrate quite a high performance since self-similar pulses can tolerate substantial nonlinear phase shift to carry higher pulse energies with broad spectral BWs. For example, Nie *et al.* demonstrated a noticeable performance of 10 nJ pulses with 42 fs pulse durations from an AS fiber laser [97]. Since the self-similar evolution in a laser cavity relies on a very narrow spectral filter BW ($\sim$ 4 nm), the center wavelength tuning is easily achieved by adjusting the narrow intracavity spectral filter. Furthermore, high peak power operation with high pulse energies and short pulse durations may be possible from AS fiber lasers. However, to date, the tunability has not been investigated in detail for AS fiber lasers.

In this chapter, the AS fiber laser is investigated to address their potential for the wavelength tunable applications. In this experiment, the central wavelength is tunable from 1030 to 1100 nm. The stable mode-locking is achieved up to 1100 nm with effectively suppressed amplified spontaneous emission (ASE) by heating the gain fiber. The performance of the laser is superior (∼ 120 fs, ∼ 4 nJ) over previous tunable mode-locked fiber lasers owing to the self-similar laser design.

5.2 Experimental Set-up

Figure 5.1 shows a schematic of the fiber laser. After 1.2 m of a single-mode fiber (Nufern: SM-DGF-5/130), a pump combiner (itf Labs: (1 + 1) × 1 Multimode Combiner) couples the 976 nm pump into a 3 m Yb doped double cladding gain fiber (Nufern: SM-YDF-5/130-VIII) which is followed by another 0.9 m SMF. The total fiber length is 5.1 m and total cavity dispersion is 0.11 ps^2. Two quarter waveplates (QWP), a half waveplate (HWP), and a polarizing beam splitter (PBS) serve as an artificial saturable absorber for

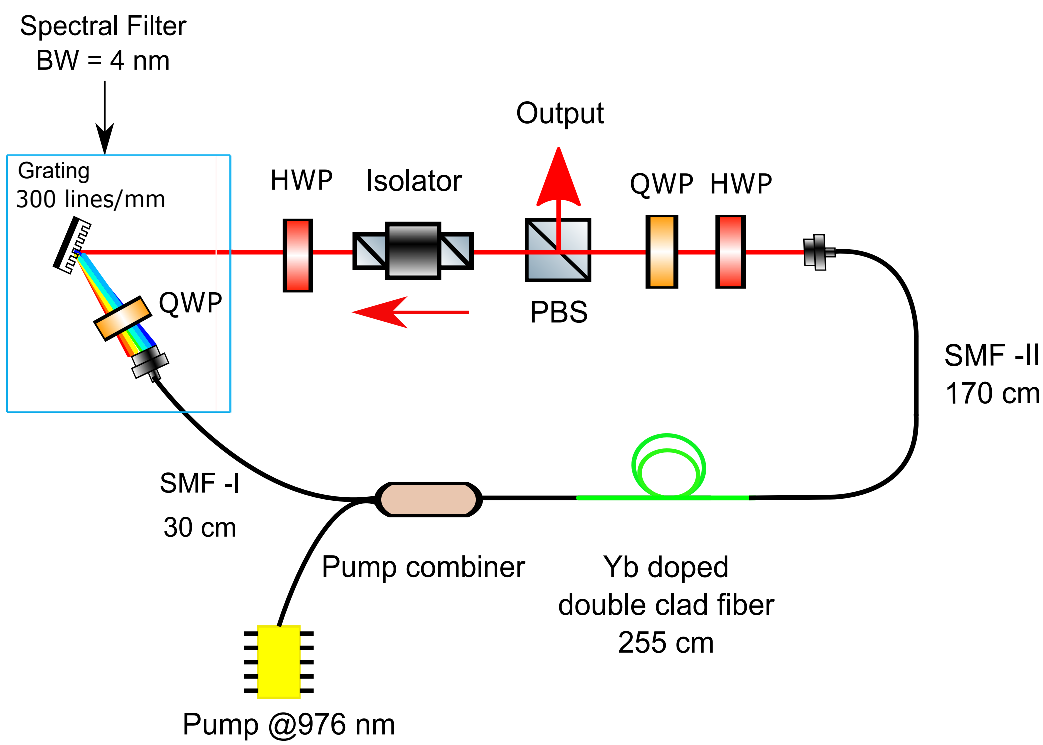

Figure 5.1: Schematic of the tunable fiber oscillator. PBS, polarizing beam splitter; HWP, half waveplate; QWP, quarter waveplate; SMF, single mode fiber.

passive mode-locking by manipulating the nonlinear polarization evolution (NPE) in the fiber. The HWP after the isolator adjusts the polarization to maximize the diffraction efficiency of the diffraction grating. A 600 lines/mm grating with a collimator serves as a 4 nm BW Gaussian spectral filter which is crucial to initiate the self- similar pulse evolution [98]. Self starting mode-locking is achieved by randomly rotating intracavity waveplates. By adjusting the diffraction grating incident angle, the center wavelength of the spectral filter is conveniently tuned. As the laser wavelength is shifted away from the maximum gain around $\sim$ 1040 nm of the Yb doped fiber, the emission cross section of the gain significantly decreases. This results in a strong gain competition between the signal and the ASE around 1040 nm. The competition may result in an undesirable parasitic lasing around 1040 nm as well. To avoid the ASE, in situ heating is provided to the gain. Researchers have demonstrated that heating Yb doped fiber changes the population of Yb sub - levels that leads to a growth of absorption cross section around 1040 nm. This increases the reabsorption effect at the shorter wavelength to assist the lasing at the longer wavelength [99, 100, 101, 102]. This method gives us a feasible way to obtain a stable mode-locking at an extreme wavelength.

5.3 Experimental Results

In our experiment, a heating platform (Corning PC 620 Hot Plate Stirrer) is used to heat the gain fiber to suppress the ASE. The gain fiber is coiled orderly on the heating platform and covered by aluminum foil, which ensures heating uniformity. It is observed that when the mode-locked operation shifts to 1100 nm, the ASE emerges and has a strong competition with the mode-locked operation [Figure 5.2(a)], which makes the spectrum unstable. The ASE starts decreasing when the temperature of the gain fiber is increased,

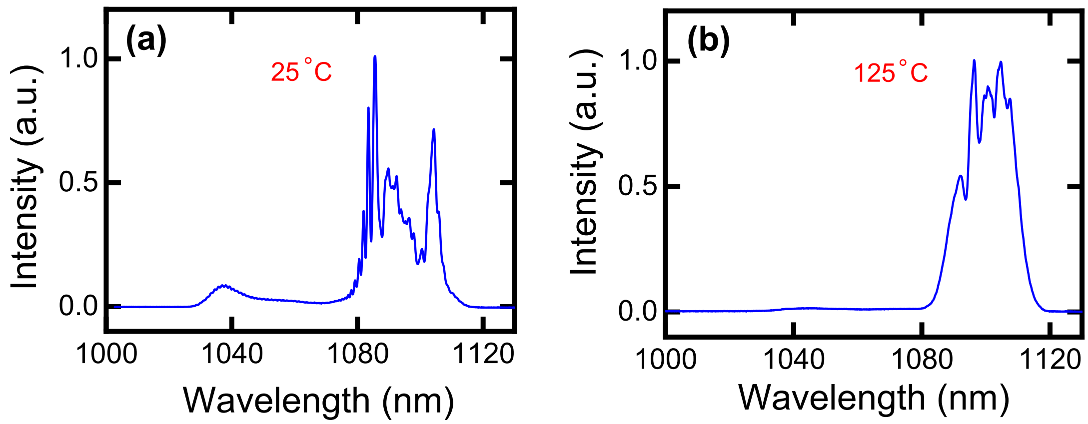

Figure 5.2: Effect of temperature on a) mode-locked spectrum at 1100 nm without heating the gain fiber (b) mode-locked spectrum at 1100 nm with heating up the gain fiber to 125° C.

and it is noticeably reduced when the heating platform reaches the temperature of 125°C [Figure 5.2(b)].

By adjusting the grating orientation, it is possible to shift the wavelength from 1030 to 1100 nm without losing mode-locking [Figure 5.3(a)]. The spectrum shape is maintained over the whole span which shows that similar pulses can be produced, regardless of the center wavelength. After a pair of gratings to dechirp pulses, interferometric autocorrelations (ACs) are measured [Figure 5.3(b)]. Figure 5.3(c) shows the pulse duration and the spectral BW, as the center wavelength is tuned. The full width at half-maximum of the spectral BW and the dechirped pulse durations range from 14 to 21 nm and 116 to 131 fs, respectively. The shortest dechirped pulse duration (116 fs) is generated at the center wavelength of 1070 nm. Figure 5.3(d) shows the pulse energy variation over the center wavelength of the laser. The highest pulse energy (3.9 nJ) is obtained at the center wavelength of 1060 nm with a 33.7 MHz repetition rate and 131 mW average power.

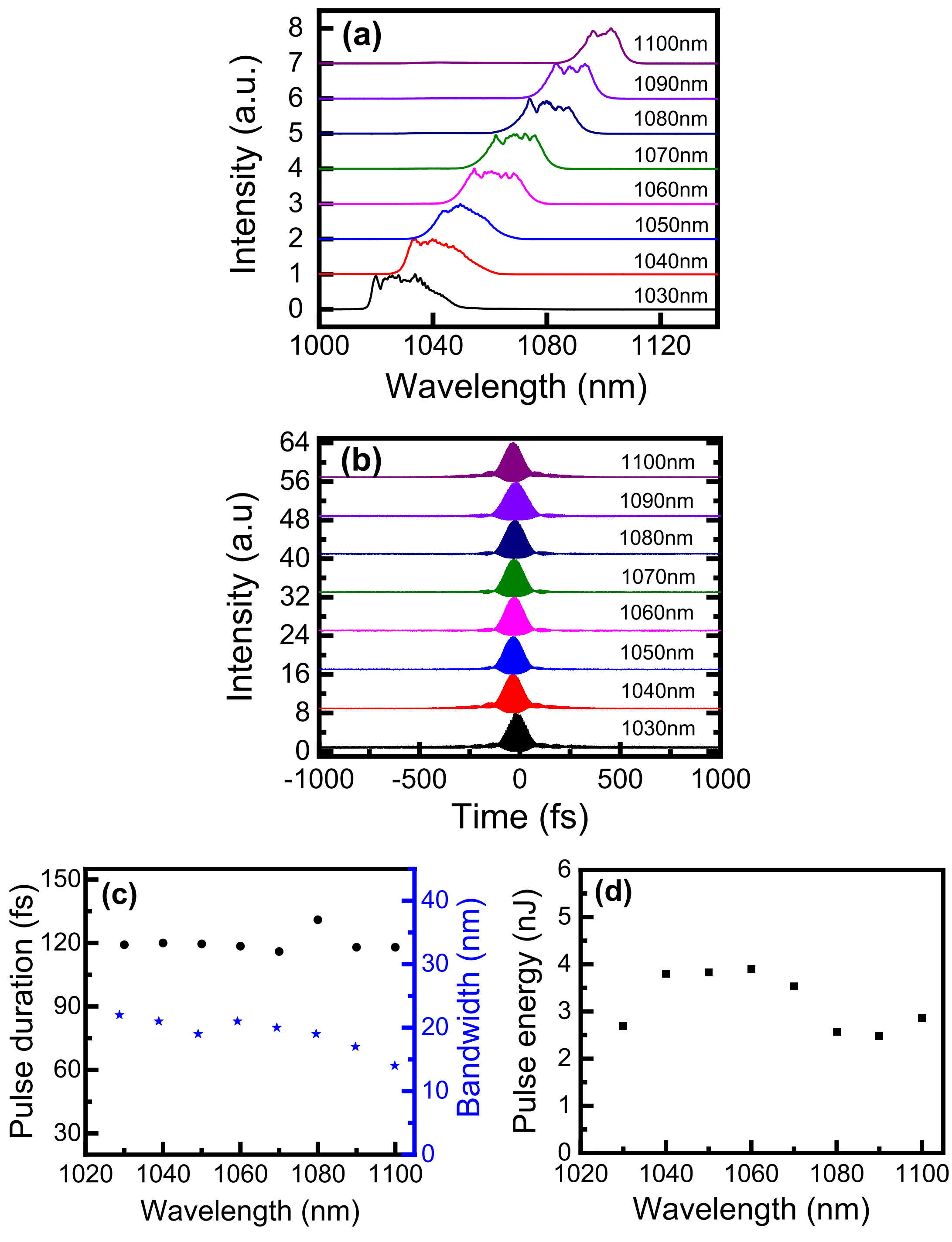

Figure 5.3: Experimental dataset 1 (a) tuned mode-locked spectra (b) AC (c) the pulse duration and BW versus the laser center wavelength (d) the pulse energy versus the laser center wavelength.

By adjusting wave plates to control the NPE, sub-100 fs pulses with a broad tuning range ($\sim$ 70 nm) can also be achieved (Figure 5.4). The production of sub-100 fs center wavelength tunable pulses, which have not been demonstrated by other fiber laser designs, are possible by the self-similar pulse evolution. Tuning is again easily achieved by adjusting the diffraction grating without losing mode-locking [Figure 5.4(a)]. Figure 5.4(b) shows AC results corresponding to various central wavelengths. Spectral BWs and pulse widths range from 30 to 45 nm and 81 to 95 fs [Figure 5.4(c)], respectively. The shortest pulse (81 fs) is at 1040 nm. Figure 5.4(d) shows the pulse energy versus the center wavelength with the highest pulse energy of 2.02 nJ at 1040 nm. As the pulse duration decreases, the output pulse energy also decreases, unfortunately. The laser stability is not checked systematically over a long period of time, but no degradation in the performance was observed within 24 h of operation.

5.4 Discussion and conclusion

As a future work, the tuning range can be extended far below 1030 nm by using a 915 nm pump [92]. In this experiment, a free-space section is there, which can be environmentally sensitive, in the fiber cavity. Implementing an all-fiber NPE saturable absorber and a fiberized spectral filter will eliminate the free space-propagation in the fiber cavity and improve its environmental stability. In summary, an investigation of a tunable Yb doped AS mode-locked fiber laser is reported. The center wavelength is tuned without losing mode-locking by adjusting a narrow intracavity spectral filter. Highly performing pulses with pulse durations around 118 fs and pulse energies of 3.9 nJ are demonstrated over a 70 nm tuning range. The results reveal that AS fiber lasers have a strong potential for applications requiring wavelength tunable pulses.

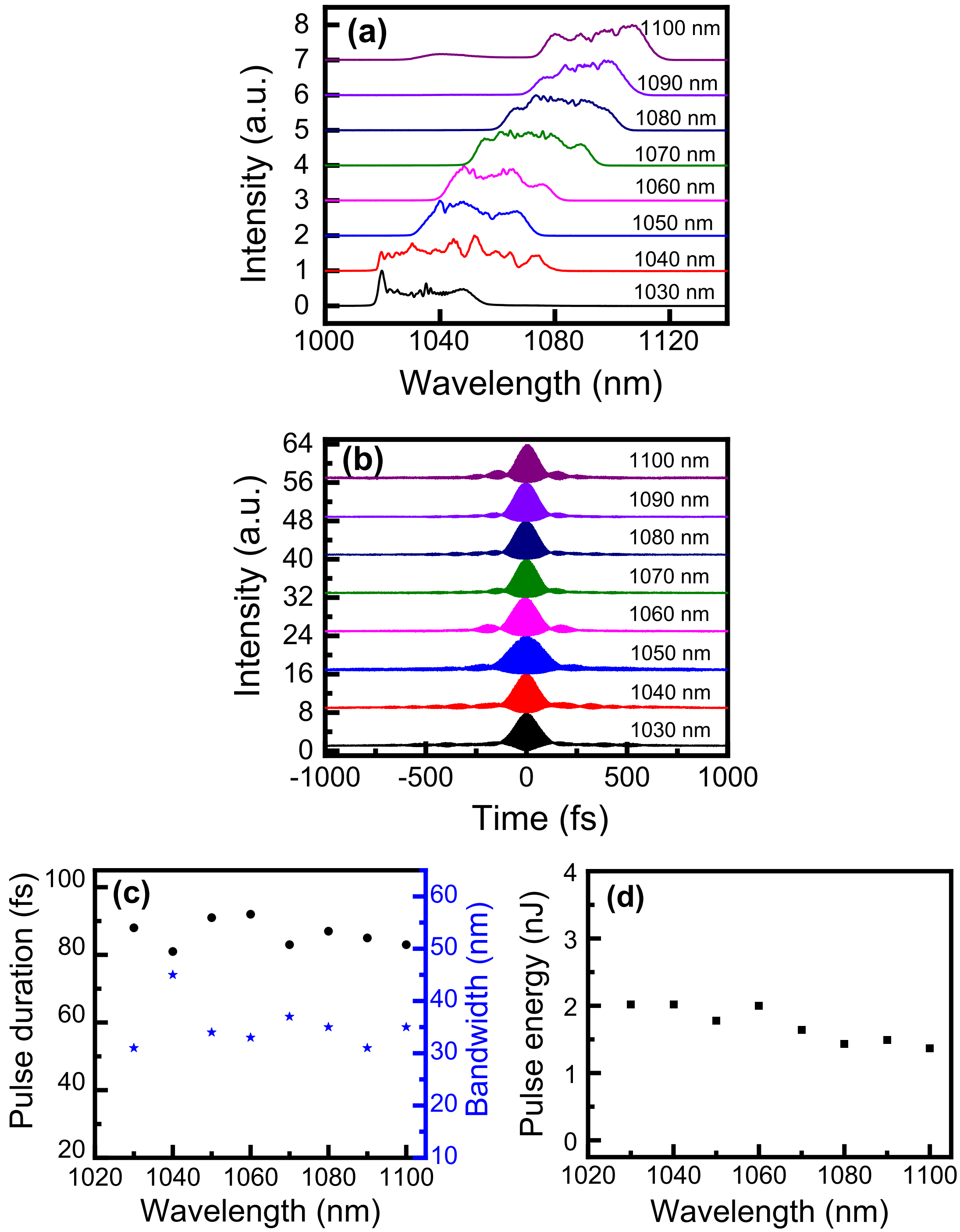

Figure 5.4: Experimental dataset 2 (a) tuned mode-locked spectra (b) AC (c) the pulse duration and BW versus the laser center wavelength (d) the pulse energy versus the laser center wavelength.

CHAPTER VI

FEW CYCLE PULSE GENERATION FROM A FIBER OSCILLATORS WITH A VERY NARROW INTRACAVITY SPECTRAL FILTER

In this chapter, a mode-locked fiber laser with a strong self-similar evolution in a gain segment and spectral broadening in a photonic crystal fiber is simulated to generate nearly octave spanning spectra. Difficulties to realize this design experimentally leads to modification in the design and this modified design generates a dramatic intracavity spectral broadening experimentally. All these efforts are summarized in this chapter.

6.1 Introduction

Optical pulses of temporal durations reaching few cycles or a single cycle of the carrier frequency with spectra broader than an octave spanning have been essential for a variety of cutting-edge applications such as attosecond science [103, 104], high-harmonic generation [105], and coherent X-ray generation [106]. Currently, solid-state lasers have been at the forefront of few-cycle pulse generation owing to their broad gain bandwidths (BWs) [107, 108, 109]. Even though the performance of fiber lasers has been comparable to solid-state lasers in terms of pulse energies and peak powers, generating few-cycle or single-cycle pulses is still challenging for fiber lasers because of their limited gain BW.

One general method to obtain few-cycle pulses from fiber lasers is using nonlinear pulse compression outside the cavity [110, 111, 112]. Another attractive method to generate a single-cycle pulse from a fiber device is by coherently combining two supercontinuum spectra from highly nonlinear photonic crystal fibers (PCF) [113]. However, these devices are extremely complex with stability issues. On the other hand, ultrashort pulses with broad spectra generated directly from mode-locked fiber lasers have advantages. Pulses generated directly from a laser are more stable with less noise since the temporal phase on a pulse is reshaped for each round trip. Furthermore, pulses can be conveniently compressed externally for even shorter pulse durations. Therefore, it is strongly desirable to generate broad spectra beyond the gain BW from a simple fiber oscillator.

In order to generate a broad spectrum directly from a fiber oscillator, a proper fiber laser design is crucial to permit a substantial intracavity spectral broadening without losing the mode-locked operation. It turns out that a recently discovered self-similar fiber laser operation [15, 16, 96] facilitates such a broad mode-locked spectrum. Self-similar pulses are linearly chirped parabolic pulses as asymptotic solutions of a normal group velocity dispersion (GVD) fiber amplifier [13]. Remarkably, a self-similar pulse is a strong nonlinear attractor of the gain fiber. Even though a strong perturbation such as a substantial accumulation of nonlinear phase is introduced, the perturbed pulse conveniently returns to a self-similar parabolic pulse by strong filtering followed by a normal GVD fiber amplifier [114]. As a consequence, an enormous intracavity spectral broadening can be stabilized as a mode-locked operation by strong spectral filtering and self-similar amplification. By inserting a highly nonlinear PCF after the self-similar pulse is established in the gain fiber (Figure 6.1), very broad spectrum ($\sim$ 200 nm BW), which is much larger than the gain BW, has been demonstrated [115]. Pulses from the laser are highly chirped but could be dechirped externally to $\sim$ 20 fs. Since then, there has not been much improvement in the pulse duration from fiber lasers.

In [115], a chirped parabolic pulse was coupled into PCF; therefore, the broadened spectral BW was limited. Recently performed simulations proved that a huge spectral broadening can occur by dechirping these chirped parabolic pulses before they enter PCF with the help of an intracavity dispersion delay line (DDL) [5]. These simulations yielded

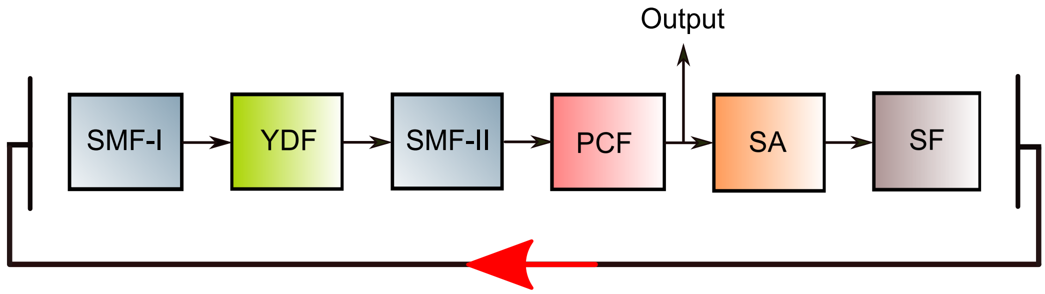

Figure 6.1: Conceptual schematic of the laser in [115]. SMF, single mode fiber; YDF, ytterbium doped fiber; PCF, photonic crystal fiber; SA, saturable absorber; SF, spectral filter.

broad spectra only when an ideal saturable absorber with ∼100 % modulation depth is used and those results are included in this chapter. However, such broad spectra have not been observed in experiments. One conjecture for this discrepancy is the nonideal saturable absorber in lasers. The subsequent experiments and numerical studies suggested that the saturable absorber in fiber lasers must be improved to stabilize substantial spectral broadening. Then, the design is modified using a unique fiber laser cavity called Mamyshev oscillator [19]. A Mamyshev oscillator exhibits a transmission Vs intensity curve that jumps from zero to maximum like a step function at a certain intensity, which is referred to as a perfect saturable absorber [116]. This oscillator has successfully demonstrated its potential for high pulse energies (50 nJ) and short pulse (40 fs) durations [19]. Lately, the same oscillator with a large-core PCF design has achieved a remarkable performance of 1 μJ pulse energy and 40 fs pulse duration [117]. Owing to its unique 'perfect' saturable absorbing action, the Mamyshev oscillator appears to be a good candidate to stabilize a massive intracavity spectrum broadening. Hence, in further experiments modified Mamyshev oscillator is used to generate a very broad mode-locked spectra (∼ 400 nm at - 20 dB) with 5-cycle pulse duration (17 fs) and the results are demonstrated.

6.2 Numerical model of a self-similar oscillator with a PCF and results

Numerical simulations are performed using standard split step Fourier method including Kerr nonlinearity, Raman effect and dispersion to assess the feasibility of the mode-locked design. The simulated laser cavity is based on the design explained in [115] with the addition of DDL shown in Figure 6.2.

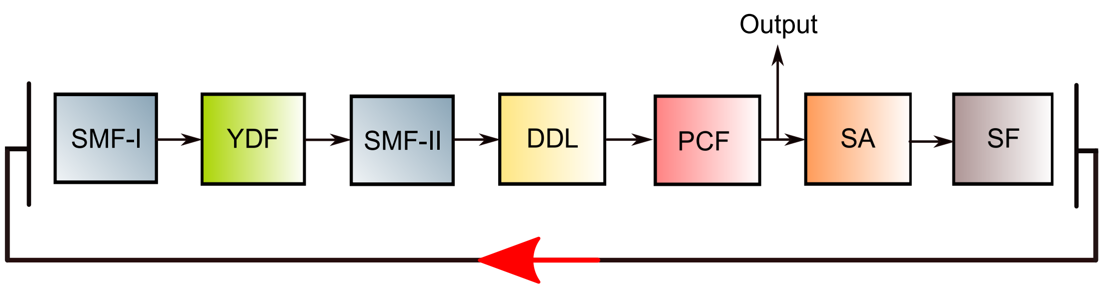

Figure 6.2: Conceptual schematic of the self-similar laser. SMF, single mode fiber; YDF, ytterbium doped fiber; DDL, dispersion delay line; PCF, photonic crystal fiber; SA, saturable absorber; SF, spectral filter.

The main purpose of introducing DDL before PCF is to send higher peak power, dechirped pulses to PCF so that a very broad spectrum can be obtained after the PCF. It is observed that simulation is unable to converge when the chirp is removed completely from pulses by using a grating pair; excessive perturbation being the main reason. The best performance is achieved when a pulse containing a small linear chirp enters the PCF. The other simulation parameters are listed in Table 6.1. The calculation related to nonlinearity coefficient γ and group velocity dispersion coefficient β_2 is explained in Appendix A.

Table 6.1: Parameters used for the numerical simulation

Parameter	Value
L_{SMF-I}	25 cm
L_{YDF-I}	255 cm
L_{SMF-II}	170 cm
Spectral filter BW	3 nm
$\beta_{2\ SMF} = \beta_{2\ YDF}$	230 fs^2/cm
$\beta_{2\ PCF}$	63.39 fs^2/cm
γ_{SMF}	0.000047 $\mathrm{W}^{-1}cm^{-1}$
γ_{PCF}	0.000405 $\mathrm{W}^{-1}cm^{-1}$
g_0	30 dB
E_{sat}	1.6 nJ
OC	0.6

The simulation produces octave spanning spectra [shown in Figure 6.3(a)] extending from 750 nm to 1600 nm (660 nm at -20 dB level). To our best knowledge, this is the first numerical evidence demonstrating the generation of very broad spectra directly out of a mode-locked fiber laser. The pulse has a linear chirp with 0.9 nJ of pulse energy [Figure 6.3(b)]. The pulse duration continues to grow inside the gain fiber as the pulse experiences the self-similar evolution as a strong local nonlinear attractor. The grating pair quickly cuts down the pulse duration before it enters the PCF. The pulse duration increases again inside the PCF, but a strong spectral filter ensures the self-consistency and stability of the mode lock operation [Figure 6.3(c)].

6.3 Experimental results of a self-similar oscillator with a PCF

The experimental laser cavity is roughly based on [97] and is shown in Figure 6.4. It should be noted that it is important to establish a powerful and efficient self-similar attractor in the gain fiber before introducing perturbations like DDL and PCF into the cavity. The

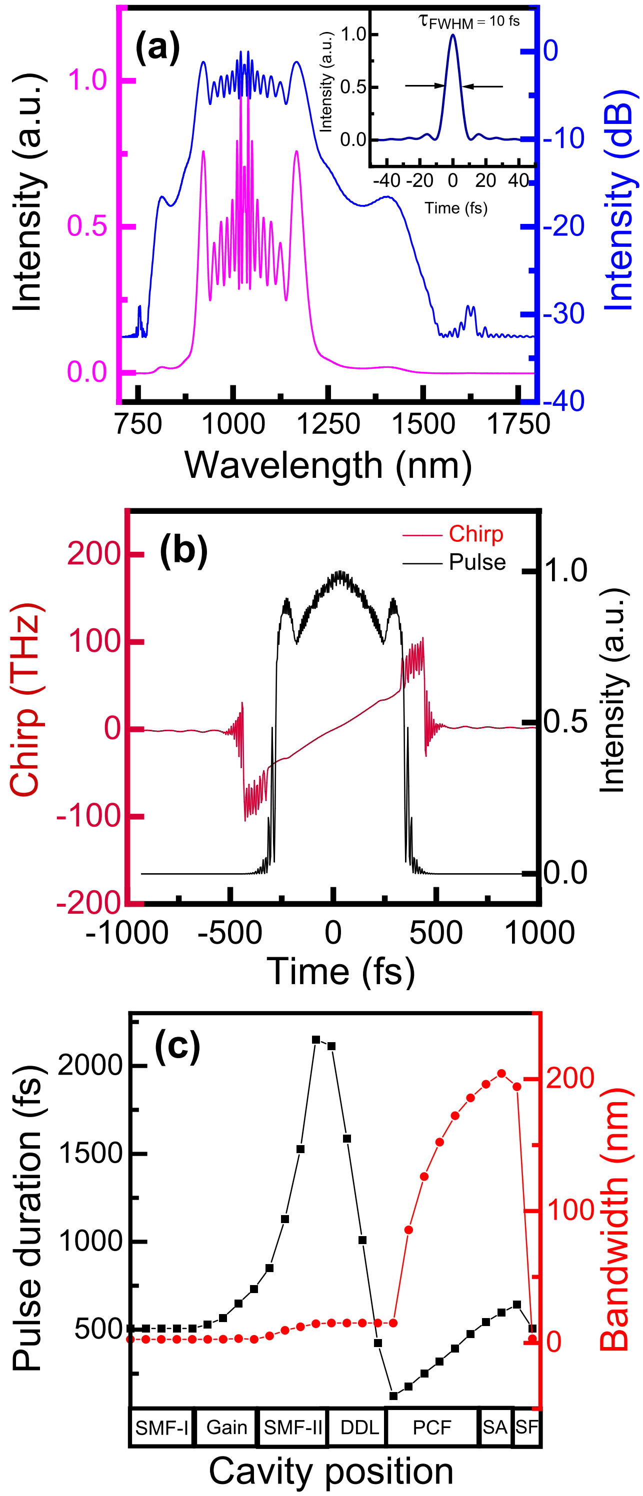

Figure 6.3: Simulation results a) octave spanning spectra. Inset shows the transform limited pulse duration b) Output pulse and corresponding chirp c) Evolution of pulse duration and spectral bandwidth through laser cavity. The spectral breathing ratio can be as large as $\sim$ 86.

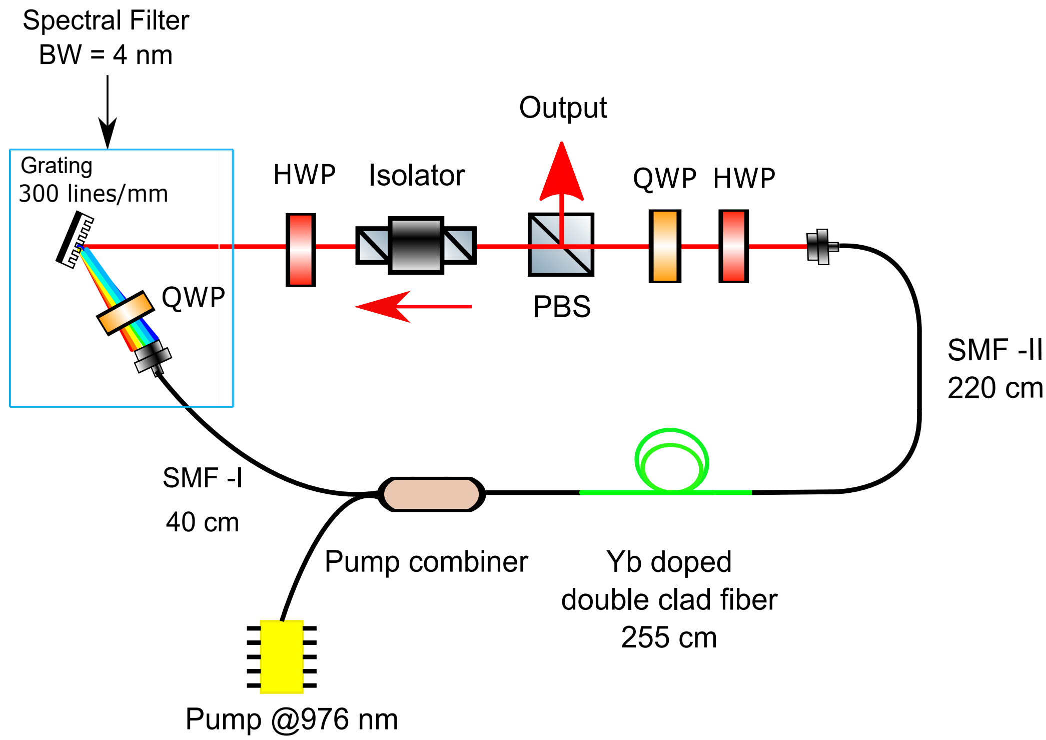

Figure 6.4: Experimental DC laser cavity. SMF, single mode fiber; HWP, half waveplate; QWP, quarter waveplate; PBS, polarizing beam splitter.

expected performance of this cavity is $\sim$ 900 mW of average output power (when pumped with $\sim$ 4 W), with approximately $\sim$ 10 nJ pulse energy after de-chirping pulses to 42 fs according to [97]. Unfortunately, this performance is not achieved with the cavity shown in Figure 6.4. The possible reasons are - the bad cleaving of the gain fiber resulting in a bad splice between the gain fiber and the pump combiner and another poor splice between gain fiber and SMF-II, using SMF28 as single mode fibers in the cavity which has operational wavelength of 1550 nm, and the handmade collimators which do not offer the quality of the commercial collimators. When pumped with 3 W, the laser emits 10 nJ pulses before de-chirping (330 mW of average output pulse power and with $\sim$ 35 MHz of repetition rate). The pulse duration is reduced to 83 fs after de-chirping with a grating pair and energy

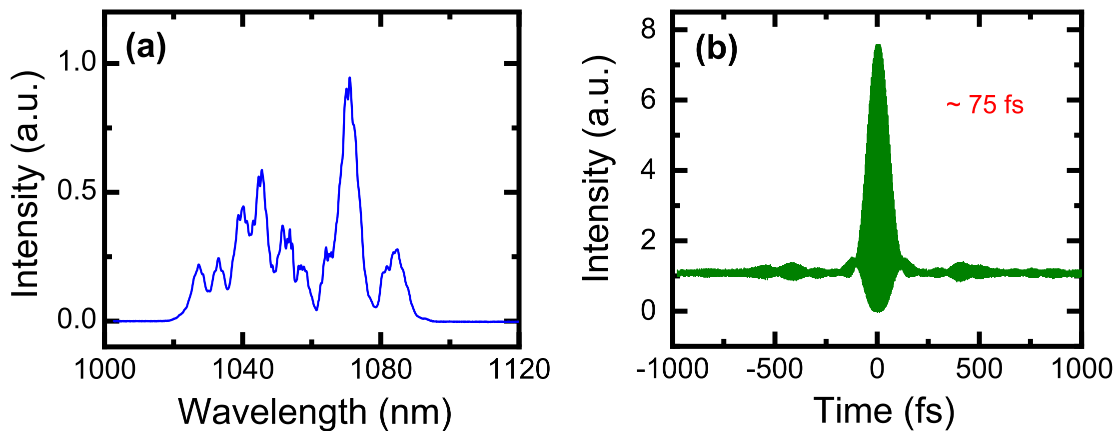

Figure 6.5: Experimental DC laser cavity results (a) output spectrum (b) autocorrelation.

is reduced to $\sim$ 7 nJ. The output spectrum and autocorrelation are shown in Figure 6.5(a) and Figure 6.5(b), respectively. The fringe pattern in the output spectrum is indicative of multimode nature of the fibers used in the cavity. One might suggest to increase the input pump power in order to increase the output power but that points to a highly inefficient laser cavity and eventually doing so, the optical components such as collimators are damaged. An efficient cavity and a high intracavity power is extremely crucial for putting high intensity pulses in the PCF and therefore, other laser designs are considered.

6.4 Experimental results of Mamyshev oscillator with an intracavity PCF

An alternative for the generation of few cycle pulses can be based on the Mamyshev oscillator, the basic principle of which has been explained in Chapter I. The basic cavity design is followed from [19], but the entire cavity is built in non polarization maintaining (non-PM) fiber format to use nonlinear polarization evolution (NPE) based saturable absorber to avoid the use of an external seed. The experimental set up of the Mamyshev oscillator is schematically illustrated in Figure 6.6. It consists of two fiber arms. In each arm, a pump combiner couples the 976 nm pump into the 3.1 m Yb-doped double cladding (DC) gain fiber, which is followed by a 0.7 m SMF. The total fiber length is 9 m which corresponds to the total cavity dispersion of 0.146 ps^2. Two free space isolators ensure a unidirectional laser operation. Two 600 lines/mm gratings with collimators serve as narrow 4 nm BW Gaussian spectral filters centered at $\sim$ 1040 nm and $\sim$ 1050 nm wavelength while the center wavelength of the laser is at 1045 nm. Two HWPs after isolators adjust the polarization to maximize the diffraction efficiency of the diffraction grating. In the second arm, more components are inserted to enhance the intracavity spectral BW. After the second arm, a DDL of a 1000 lines/mm grating pair is inserted to compress the pulse. The compressed pulse is coupled into a 45 cm of all normal dispersion (ANDi) PCF with a 50 % coupling efficiency. Two QWPs, a HWP and a PBS serve as a NPE based artificial saturable absorber to start mode-locking.

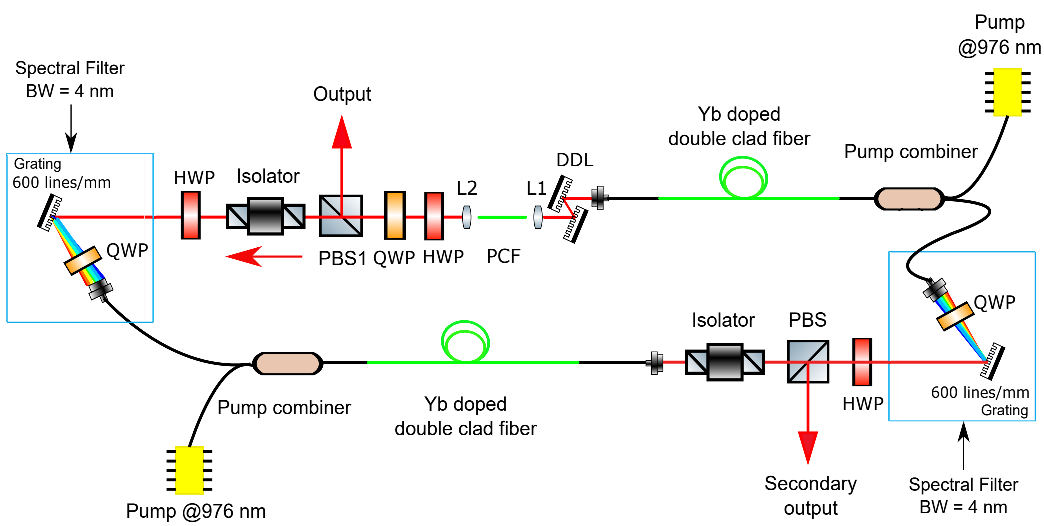

Figure 6.6: Experimental laser cavity. HWP, half waveplate; QWP, quarter waveplate; PBS, polarizing beam splitter; DDL, dispersion delay line; PCF, photonic crystal fiber; L1, focusing lens; L2, collimating lens.

Experiment results are shown in Figure 6.7. Figure 6.7(a) shows the output spectrum at the PBS2, which is the enhanced spectrum after the PCF, with 394 nm BW at -20dB. The output pulse energy is 3.5 nJ at 17.5 MHz repetition rate. The autocorrelation (Figure 6.7(b)) shows 17 fs (5 cycles) pulse duration after dechirped by a 300 /mm grating pair. In the autocorrelation signal, noticeable pedestals are observed due to uncompensated higher order dispersions. It is believed that Fourier transform limited pulses ($\sim$ 9 fs, Figure 6.7(c)) can be obtained with a better phase compensation technique such as a multiphoton intra-pulse interference phase scans (MIIPS). The detailed experimental and simulation results can be found in [118].

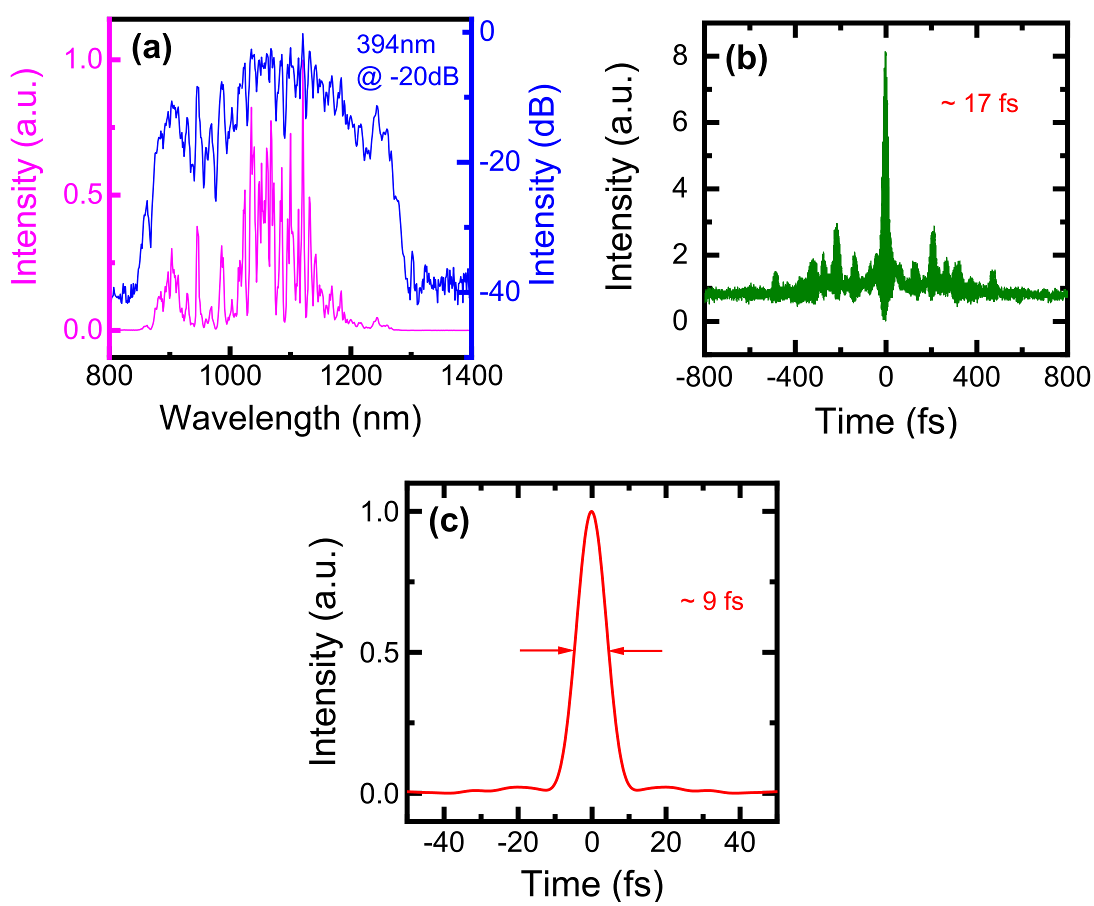

Figure 6.7: Experimental results a) Output spectrum b)Dechirped autocorrelation c) Calculated Fourier transform limited pulse profile.

6.5 Conclusion

In conclusion, ultrabroadband, few-cycle pulses directly from a Mamyshev fiber oscillator are demonstrated. The extreme spectral broadening in the cavity can be stabilized by the self- similar evolution and the perfect saturable absorber action of the Mamyshev oscillator. To the best of our knowledge, this is the broadest spectrum and shortest pulse (17 fs) directly generated from a mode-locked fiber laser.

CHAPTER VII

VISIBLE FIBER LASER

This chapter discusses numerical as well as experimental methods to generate ultrafast pulses directly at visible wavelengths.

7.1 Introduction

Visible lasers are attractive for many applications such as laser display technology [119, 120, 121], medical applications especially ophthalmology [122], material processing [123], confocal laser scanning microscopy [124], metrology [104] and Raman spectroscopy [125]. A brief overview of visible laser systems is given here and they can be classified into the three categories: gas, liquid, and solid. The most common visible gas lasers are the Ar, Kr ion lasers [126], excimer lasers [127], HeNe lasers [128] and metal vapor lasers [129, 130]. These lasers are good for scientific purposes, but they are huge, complicated systems and their power efficiency is very low. Dye lasers are the only commercially available liquid laser, have been an important system for the visible light generation with a widely tunable range, between 300 and 1100 nm [131], either in CW mode or ultra-short high energy pulse mode [132]. However, dye lasers have multiple significant disadvantages such as rapid degradation of dyes during operation, limited output power, and the need for expensive pump sources e.g. with green or blue light. Moreover, dye lasers require the handling of poisonous, often even carcinogenic materials. Therefore, solid state lasers, which are much more stable and convenient to handle over gas and liquid lasers, have been considerably preferred. In order to realize visible solid-state lasers, the following methods have been used.

- Nonlinear frequency conversion techniques such as second/third harmonic generation/sum frequency generation/optical parametric generation using pulses from IR mode-locked lasers e.g. frequency doubling of Nd:YAG or Yb doped fiber lasers to generate green light

- Upconversion lasers e.g. Praseodymium (Pr), Neodymium (Nd), Holmium (Ho), Erbium (Er) and Thulium (Tm) doped crystals/fibers can be used to generate visible wavelengths

- Semiconductor lasers e.g. InGaP, GaN laser diodes

Even though ultrashort visible pulses are useful in many applications like UV light generation, nonlinear microscopy, cancer research, mode-locked soild state ultrashort lasers at visible wavelengths are extremely rate. A Pr doped Yttrium Lithium Fluoride (Pr: YLF) solid state laser successfully generated ultrashort pulses at 613 nm [133]. But the pulses had a limited pulse duration of 400 fs and the average power was $\sim$ 50 mW. A diamond Raman laser was successfully generated yellow pulses at 573 nm [134]. However, it emitted ps pulses ($\sim$ 10 ps). Therefore, even today, visible ultrashort pulses are mainly generated by the nonlinear frequency conversion of pulses from near IR lasers such as Ti: Sapphire lasers.

Researchers desire an alternative ultrafast visible laser solution that is compact, low cost, user friendly and maintenance free compared to solid state lasers. A passively mode-locked fiber laser can satisfy all these demands, and therefore, there is strong research motivation to develop passively mode-locked fiber lasers in the visible region.

Despite the fact that the fiber lasers offer enormous advantages over solid state lasers, mode-locked femtosecond fiber lasers directly emitting visible radiation are not available readily. There are several reasons for that which are listed here.

- Visible rare earth (Pr, Nd, Ho, Er and Tm) doped fiber lasers, which are based on upconversion pumping scheme, are not efficient enough for stable passively mode-locked operation [31]
- For rare-earth doped fibers, gain bandwidths (BW) at many visible lasing wavelengths are not wide enough to support femtosecond pulses
- The huge normal dispersion of the fiber cavity at visible wavelengths greatly increases the difficulty of passive mode- locking
- Technological challenges such as fabrication of low loss fiber at visible wavelength, lack of high pump power diodes, visible wavelength fiber components such as WDM, couplers etc.

Due to the rapid development of low loss soft glass fibers and high power blue laser diodes recent years, rare earth doped ZBLAN fibres can provide high-performance optical gain at visible wavelengths [135]. Mode-locking techniques of normal dispersion fiber lasers have been advanced as well. Today, normal dispersion fiber lasers are demonstrated for their high performance [18]. It is already shown that a narrow gain BW is not an obstacle for mode-locking a laser as described in earlier chapters [115, 118] Based on recent technical advances, it is believed that the chance of realizing visible mode-locked fs fiber lasers is better than ever.

7.2 Pr doped visible fiber lasers

Praseodymium (Pr^{3+}) doped fiber is the main rear earth element that is considered in this dissertation as a gain medium. The energy level diagram of Pr^{3+} is shown in Figure 7.1.The $^3P_0$ level is a metastable state, and its lifetime is approximately several tens of ms and varies based on the host material. This state decays to the lower energy levels based on their lifetimes with visible emissions that correspond to energy gaps between excited states. There are five main emission lines: $^3P_0$ - $^3H_4$ (482 nm), $^3P_1$-$^3H_5$ (523 nm), $^3P_0$ - $^3H_6$ (605 nm), $^3P_0$ - $^3F_2$ (637 nm),and $^3P_0$ - $^3F_4$ (719 nm).

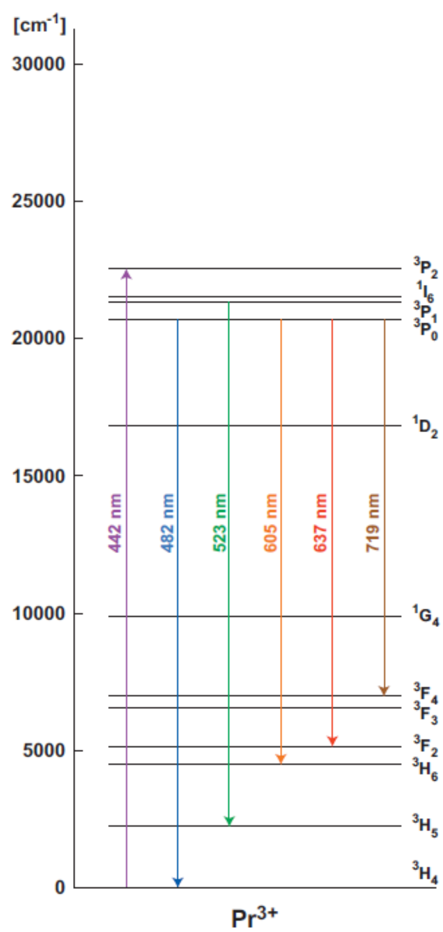

Figure 7.1: Energy level diagram of Pr^{3+}.

The rare earth elements have many energy levels and some combinations of emissive rare earth elements and host materials relax the populations at the metastable state through a multiphonon relaxation process. Since the possibility of a multiphonon relaxation process is related to the maximum phonon energy in the host material and oxide materials have relatively high phonon energy, emissive rare earth elements in oxide hosts are limited. Fluoride glasses have lower phonon energy than oxide glasses and hence they are preferred as host materials. The important discovery of a fluoride glass material was ZBLAN glass by Poulain *et al.* [136]. The ZBLAN glass system became the most common fluoride glass system. But fluoride glasses are hygroscopic hence some researchers developed aluminum fluoride (AlF_3) glass system, which is waterproof. Moreover, the high power (> 1W) blue GaN laser diode at 440 nm significantly improved the development of Pr doped visible fiber laser.

Some of the noticeable efforts in the field of visible fiber lasers are listed here. In 2009, CW tunable operation of Pr doped ZBLAN fiber laser was shown [137]. In the same year, a Pr doped waterproof fluoride glass (WPFG) fiber laser was demonstrated at four main Pr^{3+} emission wavelengths [135]. The next year, the power of this Pr: WPFG fiber laser went up 311.4 mW at 638 nm [138], and then in 2011, 645.7 mW at 638 nm [139] and 598 mW at 522.2 nm [140]. In 2012, 0.95 W (532 nm) and 1.2 W (638 nm) CW output powers were achieved from the same laser [141, 142]. It is important to know that the output power scaling was obtained by using multiple pump diodes and employing a large core (multimode) Pr: WPFG fiber. The same research group demonstrated a CW operation at 638 nm in double clad (DC) WPFG fiber as DC technology is the key for further scaling of power and it also eases free space coupling of the pump light from GaN diodes [143]. This laser could not demonstrate a watt level power but the laser output was strictly single mode. A saturable absorber (SESAM) was employed in DC WPFG fiber soon which resulted in ns pulses [144].

In the case of pulsed Pr:ZBLAN fiber lasers Wu *et al.* generated ns pulses with different types of 2D saturable absorbers [145]. All of their mode-locking efforts resulted into Q-switching eventually [146, 147]. At visible wavelengths, a fiber is highly normally dispersive. The group velocity dispersion (GVD) coefficient at the visible wavelength (500-600 nm) is estimated to be 60-80 fs$^2/mm$ (Refer to Appendix B) which is four times larger than the GVD at near IR wavelengths. The mode-locking will be very difficult for such high normal GVD laser cavities. However, with the help of ANDi and AS mode-locking techniques, it is possible to achieve ultrafast pulses at these wavelengths.

7.3 Simulation results

Short pulse generation is directly related to gain bandwidth of the medium at a particular wavelength by Equation 7.1

$$\Delta\tau\dot{\Delta}(\nu) = 0.411 \tag{7.1}$$

Obviously, Equation 7.1 assumes that emission spectrum is Gaussian shaped. With the help of this equation, it can be calculated that a mode-locked laser at 520 nm can be built because Pr exhibits $\sim$ 25 nm of bandwidth around 520 nm (shown in Figure 7.2) which can generate pulses as short as $\sim$ 16 fs. Another promising wavelength is 605 nm. With approximately 10 nm gain BW, transform limited pulse duration of $\sim$ 50 fs is possible. Unfortunately, $\sim$ 2 nm gain bandwidth at 635 nm is not enough to support very short pulses, but ps pulse generation is possible.

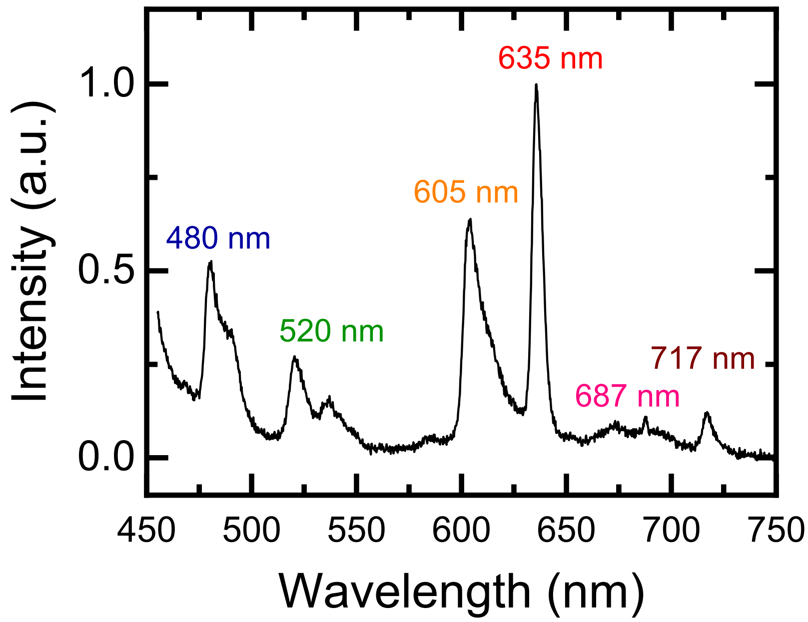

Figure 7.2: Pr doped fiber emission spectrum.

7.3.1 Simulation results at 520 nm

The simulation is performed using standard split step Fourier method. The laser cavity (shown in Figure 7.3) is based on the all normal dispersion (ANDi) configuration. There is no passive SMF is considered because of the large GVD of the gain fiber itself. The gain fiber exhibits parameters such as 5.2 μm diameter and numerical aperture of 0.08 (V number = 2.045) similar to [143]. The other simulation parameters are listed in Table 7.1. The numerical simulation results show a stable mode-locked operation of an ANDi Pr doped fiber laser at 522 nm with a 10 nm wide spectral filter. Figure 7.4(a) shows the simulation result of a Batman shaped spectrum, which is a typical output spectrum shape of an ANDi laser, and the de-chirped pulse duration [shown in Figure 7.4(b)] ($\sim$ 125 fs). The output pulse energy is around $\sim$ 3 nJ. Even though the numerical simulation does not guarantee matching experimental results, it is encouraging enough to proceed with the

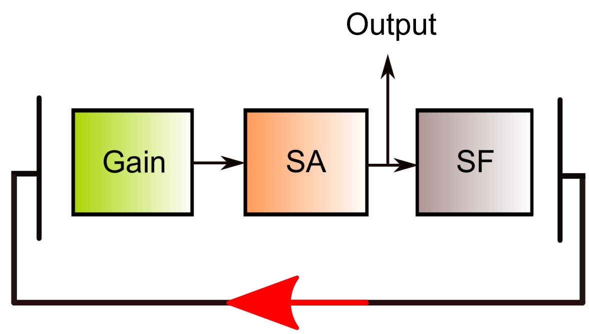

Figure 7.3: Conceptual schematic of the Pr doped ANDi fiber laser. SA, saturable absorber; SF, spectral filter.

experiments. Instead of an ANDi mode-locking operation, an amplifier similariton (AS) or self-similar (SS) pulse evolution can be used to mode-lock the Pr-doped visible fiber laser. The conceptual cavity diagram remains the same as Figure 7.3. Only this time, longer section of gain fiber (2.5 m) is used as it facilitates SS type of evolution. A sharp spectral filter with FWHM BW of 4 nm is used. Figure 7.5(a) shows the numerically simulated AS mode-locked operation at 522 nm. The dechirped pulse duration is around $\sim$ 150 fs

Table 7.1: Parameters used for the numerical simulation of mode-locked Pr-doped ANDi fiber laser

Parameter	Value
L_{Gain}	110 cm
Spectral filter BW	10 nm
$\beta_{2\ Pr:ZBLAN}$	820 fs^2/cm
$\gamma_{Pr:ZBLAN}$	0.000047 $\mathrm{W}^{-1}cm^{-1}$
g_0	30 dB
E_{sat}	0.16 nJ
OC	0.8

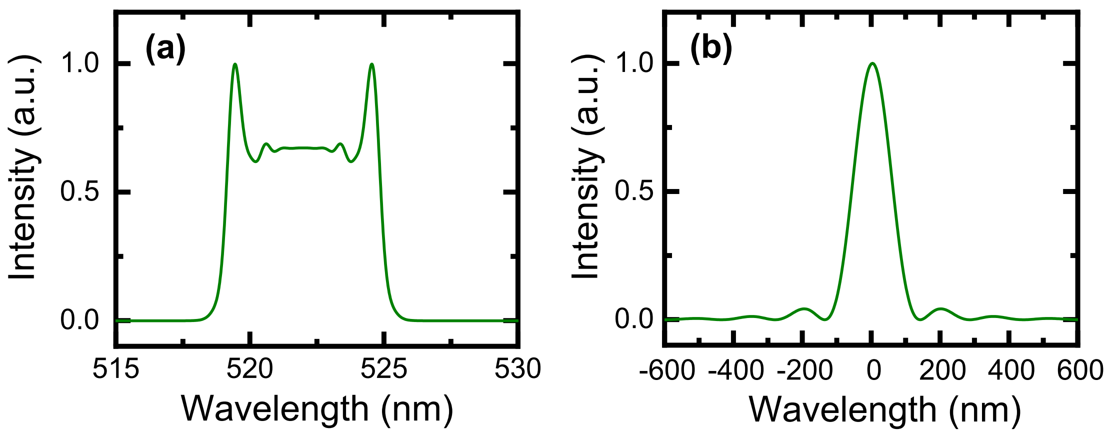

Figure 7.4: Mode-locked Pr doped ANDi fiber laser simulation results at 520 nm a) simulated output spectrum b) dechirped output pulse

[Figure 7.5(b)] with a pulse energy of $\sim$ 3 nJ. Both, ANDi and AS simulations are primary results and they can be further optimized to achieve high energy and sub 100 fs pulses.

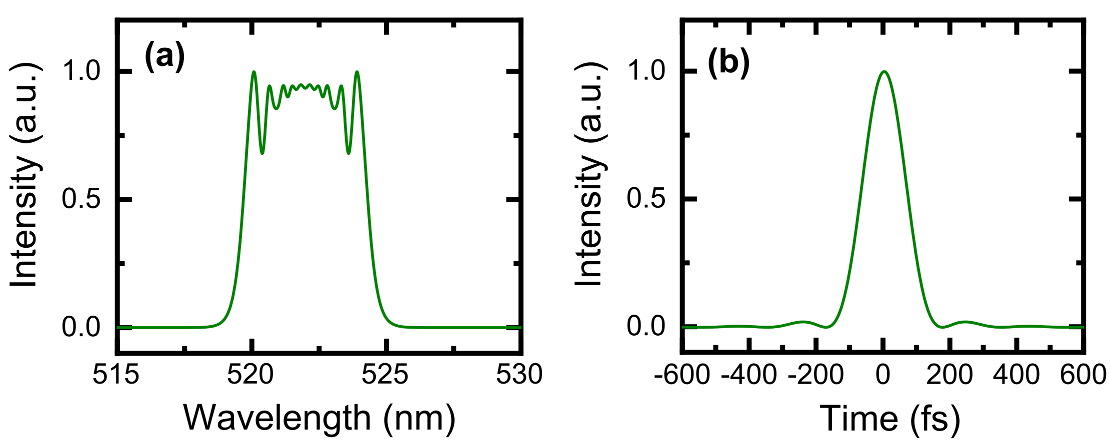

Figure 7.5: Mode-locked Pr doped AS fiber laser simulation results at 520 nm a) simulated output spectrum b) dechirped output pulse

7.3.2 Simulation results at 605 nm

For simulations at 605 nm, ANDi type of cavity is considered. The entire gain BW is utilized as a spectral filter. The simulation parameters are similar to those listed in Table 7.1 except $\beta_2 = 685\ fs^2/cm$. Figure 7.6(a) shows the numerically simulated ANDi mode-locked spectra and the dechirped pulse duration is around $\sim$ fs [Figure 7.6(b)]. The pulse energy is $\sim$ 1 nJ.

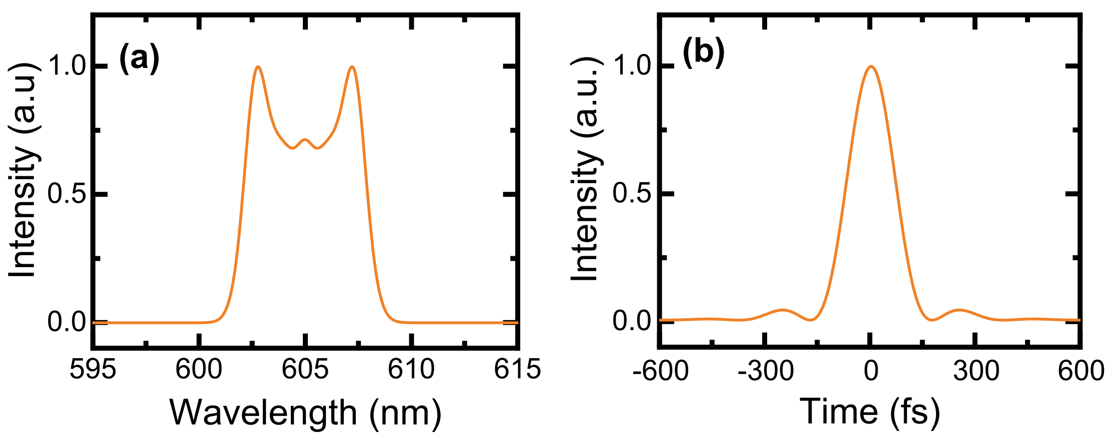

Figure 7.6: Mode-locked Pr doped AS fiber laser simulation results at 605 nm a) simulated output spectrum b) dechirped output pulse ($\sim$ 150 fs)

Instead of an ANDi mode-locking operation, AS/SS laser cavity can be simulated. Figure 7.7(a) shows the numerically simulated spectra while 7.7(b) shows the dechirped output pulse. The pulse energy is $\sim$ 1 nJ.

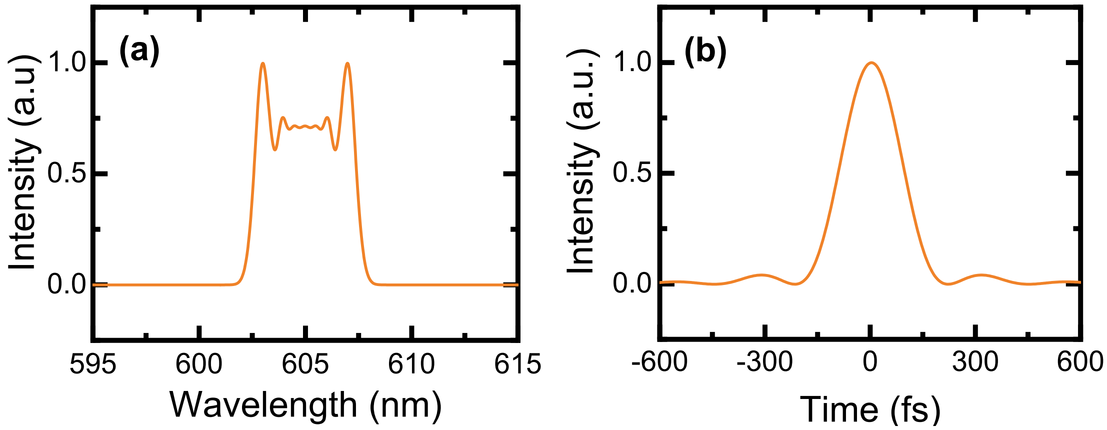

Figure 7.7: Mode-locked Pr doped AS fiber laser simulation results at 605 nm a) simulated output spectrum b) dechirped output pulse ($\sim$ 200 fs)

7.3.3 Simulation results at 635 nm

As explained earlier, it is difficult to get fs pulses at 635 nm due to limited gain BW at this wavelength but the methods to generate ultrashort pulses beyond gain BW are explained in Chapter I and the conceptual laser cavity (Figure 7.8) used for simulation is based on such methods. The other simulation parameters are listed in Table 7.2. Figure 7.9 shows the numerical simulation result of the proposed AS fiber laser.

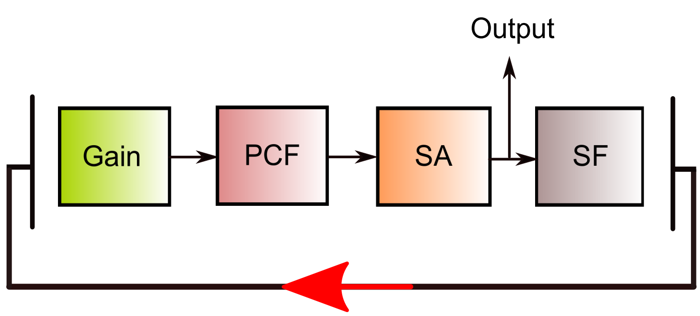

Figure 7.8: Conceptual schematic of the Pr doped modified AS fiber laser. PCF, photonic crystal fiber; SA, saturable absorber; SF, spectral filter.

These results are not optimized but the general conjecture is much shorter pulses can be generated by introducing PCF inside the cavity.

Table 7.2: Parameters used for the numerical simulation of mode-locked Pr doped modified AS fiber laser

Parameter	Value
L_{Gain}	250 cm
L_{PCF}	15 cm
Spectral filter BW	4 nm
$\beta_{2\ Pr:ZBLAN}$	647 fs^2/cm
$\beta_{2\ PCF}$	34.7 fs^2/cm
$\gamma_{Pr:ZBLAN}$	0.000047 W$^{-1}cm^{-1}$
γ_{PCF}	0.0002448 W$^{-1}cm^{-1}$
g_0	30 dB
E_{sat}	0.074 nJ
OC	0.8

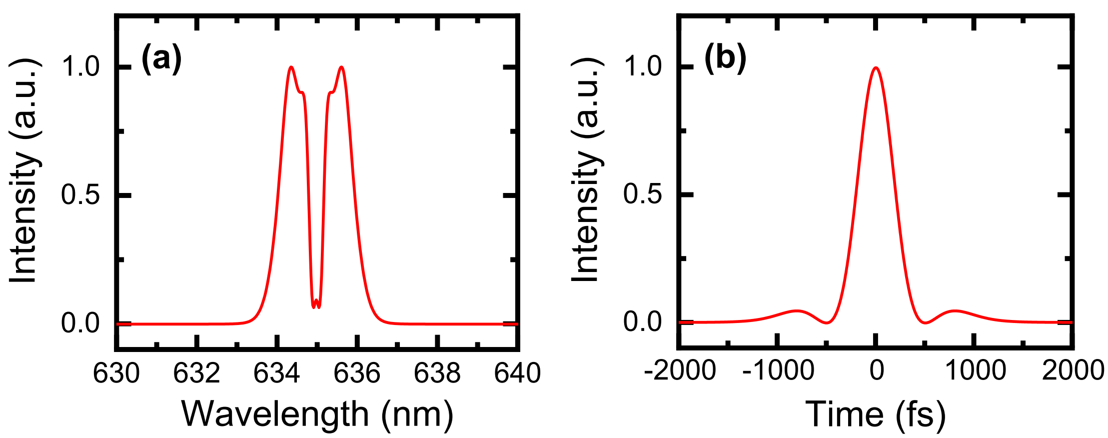

Figure 7.9: Mode-locked Pr doped modified AS fiber laser simulation results at 635 nm a) simulated output spectrum b) dechirped output pulse ($\sim$ 350 fs).

7.4 Proposed Pr doped fiber laser experimental cavities and design considerations

A sample Pr doped fiber laser is shown in Figure 7.10. The cavity is ANDi type configuration where a high power GaN diode at 442 nm laser pumps a Pr doped fiber. Although in recent years, multiwatt blue laser diodes are easily available, very few options for fiber coupled blue laser diode are available and they are expensive. Also, 442 nm /520 nm (or 605 nm /635 nm) is not available commercially. Even with a customized WDM, the splicing between a standard silica fiber and ZBLAN fiber is difficult and could introduce huge loss. Therefore, an all-fiber Pr doped fiber laser version is not a plausible option at the moment. NPE is exploited as an artificial saturable absorber to initiate the ANDi mode-locking. A thin film based filter is used as a spectral in the cavity. But a birefringent plate and polarizer based Lyot filter can also be utilized. Another design to explore is Pr doped AS fiber laser. The main difference between two laser design is spectral filter. For the AS laser, grating and collimator based spectral filter can be used. In further subsections, the important components in this laser cavity are explained in detail.

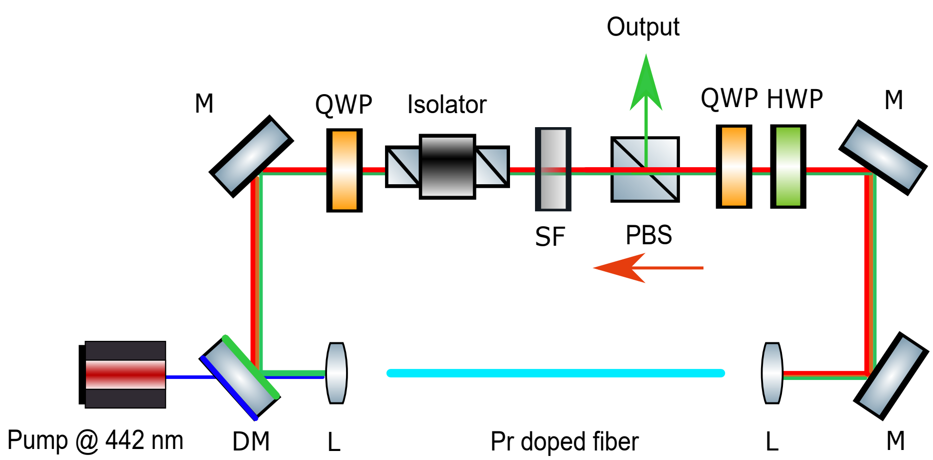

Figure 7.10: Proposed experimental mode-locked Pr doped ANDi fiber laser. DM, dichroic mirror; L, lens; M, mirror; HWP, half waveplate; QWP, quarter waveplate; PBS, polarizing beam splitter; SF, spectral filter.

7.4.1 Pump diode

A 3 W GaN diode at 442 nm (NDB7K75 from Nichia Co.) is selected due to the high absorption cross-section of Pr^{3+} ions around this wavelength. This laser diode consists of two stacks of active areas and hence the beam emitted from the diode contains two transverse electric (TE) modes and every TE mode is quasi Gaussian mode. As the beam propagates, the modes become bigger in size and collectively beam divergence increases and the beam becomes rectangular. Experimentally recorded far field pattern of NDB7K75 is shown in Figure 7.11. The divergence for this beam is 15 $^\circ$ $\times$ 45 $^\circ$. It is very difficult to collimate such a beam or focus it into a very small spot. Therefore, coupling optics needs to be designed to pump a Pr doped gain fiber with this pump diode.

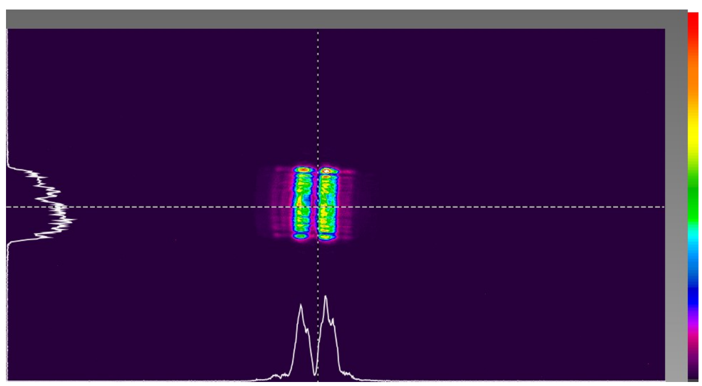

Figure 7.11: Measured far field pattern of NDB7K75.

7.4.2 Gain fiber

A double clad gain fiber can ease the coupling of the pump light as explained in Chapter I. The comparison between specifications of the three DC fibers used in the experiments is given in Table 7.3. Two of them are Pr doped ZBLAN fibers and one of them is Pr doped waterproof glass fiber.

Table 7.3: Pr doped fiber specifications

Parameter	Pr:WPFG	Pr,Yb:ZBLAN	Pr:ZBLAN
Fiber manufacturer	Sumita	Fiberlabs	LVF
Core diameter	5 μm	11 $\pm$ 2 μm	5.5 μm
Core numerical aperture	0.08	0.20 $\pm$ 0.02	0.08
V number	2.058 @ 635 nm	11 @635 nm	2.4 @635 nm
1^{st}/ 2^{nd} clad diameter	14/270 μm	125/210 μm	115 μm
1^{st} clad NA	0.29	0.50	0.48
Pr/Yb concentration	3000 ppm/NA	10000/10000 ppm	6000 ppm

7.4.3 Coupling optics

Pump beam diameter should be reduced to a size matching fisrt clad dimentions of the gain fiber. Table 7.3 shows that for Pr:ZBLAN fibers, focusing pump beam to a diameter of $\sim$ 120 μm will be sufficient for a good coupling while for Pr: WPFG fiber, that number is much smaller i.e. 14 μm. Therefore, two separate coupling optics configurations are designed. Figure 7.12(a) shows coupling optics configuration for waterproof fibers. It consists of a pair of concave and convex cylindrical lenses to collimate extremely elliptical beam from the laser diode. This collimated beam can be focused further to very small spot size. The coupling optics for ZBLAN fibers is illustrated in Figure 7.12(b). Using an aspheric lens, the elliptical beam from the pump diode is focused into a very tiny spot. Obviously, the focused beam is also elliptical. But around the focal spot, one can find a fairly circular beam which can be imaged using 4f lens system. By using a second lens with an appropriate focal length in the 4f system, the spot size of the focused beam can be further scaled down.

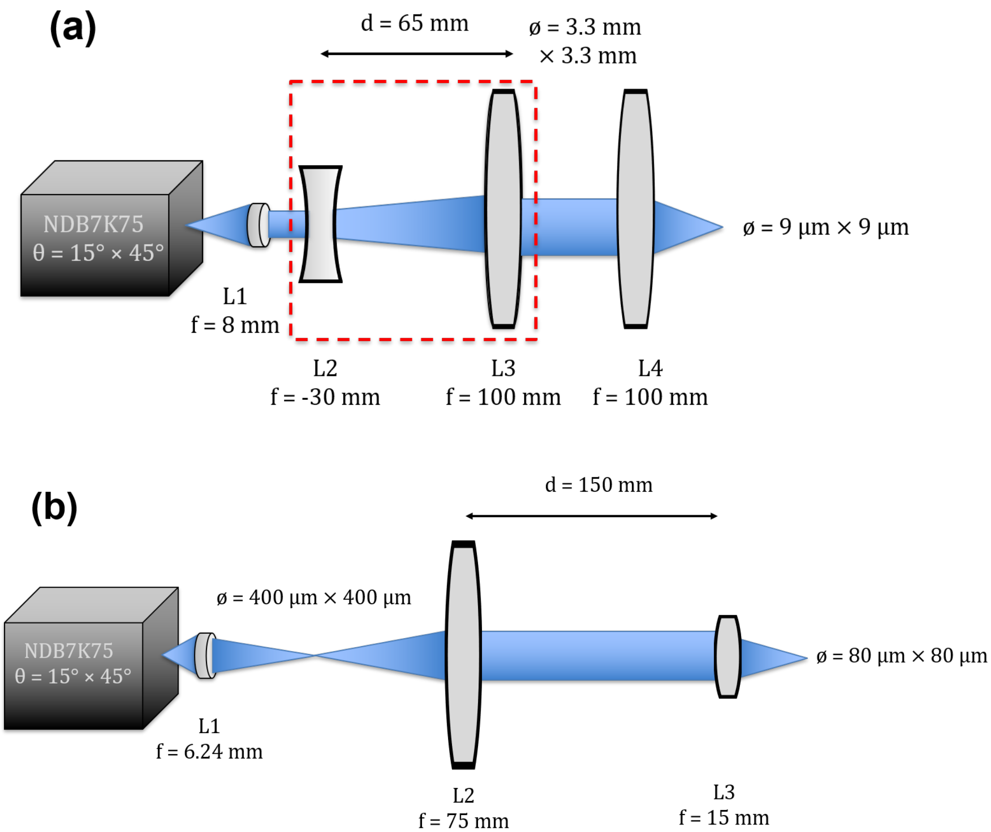

Figure 7.12: Pump coupling optics configuration (a) using concave-convex cylindrical lens configuration (b) modified 4f system.

7.5 Experimental results

In this section, experimental results for all the three DC fibers are given. Several studies have been carried out to determine the suitable gain medium out of these three fibers for this project. Although the goal of the project is to build a ring oscillator, to understand Pr doped gain medium properties thoroughly linear laser cavities are built initially with each of the gain fibers.

7.5.1 Experimental results for Pr:WPFG fiber

Initially, Pr:WPFG fiber is chosen to build a linear CW laser oscillator because such promising result is demonstrated before and the fiber used in the experiment is exactly similar to the one in [143]. As normal fiber stripping and cleaving techniques are redundant for these fibers, it is important to prepare fiber ends to ensure good pump light coupling. The fiber is inserted in a zirconia ferrule and both ends of the fiber are polished using polishing sheets and plates. It is important to note that the zirconia ferrule is customized especially for its length and bore dimensions (Figure 7.13).

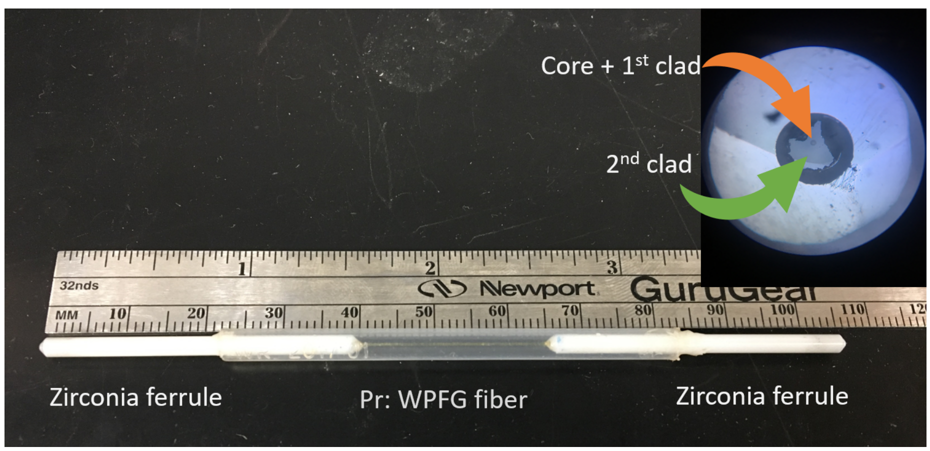

Figure 7.13: Pr: WPFG fiber with zirconia ferrule (L=105 mm). The inset shows the polished fiber end viewed through microscope.

The pump light is coupled using configuration shown in Figure 7.12(a). First, the pump coupling efficiency of an undoped silica fiber having the somewhat similar core and first clad dimensions as WPFG fiber is determined. The measured maximum coupled pump power into the undoped fiber core is 9.5 mW, while the incident pump power is 34 mW, confirming the 28 % of coupling efficiency. This poor coupling efficiency can be attributed to a bad polished end of the fiber end on the pump coupling side and low NA of the first clad. Figure 7.14(a) shows the lightly glowing Pr doped fiber and the ASE emitted from the fiber is illustrated in Figure 7.14(b) which depicts multiple visible emissions, 605 nm being the strongest.

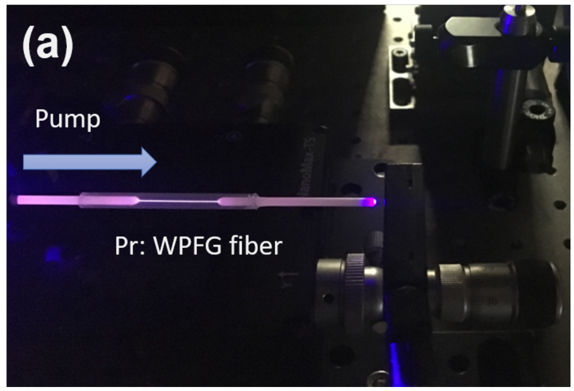

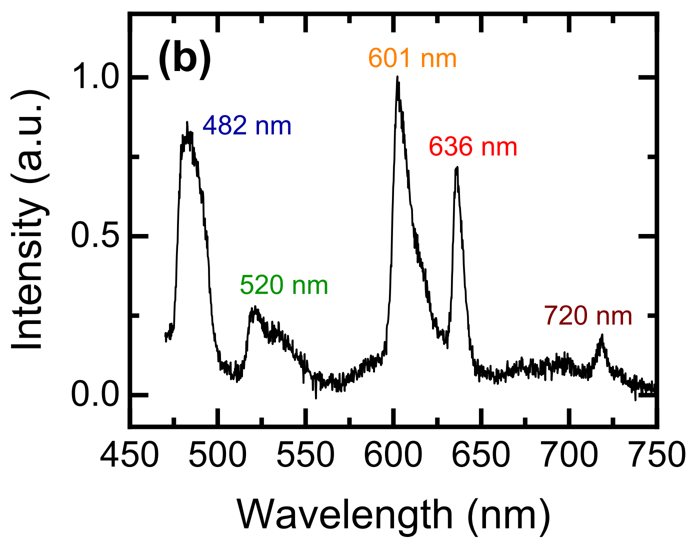

Figure 7.14: Pr: WPFG fiber with zirconia ferrule (L=105 mm). The inset shows the polished fiber end viewed through the microscope.

A linear laser cavity is constructed (Figure 7.15) to determine the approximate pump power required for lasing. The design is unsuccessful for the following reasons

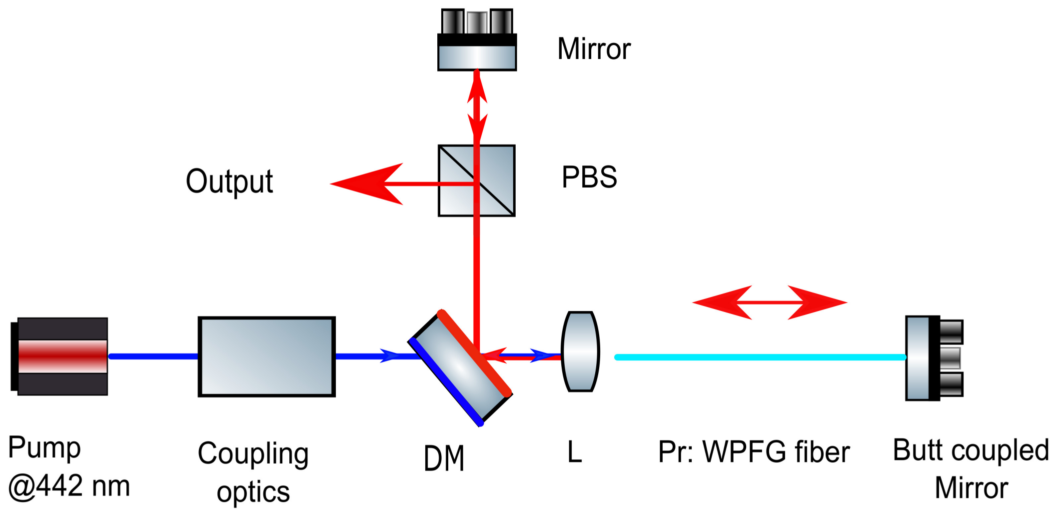

Figure 7.15: Experimental linear CW Pr:WPFG fiber fiber laser cavity. DM, dichroic mirror; L, lens; M, mirror; PBS, polarizing beam splitter

- The pump coupling efficiency is poor. The polishing technique is very customized and polishing quality can not be improved further.
- The pump is not completely absorbed with the 105 mm section of the fiber. But longer fiber can not be used because the fiber is very brittle and to support it, longer zirconia ferrule is needed which is not available commercially.
- Any efforts of pumping higher resulted in the burning of the polished end near the butt coupled mirror.

In conclusion, it is decided to explore the ZBLAN host system.

7.5.2 Experimental results for Pr, Yb:ZBLAN fiber

Pr:ZBLAN DC fibers are not commercially available, but Pr, Yb co-doped fibers are available which are primarily used for 1300 nm amplification. An upconversion laser emitting at the visible wavelength can also be built by pumping this fiber with 850 nm. But as upconversion laser has very little efficiency, that option is not considered here. Handling of Pr,Yb: ZBLAN fiber is much easier than Pr: WPFG fiber. It can be stripped by soaking it in Acetone. The stripped ends can be cleaved with any cleaver with adjustable tension. The surface flatness and the angle of the cleaved fiber ends is confirmed for each cleaving to achieve a low-loss cavity, since the pump coupling efficiency and cavity loss depended heavily on the condition of the fiber ends.

For the initial experiment, 1 m Pr,Yb: ZBLAN is used to construct a linear CW oscillator as shown in Figure 7.16. As per Table 7.3, this fiber is multimode (V number = 11), hence

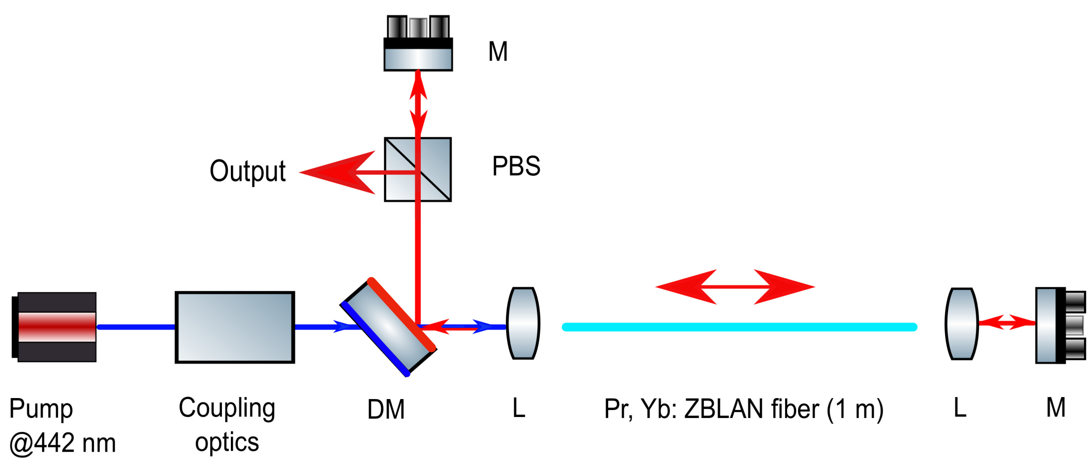

Figure 7.16: Linear CW Pr,Yb: ZBLAN fiber fiber laser cavity. DM, dichroic mirror; L, lens; M, mirror; PBS, polarizing beam splitter.

pump coupling is very easy and the coupling efficiency of 67 % of coupling efficiency is achieved. The recorded ASE for the fiber is similar to the one in Figure 7.2, emission at 635 nm being the strongest. A very weak CW is obtained (shown in Figure 7.17) when the input pump power is ~ 700 mW. It can be also seen that the output still has an unabsorbed pump which means the length of the fiber is not sufficient. Increasing input pump power leads to the burning of the Pr, Yb: ZBLAN fiber. This underlines the fact that the gain fiber length is very crucial.

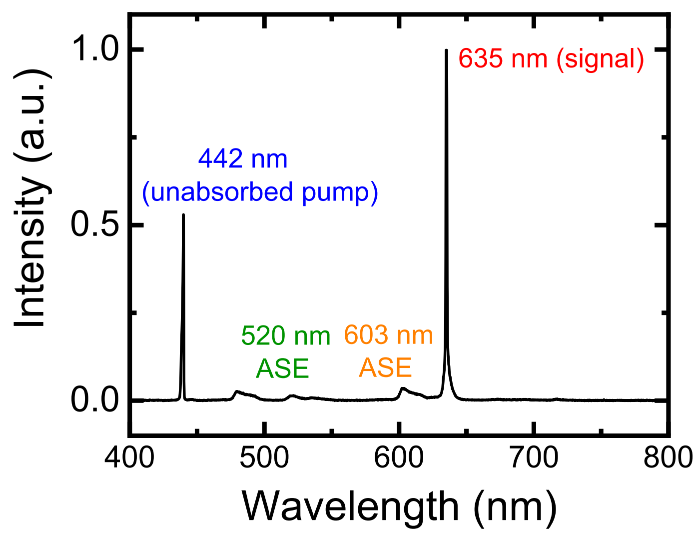

Figure 7.17: CW oscillation at 635 nm for Pr,Yb: ZBLAN fiber laser. Unabsorbed pump at 442 nm is seen.

7.5.3 Experimental results for Pr:ZBLAN fiber

Okamoto *et al.* found that the ASE intensity at 635 nm was 200 times higher for Pr:ZBLAN fiber than that for Pr,Yb: ZBLAN fiber by comparing the maximum ASE power [148]. Therefore, the next experiment is done with Pr:ZBLAN fiber and the fiber specifications are listed in Table 7.3. This fiber is single mode at 635 nm (V number = 2.4) and also its first clad is big enough to accept the pump beam. A linear cavity is built using 8 m of fiber and is shown in Figure 7.18(a). Figure 7.18(b) represents a photograph of the 635 nm Pr:ZBLAN fiber laser. It is possible that the light coming out of the front end of

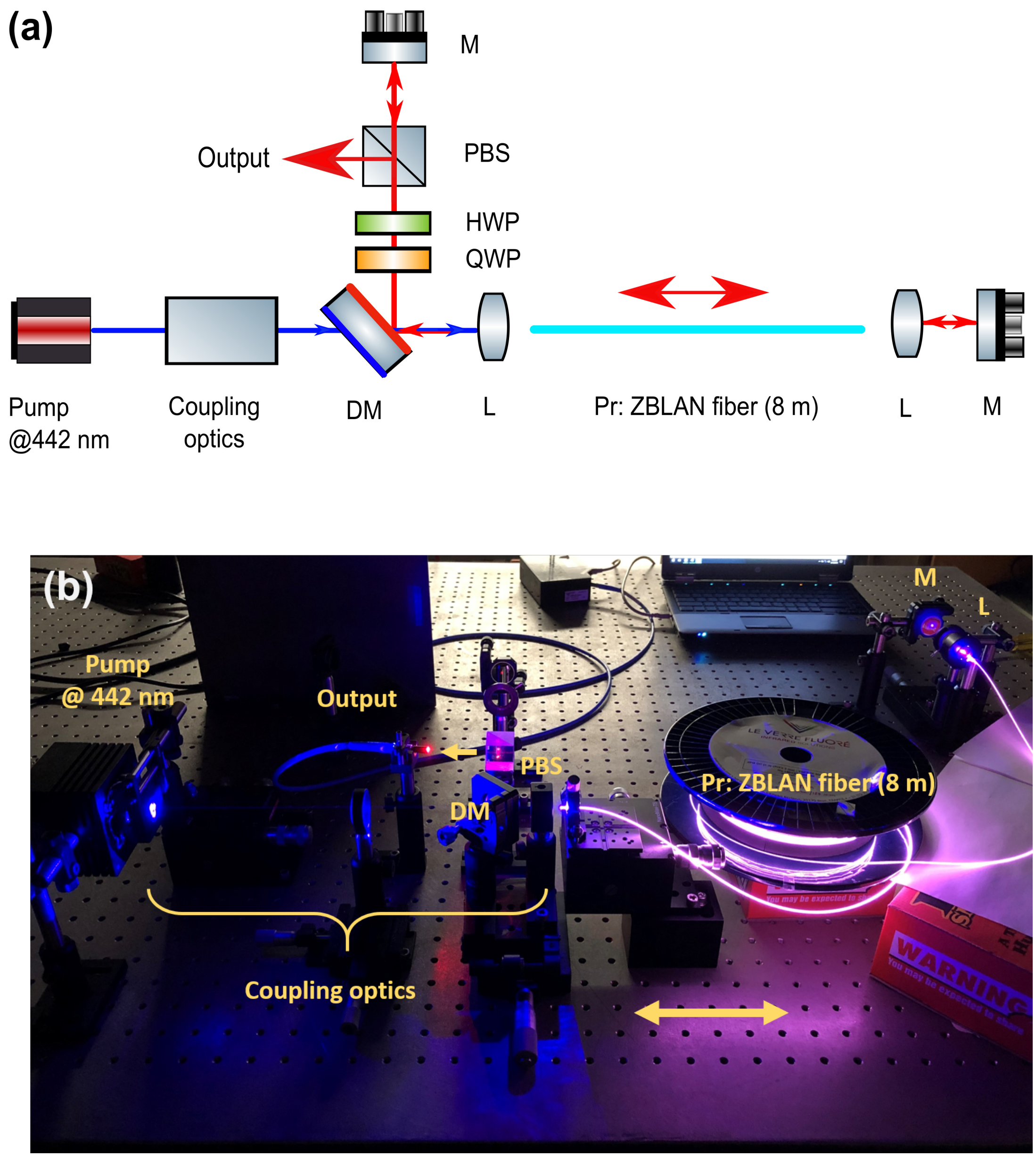

Figure 7.18: Experimental 635 nm Pr: ZBLAN CW fiber laser linear cavity. DM, dichroic mirror; L, lens; M, mirror; PBS, polarizing beam splitter; HWP, half waveplate; QWP, quarter waveplate (a) schematic (b) photograph.

the fiber may not be s-polarized, hence a pair of HWP and QWP is introduced to modify the polarization state and to get maximum output power. The CW output is reported in Figure 7.19(a) and it can be seen that the pump is entirely absorbed. Figure 7.19(b) depicts laser input-output characteristics which conversion efficiency of 17 %.

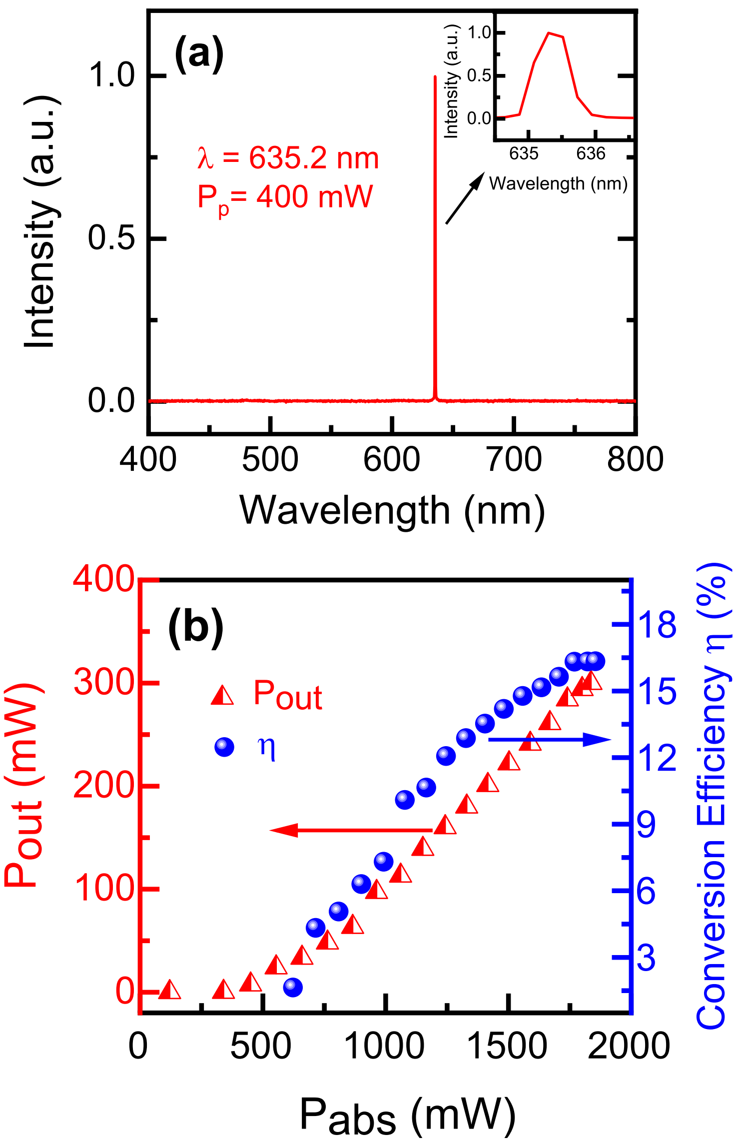

Figure 7.19: Pr: ZBLAN fiber laser dataset (a) CW oscillation at 635 nm. Inset shows the close-up view of the optical spectra (b) input-output characteristics as a function of threshold absorbed pump power.

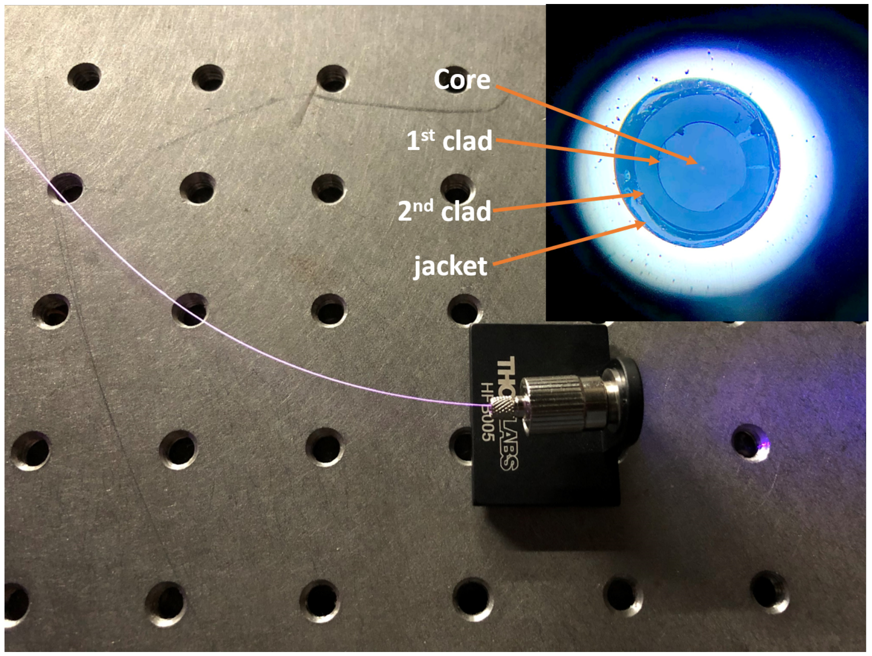

Figure 7.20: Connectorized Pr: ZBLAN fiber. The inset shows the polished fiber end viewed through a fiber microscope.

Even though $\sim$ 300 mW of output power can be obtained by utilizing 3 W of maximum pump power, this CW efficiency is still less than other gain media such as Yb, Er or Tm. The only way to increase the CW efficiency is to avoid free space coupling of light in the cavity. This can be done by depositing a thin film mirror with a high reflection at 635 nm on fiber ends. But this requires connectorization and polishing of Pr:ZBLAN fiber which is accomplished and shown in Figure 7.20. Unfortunately, due to lack of the thin film deposition technology, research regarding a high power CW fiber laser at 635 nm is not pursued.

As explained earlier, due to a narrow gain BW at 635 nm, it is better to construct a modified AS type of cavity which is a ring oscillator. This cavity [Figure 7.21(a)] contains 4 m of Pr:ZBLAN fiber. Isolator maintains unidirectional operation and waveplates change

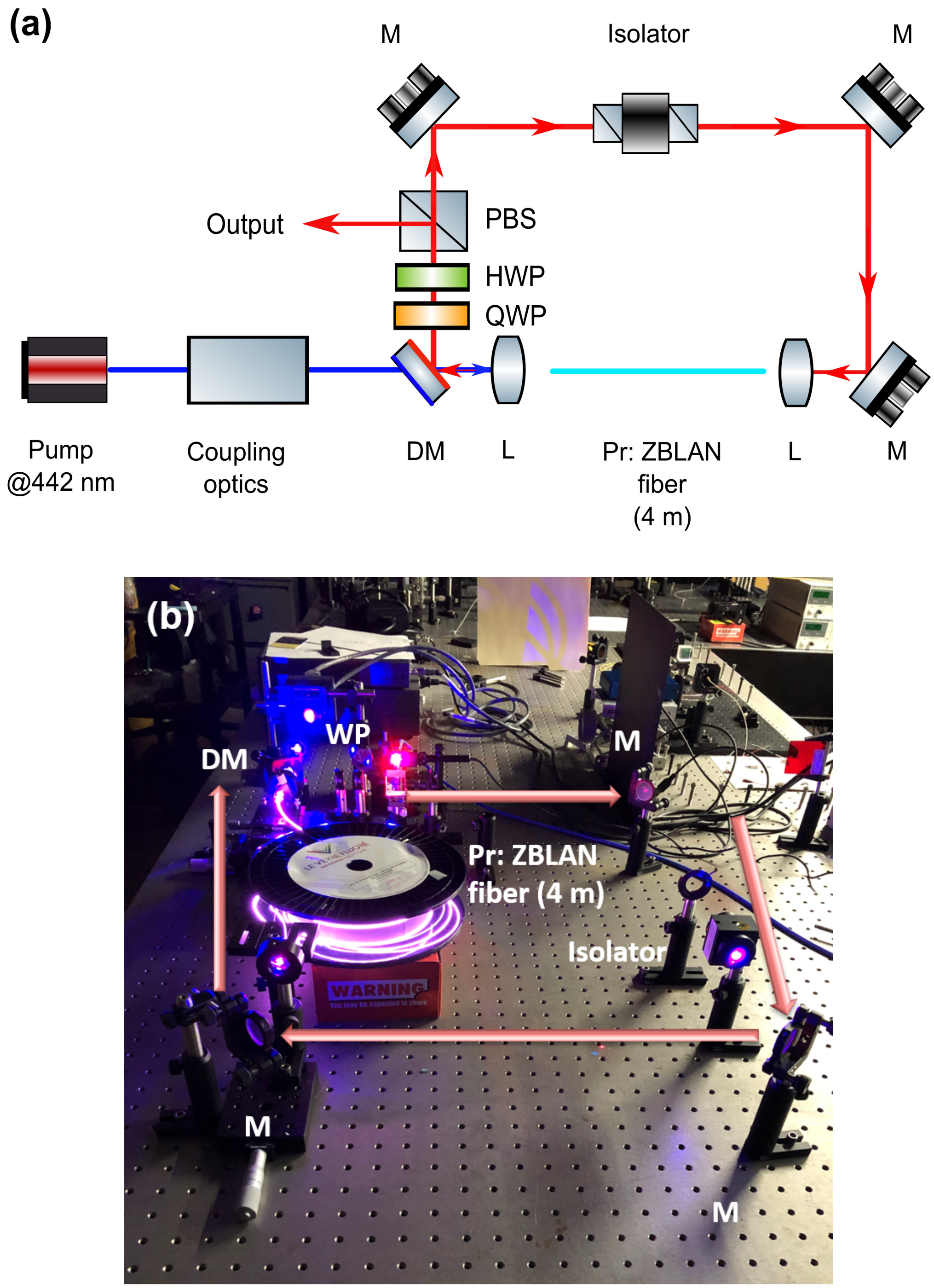

Figure 7.21: Experimental 635 nm Pr: ZBLAN CW fiber laser ring cavity. DM, dichroic mirror; L, lens; M, mirror; PBS, polarizing beam splitter; HWP, half waveplate; QWP, quarter waveplate (a) schematic (b) photograph.

the state of polarization to achieve maximum power at the output port. Figure 7.21(b) shows the picture of this laser. The CW operation is achieved at an absorbed pump power of 300 mW. The input-output characteristics of this laser are shown in (Figure 7.22). Compared to linear CW operation, conversion efficiency is low (approximately 7 %) at ~ 1 W of absorbed pump power. When pump power is increased beyond this point, the fiber tip burns. This can be due to the insufficient absorption of the pump in the gain medium. It can be solved using a longer gain fiber.

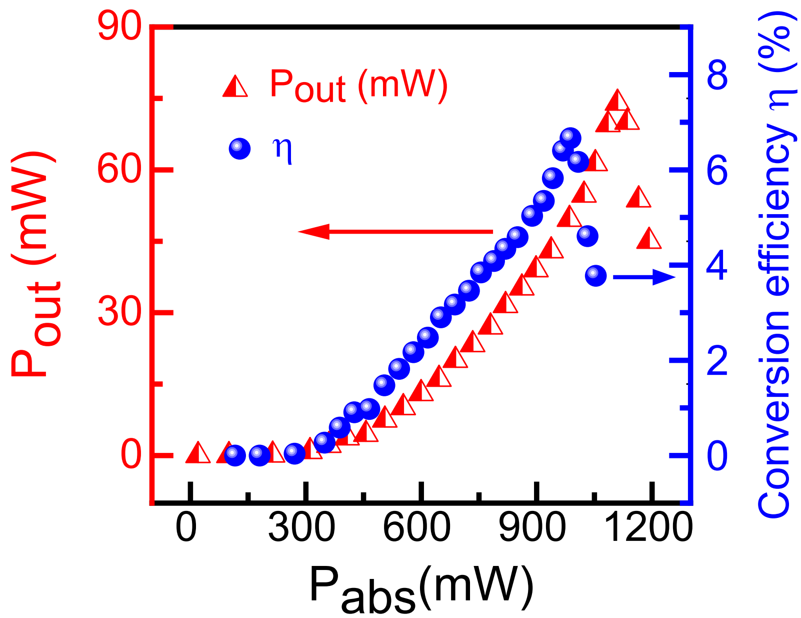

Figure 7.22: Input-output power characteristics as a function of absorbed pump power for 635 nm Pr:ZBLAN fiber ring oscillator

7.6 Discussion and future direction

The future step in this project is definitely building AS type of oscillator and including a highly non-linear fiber (HNLF) inside the cavity. Obviously, the CW efficiency of the ring cavity must be improved by taking necessary measures such as proper length of the gain fiber. With the help of numerical simulations in this chapter, the parameters of HNLF are known. Unfortunately, such fiber is not commercially available but a customized HNLF may renew this research topic. On the other hand, to build ANDi/AS type of oscillators at 520 nm is much easier. But unfortunately, Pr:ZBLAN fibers available in the market are targeted towards the generation of high power at 635 nm. A customized Pr:ZBLAN fiber with strong ASE at 520 nm will be a perfect candidate to facilitate constructing these oscillators. Clearly, if ZBLAN technology becomes mature enough to produce visible wavelength passive fibre components such as WDMs, isolators and collimators commercially, then future of ultrafast oscillators at visible wavelengths looks promising.

CHAPTER VIII

FUTURE DIRECTIONS FOR ULTRAFAST FIBER LASERS RESEARCH

In this chapter, future research directions aimed at improving the performance of ultrafast mode-locked fiber oscillators are suggested. There are several directions in which fiber laser research can head but this discussion is limited to the spectral filter research reported in this dissertation. First, a brief summary is given of each of these directions. Then, in a separate section, effect of higher order spectral filtering in mode-locked fiber lasers is studied numerically which leads to very interesting conclusions. Some primary experimental results are also provided.

8.1 Summary of future research ideas

- In Chapter II, a tunable bandwidth (BW), all-fiber spectral filter is presented. The experiments are carried out for ytterbium (Yb) doped mode-locked fiber laser at 1 μm. Similar experiments can be carried out for all normal dispersion (ANDi) fiber lasers at different wavelengths utilizing different gain media. For example, erbium (Er) which emits at 1.5 μm wavelength, where telecommunications systems operate is worth investigating so as Thulium (Tm) which has emission around 2 μm is very crucial wavelength with respect to sensing and medical applications.

- Noise-like pulses (NLP) are high energy wavepackets that are made up of multiple pulses with random pulse width, intensity and phase [149]. They have gained importance because of their broadband spectrum with high pulse energies that are beneficial for material processing and supercontinuum generation [150]. In general, the NLP generation is attributed to the birefringence of the laser cavity in a combination with the nonlinear pulse propagation [151]. As this spectral filter is birefrinegent fiber based, the laser cavity in Chapters II and III are perfectly capable. In the next section, such NLP mode-locked spectrum is experimentally demonstrated.

- In Chapter III, the same spectral filter is used to control multipulse dynamics. Such versatile spectral filter can be used in realizing dual wavelength mode-locked lasers. Mode-locked fiber lasers that generate two frequency combs with different frequency intervals are vital in low-complexity dual-comb metrology research. Experimental evidence of such mode-locking for the experimental cavity in Chapter III is provided in the upcoming section. But for other gain media like Tm which has a larger gain BW compared to Yb, this spectral filter can be employed more efficiently to obtain dual mode-locking operation.

- Further, this spectral filter can be exploited for developing ps fiber based light sources for Coherent anti-Stokes Raman scattering (CARS) microscopy. A practical light source for CARS imaging needs to satisfy this important requirement - the excitation pulse should have a narrower spectral width than the vibrational resonance. Therefore, a transform-limited pulse with a duration of several picoseconds is typically ideal. Our initial experiments show that this spectral filter is capable of generating spectra with a very narrow spectral BW. Obviously, more probing in this research matter is required.

- It is very evident from Chapter IV that the first experimental demonstration of complex Swift Hohenberg equation (CSHE) based dissipative soliton fiber laser opens up multiple new research directions. The next step in this research would be implementing higher order or multipeak filter in mode-locked fiber lasers. In this chapter, some preliminary results are provided in this direction. Besides this, it is worth looking into what happens to different types of fiber laser cavities such as self-similar (SS) or Mamyshev oscillator if a fourth order spectral filter is used in these cavities.

- Chapter V explores the idea of tuning the central wavelength of mode-locked fiber laser using grating-collimator based spectral filter. This laser offered 70 nm tunabilty covering wavelengths from 1030 -1100 nm. But it is really difficult to have good laser sources covering wavelengths between 990-1020 nm. The special wavelength of 1010 nm by itself can potentially provide a higher two photon excited fluorescence (TPEF) efficiency for some widely used biomolecules and dyes, e.g., Alexa Fluor 488 and emerald GFP [152]. Okhotnikov *et al.* cleverly made use of a 915 nm pump to pump Yb doped mode-locked laser [92]. Yb doped fibers have two prominent absorption regions; the narrow region but relatively high absorption cross section around 976 nm and the broad region but lower absorption cross section around 915 nm. However, one of the main challenges with using 976 nm sources is ensuring the wavelength stability of pump sources during laser operation. Therefore; careful thermal management is required for the stabilization of the pump diodes. On the other hand, although it has a lower absorption cross section compared to the 976 nm wavelength regime, the spectral region around 915 nm, another important absorption regime for Yb-doped fibers, offers a broad range of wavelengths usable. Although they demonstrated 90 nm wavelength tunabilty from 980 nm -1070 nm, the laser performance was not very good considering it emitted ps and very low energy pulses. All these drawbacks can be overcome by slightly modifying the fiber laser cavity in Chapter V - by pumping it with multimode high power 915 nm. An energetic pulsed light source spanning from 980 -1100 nm will definitely serve as an attractive source for non-linear imaging techniques.

- Chapter VI describes a method of generating ultrashort pulses by breaking the gain BW limit. Although the experiments involve Yb as a gain medium, this method is applicable to any other gain medium like praseodymium (Pr), dysprosium (Dy), terbium (Tb), samarium (Sm), etc. In our research, ultrafast pulses of duration of 17 fs are obtained. But it is still not close to a single cycle duration and the spectrum is also far away from being octave spanning. But building the same laser with a large mode area-photonic crystal fiber (LMA-PCF), the intracavity power can be scaled up and with the method of passive nonlinear spectral broadening inside this particular laser cavity, an octave-spanning, single cycle pulsed laser could be possible in the future.

- In Chapter VII, an attempt is made to build ANDi or SS type lasers at visible wavelength using Pr as a gain medium. The same efforts can be endured for other unconventional gain media like bismuth doped fiber to access 1300 nm.

8.2 Noise like pulses from a mode-locked fiber laser

Figure 3.3 shows the experimental cavity. The laser cavity is operated below lasing threshold and PC1 are tuned to get the spectral filter shape illustrated by Figure 8.1(a). For this laser, it is easier to get noise mode-locking when spectral filter BW approaches ASE BW. Then, pump power is increased and by adjusting PC2 and rotating intracavity waveplates, a noise mode-locked spectrum represented by Figure 8.1(b) can be obtained. It usually has a smooth bell shaped curve. In the temporal domain, it corresponds to a ps wavepacket consisting of an irregular train of fs pulses 8.1(c). This leads to fluctuations in the envelope parameters and noticeable while observing the pulse train on the oscilloscope. The difference between NLP train [8.1(d)- upper row] is compared with the non-NLP train emitted by a mode-locked laser [8.2(d)- lower row] and it can be seen that the NLP train

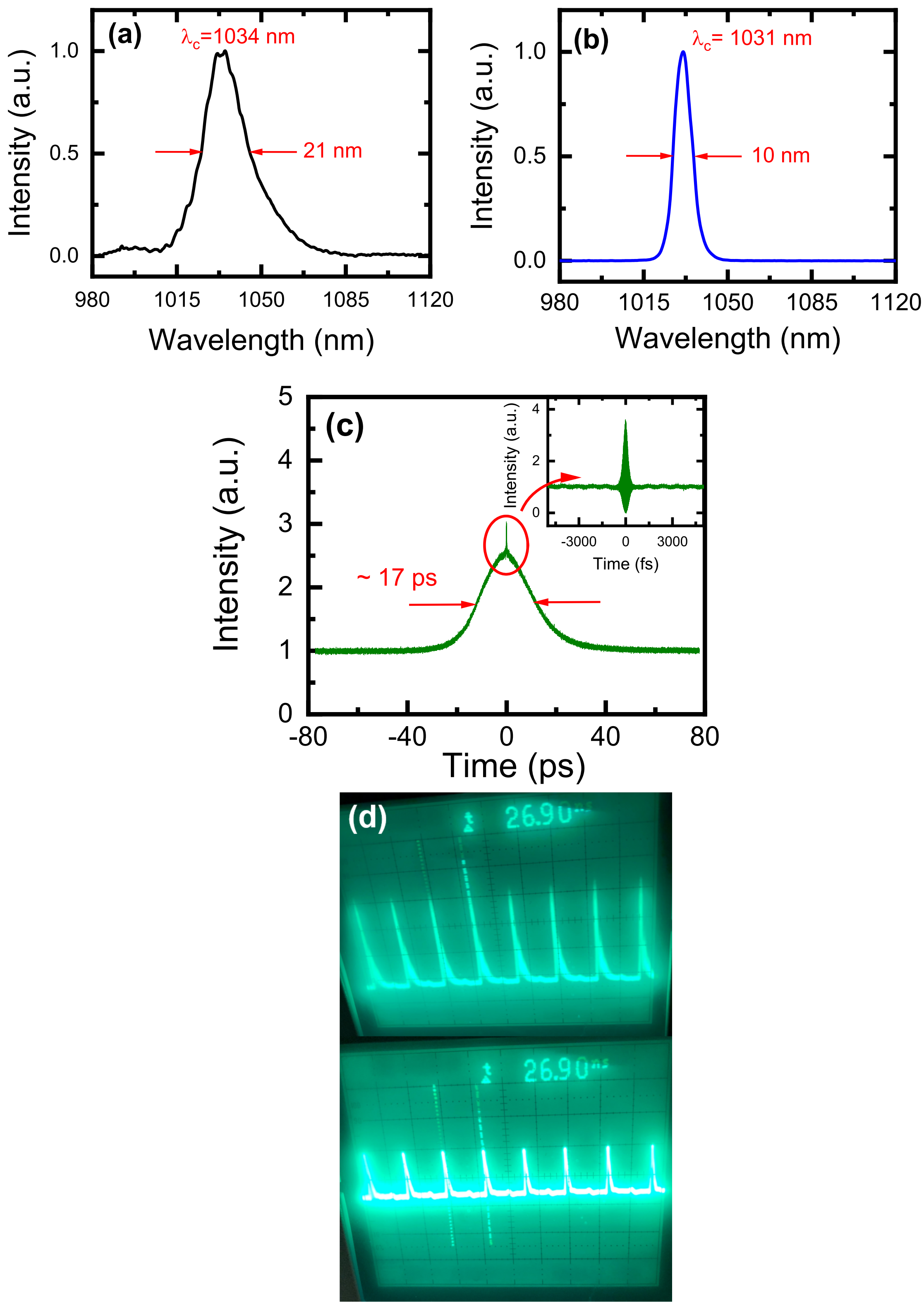

Figure 8.1: Measured (a) spectral filter output (b) noise mode-locked spectra (c) intensity autocorrelation of NLP. Inset shows short range interferometric autocorrelation (d) pulse train for NLP (upper row) and ANDi mode-locking (lower row).

is jittery. Still, the NLP energy is $\sim$ 8 nJ, higher than the standard ANDi mode-locked operation which offers 1-2 nJ pulses in single mode,single clad, single pump format.

8.3 Dual wavelength mode-locking

The experimental laser cavity is shown in Figure 3.3. The laser cavity is operated below lasing threshold and PC2 and PC3 are tuned to get the spectral filter shape illustrated by Figure 8.2(a). Then, pump power is increased and by adjusting PC1 and rotating intracavity waveplates, dual mode-locked spectra [Figure 8.2(b)] is achieved. The central wavelengths of the dual-wavelength mode locking laser are at 1020.5 nm and 1036 nm, respectively. The full width half maximum (FWHM) bandwidth (BW) of the two spectral envelopes are $\sim$ 8.5 nm and $\sim$ 9.5 nm, respectively. In this case, the spectral asymmetry of the mode locking spectra with different central wavelengths can be directly related to the irregular transmission of the spectral filter. This initial experimental result proves that this spectral filter can be useful for realizing dual wavelength mode-locked lasers.

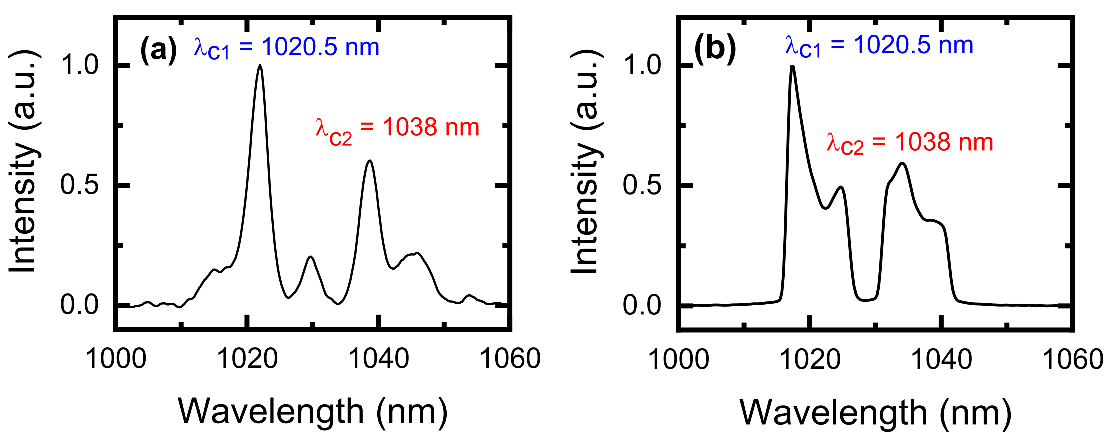

Figure 8.2: Measured (a) spectral filter output (b) dual mode-locked spectra.

It is possible to get an output spectrum with a very narrow spectral bandwidth from this laser (Figure 3.3). Such sample spectra are presented in Figure 8.3(a) and the associated spectral filter shape are given by Figure 8.3(b). The pulses are of a longer duration of 500 fs (0.5 ps) and the autocorrelation is shown in Figure 8.3(c). But mostly, with such a narrow spectrum, the laser is multipulsing and it is confirmed by a fast oscilloscope and the result is shown in Figure 8.3(d). The total pulse energy is 8.4 nJ which makes energy per pulse 1.67 nJ. Although pulses are still short ($\sim$ 500 fs), the spectral filter design could be further

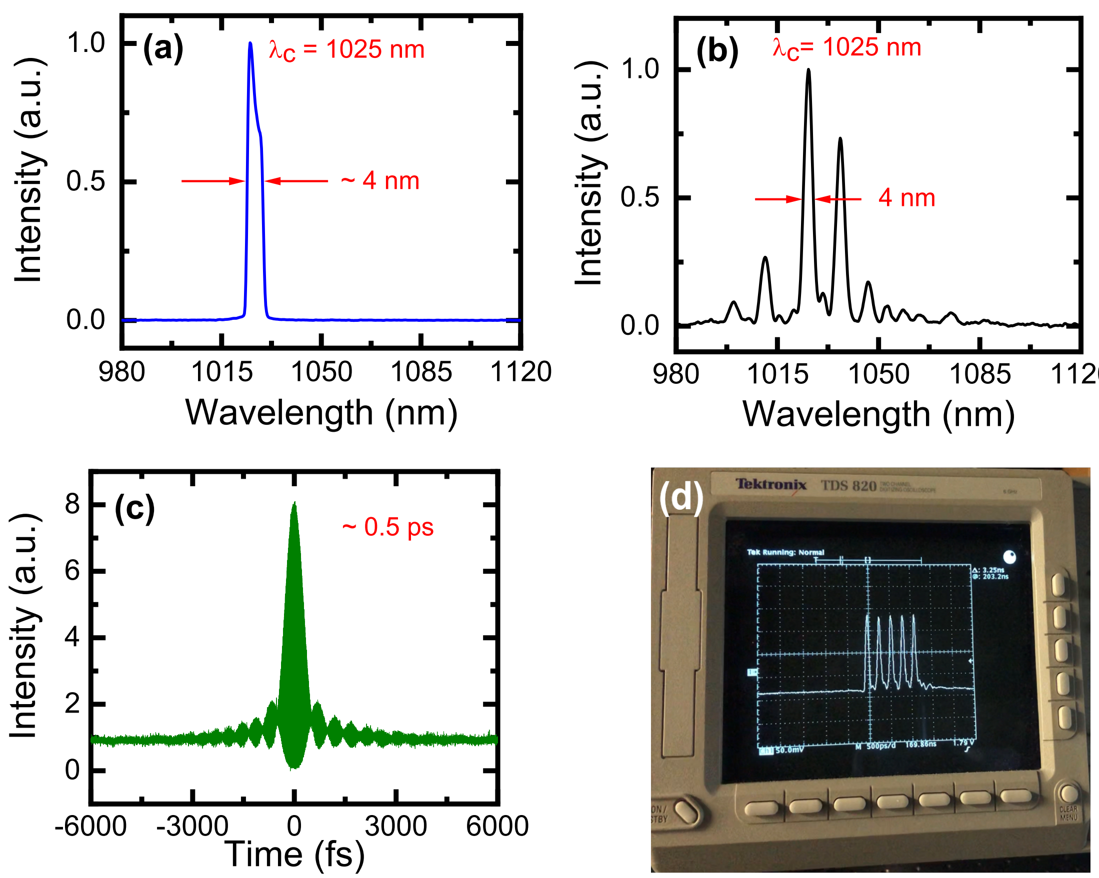

Figure 8.3: Measured (a) mode-locked spectra (b) spectral filter output (c) autocorrelation (d) pulse train.

studied for ps pulse generation.

8.5 Implementing higher order spectral filter in mode-locked fiber lasers

Numerical simulations are performed for the laser cavity illustrated in Figure 8.4 and the simulation parameters are consistent with the ones mentioned in Chapter IV except third order dispersion coefficient β_3 is omitted. Of course, one can include β_3 which will lead to asymmetry in the output. But the crux of this simulation is including a higher order filter in a fiber laser cavity is shown in Figure 8.5. The simulated spectrum propagation throughout fiber laser cavity is shown in Figure 8.6(a)-(e).The simulated pulse propagation is shown in 8.7(a)-(e). It is apparent from the simulation that somehow pulses evolve into parabolic shape and the spectrum also becomes smooth and somewhat parabolic shape which is close to SS evolution. This is strikingly different than the CSHE behavior. It is conventional knowledge that to obtain SS operation in mode-locked fiber lasers, a sharp spectral filter is necessary. But this simulation predicts that there could be another way to facilitate SS pulse formation.

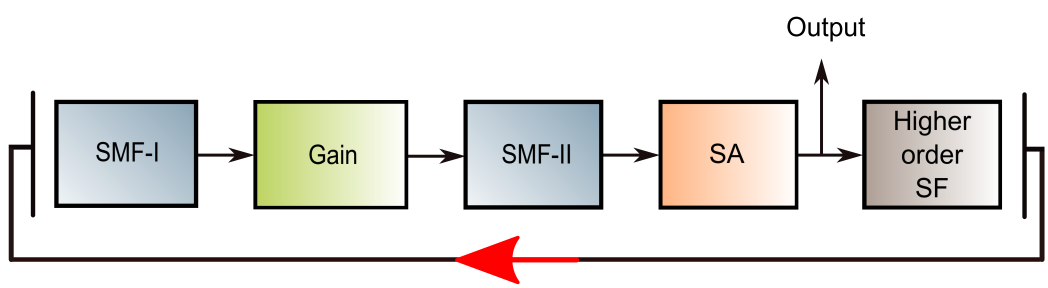

Figure 8.4: Conceptual schematic of the Yb doped fiber laser with a higher order spectral filter. SMF, single mode fiber; SA, saturable absorber; SF, spectral filter.

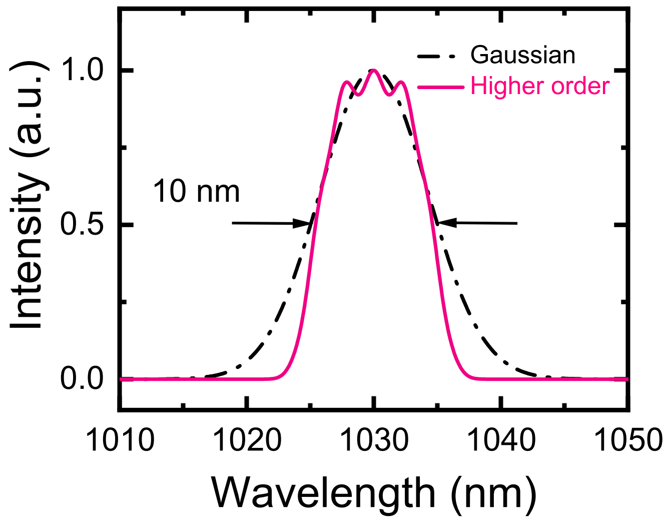

Figure 8.5: Higher order spectral filter transmission (pink curve) compared with a Gaussian spectral filter transmission (black curve) with approximately same FWHM.

In another effort, simulations are performed to observe the effect of much complicated spectral filter illustrated by Figure 8.8(a). The spectral and temporal output of this laser are presented in Figures 8.8(b) and 8.8(c), respectively. This result is greatly different than the one presented in Figures 8.6 and 8.7. The spectrum is very structured and it has cat ears like ANDi fiber laser spectrum. But the pulse is unlike ANDi fiber lasers. In fact, the pulse resembles the wide composite pulse solution of the Cubic Ginzberg Landau Equation (CGLE) [153].

In conclusion, this comprehensive study of effect of spectral filtering on mode-locked fiber oscillators and especially our recent work on CSHE will pioneer future ultrafast fiber laser research.

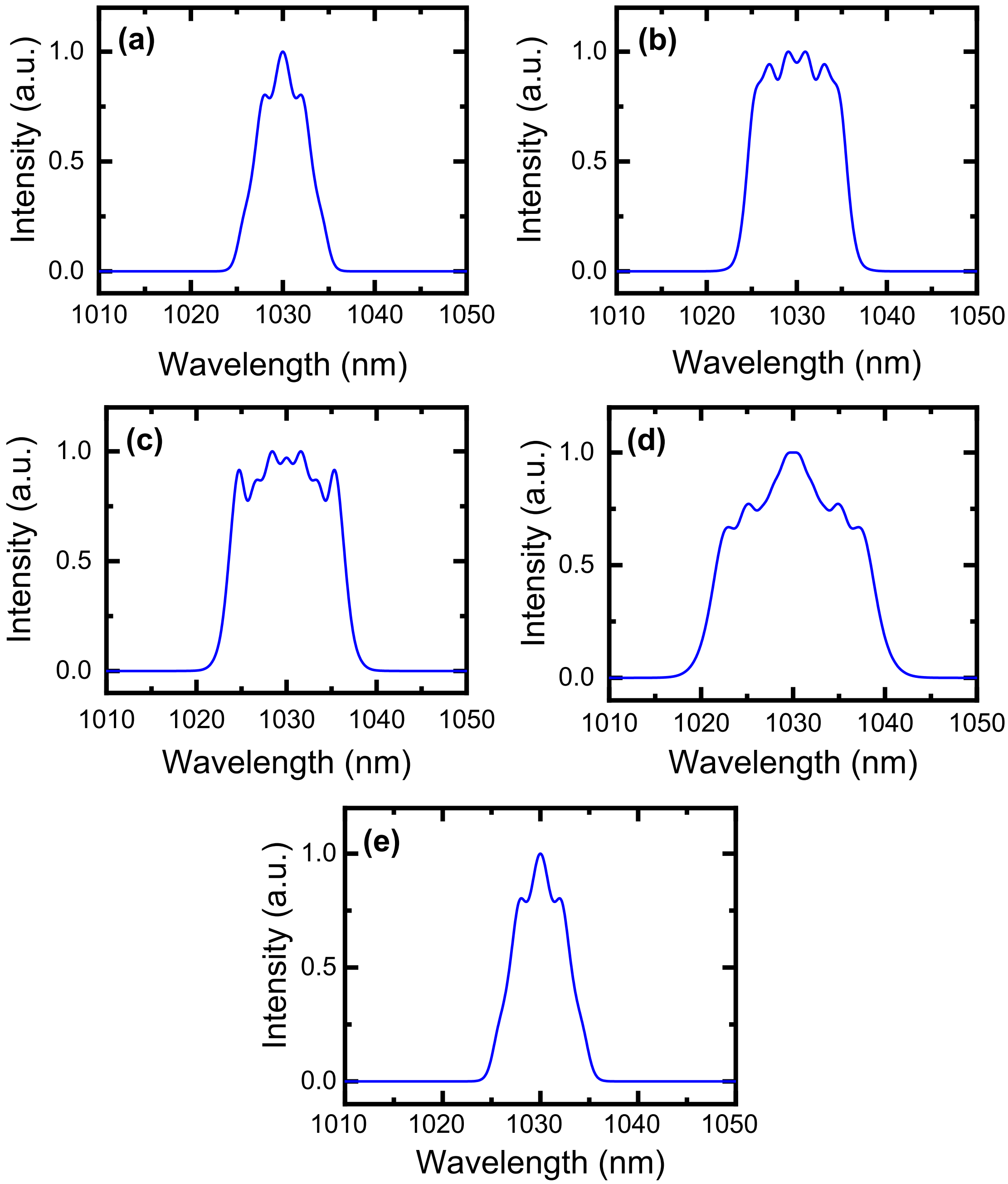

Figure 8.6: Simulated mode-locked spectra for a fiber laser with a three peak spectral filter transmission profile after (a) SMF-I (b) gain (c) SMF-II (d) SA (output) (e) SF.

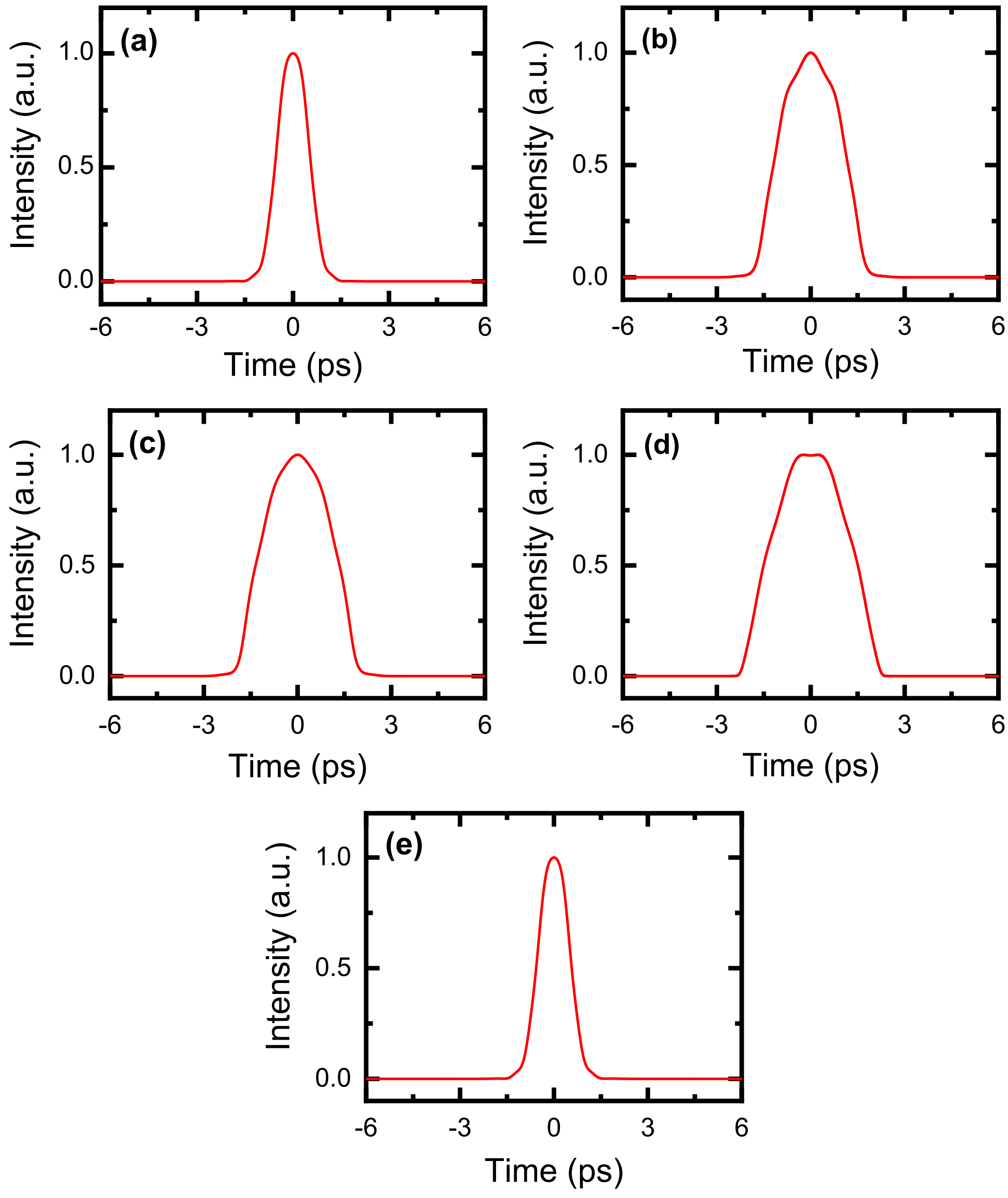

Figure 8.7: Simulated pulse for a fiber laser with a three peak spectral filter transmission profile after (a) SMF-I (b) gain (c) SMF-II (d) SA (output) (e) SF.

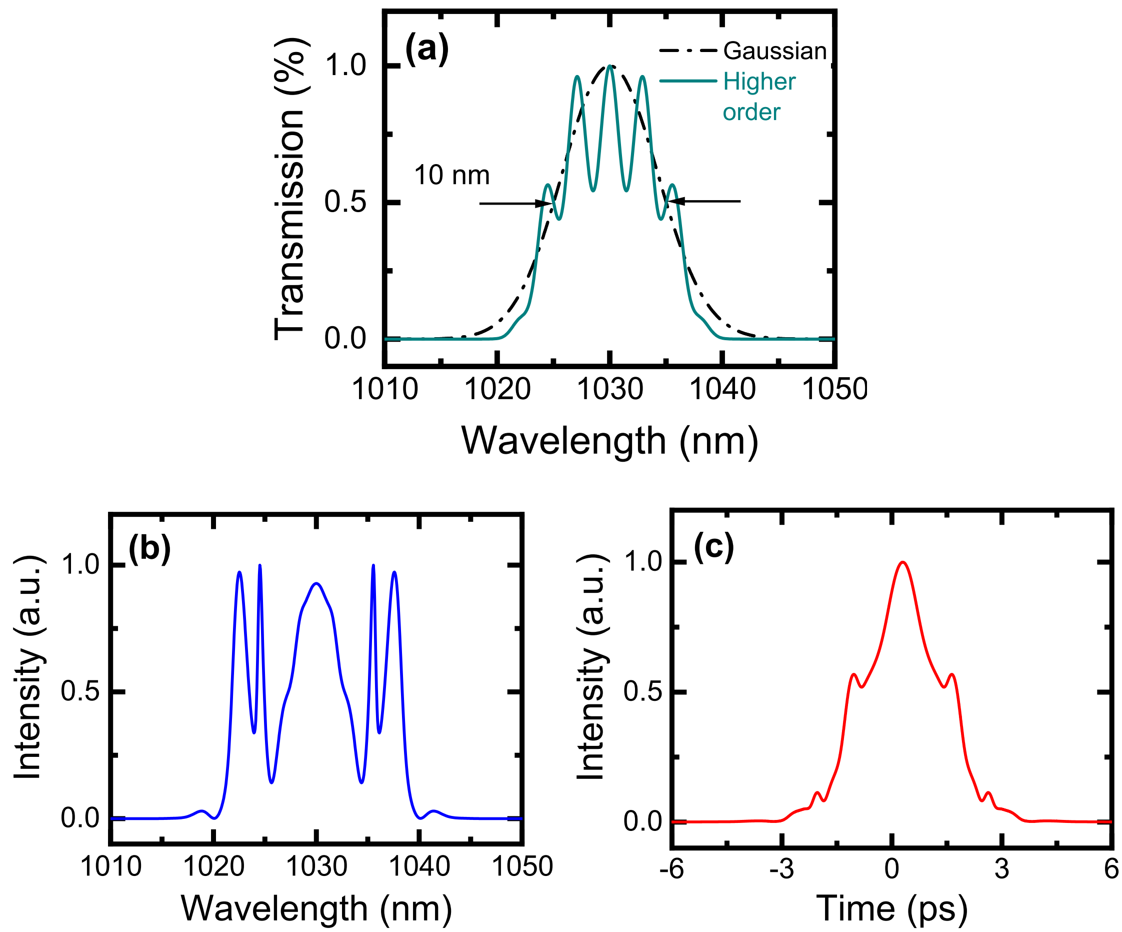

Figure 8.8: Simulation results for a fiber laser with (a) a complicated spectral filter transmission profile (b) output spectrum (c) output pulse.

[1] A. Khanolkar, X. Ge, and A. Chong, "All normal dispersion fiber laser with bandwidth tunable fiber based spectral filter," in *Conference on Lasers and Electro-Optics*. Optical Society of America, 2020, p. JW2E.27.

[2] A. Khanolkar, X. Ge, and A. Chong, "All-normal dispersion fiber laser with a bandwidth tunable fiber-based spectral filter," *Optics letters*, vol. 45, no. 16, pp. 4555–4558, 2020.

[3] A. Khanolkar and A. Chong, "Multipulsing states management in all-normal dispersion fiber laser with a fiber-based spectral filter," *Optics Letters*, vol. 45, no. 23, pp. 6374–6377, 2020.

[4] A. Khanolkar, Y. Zang, and A. Chong, "Complex swift hohenberg equation dissipative soliton fiber laser," *Photonics Research*, vol. 9, no. 6, pp. 1033–1038, 2021.

[5] A. Khanolkar, C. Ma, and A. Chong, "Generation of octave spanning spectra directly from a fiber oscillator with self-similar pulse evolution," in *CLEO: QELS_Fundamental Science*. Optical Society of America, 2018, pp. JTh2A–111.

[6] G. P. Agrawal, *Nonlinear Fiber Optics: Formerly Quantum Electronics*. Academic press, 2013.

[7] A. Hasegawa and F. Tappert, "Transmission of stationary nonlinear optical pulses in dispersive dielectric fibers. i. anomalous dispersion," *Applied Physics Letters*, vol. 23, no. 3, pp. 142–144, 1973.

[8] A. Shabat and V. Zakharov, "Exact theory of two-dimensional self-focusing and one-dimensional self-modulation of waves in nonlinear media," *Soviet physics JETP*, vol. 34, no. 1, p. 62, 1972.

[9] L. F. Mollenauer and R. H. Stolen, "The soliton laser," *Optics News*, vol. 10, no. 6, pp. 20_2–21, 1984.

[10] K. Tamura, E. Ippen, H. Haus, and L. Nelson, "77-fs pulse generation from a stretched-pulse mode-locked all-fiber ring laser," *Optics letters*, vol. 18, no. 13, pp. 1080–1082, 1993.

[11] D. Anderson, M. Desaix, M. Karlsson, M. Lisak, and M. Quiroga-Teixeiro, "Wave-breaking-free pulses in nonlinear-optical fibers," *JOSA B*, vol. 10, no. 7, pp. 1185–1190, 1993.

[12] K. Tamura and M. Nakazawa, "Pulse compression by nonlinear pulse evolution with reduced optical wave breaking in erbium-doped fiber amplifiers," *Optics letters*, vol. 21, no. 1, pp. 68–70, 1996.

[13] M. E. Fermann, V. Kruglov, B. Thomsen, J. M. Dudley, and J. D. Harvey, "Self-similar propagation and amplification of parabolic pulses in optical fibers," *Physical review letters*, vol. 84, no. 26, p. 6010, 2000.

[14] F. Ö. Ilday, J. Buckley, H. Lim, F. Wise, and W. Clark, "Generation of 50-fs, 5-nj pulses at 1.03 μm from a wave-breaking-free fiber laser," *Optics letters*, vol. 28, no. 15, pp. 1365–1367, 2003.

[15] B. Oktem, C. Ülgüdür, and F. Ö. Ilday, "Soliton–similariton fibre laser," *Nature Photonics*, vol. 4, no. 5, pp. 307–311, 2010.

[16] W. H. Renninger, A. Chong, and F. W. Wise, "Self-similar pulse evolution in an all-normal-dispersion laser," *Physical Review A*, vol. 82, no. 2, p. 021805, 2010.

[17] A. Chong, J. Buckley, W. Renninger, and F. Wise, "All-normal-dispersion femtosecond fiber laser," *Optics express*, vol. 14, no. 21, pp. 10 095–10 100, 2006.

[18] A. Chong, W. H. Renninger, and F. W. Wise, "All-normal-dispersion femtosecond fiber laser with pulse energy above 20nj," *Optics letters*, vol. 32, no. 16, pp. 2408–2410, 2007.

[19] Z. Liu, Z. M. Ziegler, L. G. Wright, and F. W. Wise, "Megawatt peak power from a mamyshev oscillator," *Optica*, vol. 4, no. 6, pp. 649–654, 2017.

[20] K. Regelskis, J. Želudevičius, K. Viskontas, and G. Račiukaitis, "Ytterbium-doped fiber ultrashort pulse generator based on self-phase modulation and alternating spectral filtering," *Optics letters*, vol. 40, no. 22, pp. 5255–5258, 2015.

[21] I. Samartsev, A. Bordenyuk, and V. Gapontsev, "Environmentally stable seed source for high power ultrafast laser," in *Components and Packaging for Laser Systems III*, vol. 10085. International Society for Optics and Photonics, 2017, p. 100850S.

[22] P. Mamyshev, "All-optical data regeneration based on self-phase modulation effect," in *24th European Conference on Optical Communication. ECOC'98 (IEEE Cat. No. 98TH8398)*, vol. 1. IEEE, 1998, pp. 475–476.

[23] B. Lyot, "Optical apparatus with wide field using interference of polarized light," *CR Acad. Sci.(Paris)*, vol. 197, no. 1593, 1933.

[24] A. A. Tovar and L. W. Casperson, "Generalized beam matrices: Gaussian beam propagation in misaligned complex optical systems," *JOSA A*, vol. 12, no. 7, pp. 1522–1533, 1995.

[25] L. G. Wright, D. N. Christodoulides, and F. W. Wise, "Spatiotemporal mode-locking in multimode fiber lasers," *Science*, vol. 358, no. 6359, pp. 94–97, 2017.

[26] E. Snitzer, H. Po, F. Hakimi, R. Tumminelli, and B. McCollum, "Double clad, offset core nd fiber laser," in *Optical fiber sensors*. Optical Society of America, 1988, p. PD5.

[27] Danielsoh8, "Schematic diagram of high power fiber laser using a double-clad fiber," https://commons.wikimedia.org/wiki/File:Schematic_diagram_of_high_power_fiber_laser_using_a_double-clad_fiber.svg.

[28] P. Russell, "Photonic crystal fibers," *science*, vol. 299, no. 5605, pp. 358–362, 2003.

[29] ALPhANOV, "Photonic crystal fiber interfacing," https://www.alphanov.com/en/products-services/photonic-crystal-fiber-interfacing.

[30] D. R. Paschotta, "Photonic crystal fibers," https://www.rp-photonics.com/photonic_crystal_fibers.html.

[31] X. Zhu and N. Peyghambarian, "High-power zblan glass fiber lasers: review and prospect," *Advances in OptoElectronics*, vol. 2010, 2010.

[32] F. Théberge, J.-F. Daigle, D. Vincent, P. Mathieu, J. Fortin, B. E. Schmidt, N. Thiré, and F. Légaré, "Mid-infrared supercontinuum generation in fluoroindate fiber," *Optics letters*, vol. 38, no. 22, pp. 4683–4685, 2013.

[33] J. Swiderski, M. Michalska, and G. Maze, "Mid-ir supercontinuum generation in a zblan fiber pumped by a gain-switched mode-locked tm-doped fiber laser and amplifier system," *Optics express*, vol. 21, no. 7, pp. 7851–7857, 2013.

[34] A. Chong, W. H. Renninger, and F. W. Wise, "Properties of normal-dispersion femtosecond fiber lasers," *JOSA B*, vol. 25, no. 2, pp. 140–148, 2008.

[35] W. Renninger, A. Chong, and F. Wise, "Dissipative solitons in normal-dispersion fiber lasers," *Physical Review A*, vol. 77, no. 2, p. 023814, 2008.

[36] O. Prochnow, A. Ruehl, M. Schultz, D. Wandt, and D. Kracht, "All-fiber similariton laser at 1 μm without dispersion compensation," *Optics express*, vol. 15, no. 11, pp. 6889–6893, 2007.

[37] C. K. Nielsen and S. R. Keiding, "All-fiber mode-locked fiber laser," *Optics letters*, vol. 32, no. 11, pp. 1474–1476, 2007.

[38] K. Kieu and F. Wise, "All-fiber normal-dispersion femtosecond laser," *Optics express*, vol. 16, no. 15, pp. 11 453–11 458, 2008.

[39] M. Schultz, H. Karow, O. Prochnow, D. Wandt, U. Morgner, and D. Kracht, "All-fiber ytterbium femtosecond laser without dispersion compensation," *Optics express*, vol. 16, no. 24, pp. 19 562–19 567, 2008.

[40] J. Fekete, A. Cserteg, and R. Szipőcs, "All-fiber, all-normal dispersion ytterbium ring oscillator," *Laser Physics Letters*, vol. 6, no. 1, p. 49, 2008.

[41] K. Özgören and F. Ö. İlday, "All-fiber all-normal dispersion laser with a fiber-based lyot filter," *Optics letters*, vol. 35, no. 8, pp. 1296–1298, 2010.

[42] Y. Fedotov, S. Kobtsev, R. Arif, A. Rozhin, C. Mou, and S. Turitsyn, “Spectrum-, pulsewidth-, and wavelength-switchable all-fiber mode-locked yb laser with fiber based birefringent filter,” *Optics express*, vol. 20, no. 16, pp. 17 797–17 805, 2012.

[43] Y. S. Fedotov, S. M. Kobtsev, A. G. Rozhin, S. K. Turitsyn, and C. Mou, “Spectral width and pulse duration tuning in yb+ mode-locked fiber laser with birefringent lyot filter.” in *Advanced Photonics Congress*. Optical Society of America, 2012, p. JM5A.25. [Online]. Available: http://www.osapublishing.org/abstract.cfm?URI=ANIC-2012-JM5A.25

[44] Z. Wang, L. Zhan, X. Fang, and H. Luo, “Spectral filtering effect on mode-locking regimes transition: similariton-dissipative soliton fiber laser,” *JOSA B*, vol. 34, no. 11, pp. 2325–2333, 2017.

[45] R. Ulrich and A. Simon, “Polarization optics of twisted single-mode fibers,” *Applied optics*, vol. 18, no. 13, pp. 2241–2251, 1979.

[46] A. Yariv and P. Yeh, *Optical waves in crystals*. Wiley New York, 1984, vol. 5.

[47] J. Szczepanek, T. M. Kardaś, C. Radzewicz, and Y. Stepanenko, “Nonlinear polarization evolution of ultrashort pulses in polarization maintaining fibers,” *Optics express*, vol. 26, no. 10, pp. 13 590–13 604, 2018.

[48] J. Berthold III and L. Thompson, “Thermal dependence of stress-induced birefringence in single mode optical fibers,” in *Fiber optic and laser sensors II*, vol. 478. International Society for Optics and Photonics, 1984, pp. 63–67.

[49] D.-H. Kim and J. U. Kang, “Analysis of temperature-dependent birefringence of a polarization-maintaining photonic crystal fiber,” *Optical Engineering*, vol. 46, no. 7, p. 075003, 2007.

[50] N. Boudrioua, A. Boudrioua, F. Monteiro, E. Losson, A. Dandache, and R. Kremer, “Analysis of polarization mode dispersion fluctuations in single mode fibres due to temperature,” *Optics communications*, vol. 281, no. 19, pp. 4870–4875, 2008.

[51] P. Ma, N. Song, J. Jin, J. Song, and X. Xu, “Birefringence sensitivity to temperature of polarization maintaining photonic crystal fibers,” *Optics & Laser Technology*, vol. 44, no. 6, pp. 1829–1833, 2012.

[52] N. Akhmediev and A. Ankiewicz, “Multi-soliton complexes,” *Chaos: An Interdisciplinary Journal of Nonlinear Science*, vol. 10, no. 3, pp. 600–612, 2000.

[53] A. MARECZKO, C. Vincent, A. COURJAUD, C. Patrice, J.-L. DOUALAN, R. MONCORGE, and E. MOTTAY, “100mj level yb: Caf2 regenerative amplifier for multipulse femtosecond regime,” in *Advanced Solid State Lasers*. Optical Society of America, 2013, pp. ATu3A–47.

[54] A. Grudinin, D. Richardson, and D. Payne, "Energy quantisation in figure eight fibre laser," *Electronics Letters*, vol. 28, no. 1, pp. 67–68, 1992.

[55] D. Tang, W. Man, and H. Tam, "Stimulated soliton pulse formation and its mechanism in a passively mode-locked fibre soliton laser," *Optics communications*, vol. 165, no. 4-6, pp. 189–194, 1999.

[56] B. Zhao, D. Tang, P. Shum, Y. Gong, C. Lu, W. Man, and H. Tam, "Energy quantization of twin-pulse solitons in a passively mode-locked fiber ring laser," *Applied physics B*, vol. 77, no. 6-7, pp. 585–588, 2003.

[57] D. Tang, L.-M. Zhao, B. Zhao, and A. Liu, "Mechanism of multisoliton formation and soliton energy quantization in passively mode-locked fiber lasers," *Physical Review A*, vol. 72, no. 4, p. 043816, 2005.

[58] N. Akhmediev, J. M. Soto-Crespo, M. Grapinet, and P. Grelu, "Dissipative soliton pulsations with periods beyond the laser cavity round trip time," *Journal of Nonlinear Optical Physics & Materials*, vol. 14, no. 02, pp. 177–194, 2005.

[59] P. Grelu, F. Belhache, F. Gutty, and J. M. Soto-Crespo, "Relative phase locking of pulses in a passively mode-locked fiber laser," *JOSA B*, vol. 20, no. 5, pp. 863–870, 2003.

[60] B. Ortaç, A. Hideur, M. Brunel, C. Chédot, J. Limpert, A. Tünnermann, and F. Ilday, "Generation of parabolic bound pulses from a yb-fiber laser," *Optics Express*, vol. 14, no. 13, pp. 6075–6083, 2006.

[61] J. Peng, L. Zhan, S. Luo, and Q. S. Shen, "Generation of soliton molecules in a normal-dispersion fiber laser," *IEEE Photonics Technology Letters*, vol. 25, no. 10, pp. 948–951, 2013.

[62] C. Bao, X. Xiao, and C. Yang, "Soliton rains in a normal dispersion fiber laser with dual-filter," *Optics letters*, vol. 38, no. 11, pp. 1875–1877, 2013.

[63] S. Huang, Y. Wang, Y. Peiguang, G. Zhang, J. Zhao, H. Li, R. Lin, G. Cao, and J. Duan, "Observation of multipulse bunches in a graphene oxide passively mode-locked ytterbium-doped fiber laser with all-normal dispersion," *Applied Physics B*, vol. 116, no. 4, pp. 939–946, 2014.

[64] J. M. Soto-Crespo and N. Akhmediev, "Composite solitons and two-pulse generation in passively mode-locked lasers modeled by the complex quintic swift-hohenberg equation," *Physical Review E*, vol. 66, no. 6, p. 066610, 2002.

[65] A. Komarov, K. Komarov, H. Leblond, and F. Sanchez, "Spectral-selective management of dissipative solitons in passive mode-locked fibre lasers," *Journal of Optics A: Pure and Applied Optics*, vol. 9, no. 12, p. 1149, 2007.

[66] A. Haboucha, A. Komarov, H. Leblond, F. Sanchez, and G. Martel, "Mechanism of multiple pulse formation in the normal dispersion regime of passively mode-locked fiber ring lasers," *Optical Fiber Technology*, vol. 14, no. 4, pp. 262–267, 2008.

[67] H. A. Haus, "Theory of mode locking with a fast saturable absorber," *Journal of Applied Physics*, vol. 46, no. 7, pp. 3049–3058, 1975.

[68] N. Akhmediev and A. Ankiewicz, *Dissipative solitons: from optics to biology and medicine*. Springer Science & Business Media, 2008, vol. 751.

[69] W. Firth and A. Scroggie, "Optical bullet holes: robust controllable localized states of a nonlinear cavity," *Physical review letters*, vol. 76, no. 10, p. 1623, 1996.

[70] J. Lega, J. V. Moloney, and A. C. Newell, "Swift-hohenberg equation for lasers," *Physical review letters*, vol. 73, no. 22, p. 2978, 1994.

[71] K. Staliūnas, G. Šlekys, and C. Weiss, "Nonlinear pattern formation in active optical systems: shocks, domains of tilted waves, and cross-roll patterns," *Physical review letters*, vol. 79, no. 14, p. 2658, 1997.

[72] J.-F. Mercier and J. V. Moloney, "Derivation of semiconductor laser mean-field and swift-hohenberg equations," *Physical Review E*, vol. 66, no. 3, p. 036221, 2002.

[73] E. P. Ippen, "Principles of passive mode locking," *Applied Physics B*, vol. 58, no. 3, pp. 159–170, 1994.

[74] K.-i. Maruno, A. Ankiewicz, and N. Akhmediev, "Exact soliton solutions of the one-dimensional complex swift–hohenberg equation," *Physica D: Nonlinear Phenomena*, vol. 176, no. 1-2, pp. 44–66, 2003.

[75] H. Wang and L. Yanti, "An efficient numerical method for the quintic complex swift-hohenberg equation," *Numerical Mathematics: Theory, Methods and Applications*, vol. 4, no. 2, pp. 237–254, 2011.

[76] S. Latas, "High-energy plain and composite pulses in a laser modeled by the complex swift–hohenberg equation," *Photonics Research*, vol. 4, no. 2, pp. 49–52, 2016.

[77] S. Latas, M. Ferreira, and M. Facão, "Swift–hohenberg soliton explosions," *JOSA B*, vol. 35, no. 9, pp. 2266–2271, 2018.

[78] L. Zhao, D. Li, L. Li, X. Wang, Y. Geng, D. Shen, and L. Su, "Route to larger pulse energy in ultrafast fiber lasers," *IEEE Journal of Selected Topics in Quantum Electronics*, vol. 24, no. 3, pp. 1–9, 2017.

[79] C. Bao, W. Chang, C. Yang, N. Akhmediev, and S. T. Cundiff, "Observation of coexisting dissipative solitons in a mode-locked fiber laser," *Physical review letters*, vol. 115, no. 25, p. 253903, 2015.

[80] Y. Zhou, W. Lin, H. Cheng, W. Wang, T. Qiao, Q. Qian, S. Xu, and Z. Yang, "Composite filtering effect in a sesam mode-locked fiber laser with a 3.2-ghz fundamental repetition rate: switchable states from single soliton to pulse bunch," *Optics express*, vol. 26, no. 8, pp. 10 842–10 857, 2018.

[81] A. Chong, W. H. Renninger, and F. W. Wise, "Route to the minimum pulse duration in normal-dispersion fiber lasers," *Optics letters*, vol. 33, no. 22, pp. 2638–2640, 2008.

[82] X. Wang, Y.-g. Liu, Z. Wang, Z. Wang, and G. Yang, "L-band efficient dissipative soliton erbium-doped fiber laser with a pulse energy of 6.15 nj and 3 db bandwidth of 47.8 nm," *Journal of Lightwave Technology*, vol. 37, no. 4, pp. 1168–1173, 2019.

[83] J. Zhou, W. Qi, W. Pan, and Y. Feng, "Dissipative soliton generation from a large anomalous dispersion ytterbium-doped fiber laser," *Optics Letters*, vol. 45, no. 20, pp. 5768–5771, 2020.

[84] D. Li, H. Jussila, Y. Wang, G. Hu, T. Albrow-Owen, R. C. Howe, Z. Ren, J. Bai, T. Hasan, and Z. Sun, "Wavelength and pulse duration tunable ultrafast fiber laser mode-locked with carbon nanotubes," *Scientific reports*, vol. 8, no. 1, pp. 1–8, 2018.

[85] A. O'Keefe and D. A. Deacon, "Cavity ring-down optical spectrometer for absorption measurements using pulsed laser sources," *Review of scientific instruments*, vol. 59, no. 12, pp. 2544–2551, 1988.

[86] R. Swofford and A. Albrecht, "Nonlinear spectroscopy," *Annual Review of Physical Chemistry*, vol. 29, no. 1, pp. 421–440, 1978.

[87] Z. Sun, D. Popa, T. Hasan, F. Torrisi, F. Wang, E. J. Kelleher, J. C. Travers, V. Nicolosi, and A. C. Ferrari, "A stable, wideband tunable, near transform-limited, graphene-mode-locked, ultrafast laser," *Nano Research*, vol. 3, no. 9, pp. 653–660, 2010.

[88] Y. Nakazaki and S. Yamashita, "Fast and wide tuning range wavelength-swept fiber laser based on dispersion tuning and its application to dynamic fbg sensing," *Optics express*, vol. 17, no. 10, pp. 8310–8318, 2009.

[89] Y. Liu, H. Tu, W. A. Benalcazar, E. J. Chaney, and S. A. Boppart, "Multimodal nonlinear microscopy by shaping a fiber supercontinuum from 900 to 1160 nm," *IEEE Journal of Selected Topics in Quantum Electronics*, vol. 18, no. 3, pp. 1209–1214, 2011.

[90] W. Liu, S.-H. Chia, H.-Y. Chung, R. Greinert, F. X. Kärtner, and G. Chang, "Energetic ultrafast fiber laser sources tunable in 1030–1215 nm for deep tissue multi-photon microscopy," *Optics express*, vol. 25, no. 6, pp. 6822–6831, 2017.

[91] P. Taroni, A. Bassi, D. Comelli, A. Farina, R. Cubeddu, and A. Pifferi, "Diffuse optical spectroscopy of breast tissue extended to 1100 nm," *Journal of biomedical optics*, vol. 14, no. 5, p. 054030, 2009.

[92] O. Okhotnikov, L. Gomes, N. Xiang, T. Jouhti, and A. Grudinin, “Mode-locked ytterbium fiber laser tunable in the 980–1070-nm spectral range,” *Optics letters*, vol. 28, no. 17, pp. 1522–1524, 2003.

[93] L. Kong, X. Xiao, and C. Yang, “Tunable all-normal-dispersion yb-doped mode-locked fiber lasers,” *Laser physics*, vol. 20, no. 4, pp. 834–837, 2010.

[94] C. Ouyang, P. Shum, H. Wang, S. Fu, X. Cheng, J. H. Wong, and X. Tian, “Wavelength-tunable high-energy all-normal-dispersion yb-doped mode-locked all-fiber laser with a hibi fiber sagnac loop filter,” *IEEE Journal of Quantum Electronics*, vol. 47, no. 2, pp. 198–203, 2011.

[95] M. Schultz, H. Karow, D. Wandt, U. Morgner, and D. Kracht, “Ytterbium femtosecond fiber laser without dispersion compensation tunable from 1015 nm to 1050 nm,” *Optics communications*, vol. 282, no. 13, pp. 2567–2570, 2009.

[96] C. Aguergaray, D. Méchin, V. Kruglov, and J. D. Harvey, “Experimental realization of a mode-locked parabolic raman fiber oscillator,” *Optics express*, vol. 18, no. 8, pp. 8680–8687, 2010.

[97] B. Nie, D. Pestov, F. W. Wise, and M. Dantus, “Generation of 42-fs and 10-nj pulses from a fiber laser with self-similar evolution in the gain segment,” *Optics express*, vol. 19, no. 13, pp. 12 074–12 080, 2011.

[98] B. G. Bale and S. Wabnitz, “Strong spectral filtering for a mode-locked similariton fiber laser,” *Optics letters*, vol. 35, no. 14, pp. 2466–2468, 2010.

[99] D. A. Grukh, A. S. Kurkov, V. M. Paramonov, and E. M. Dianov, “Effect of heating on the optical properties of yb3+-doped fibres and fibre lasers,” *Quantum Electronics*, vol. 34, no. 6, p. 579, 2004.

[100] A. Kurkov, V. Paramonov, and O. Medvedkov, “Ytterbium fiber laser emitting at 1160 nm,” *Laser Physics Letters*, vol. 3, no. 10, p. 503, 2006.

[101] M. P. Kalita, S.-u. Alam, C. Codemard, S. Yoo, A. J. Boyland, M. Ibsen, and J. K. Sahu, “Multi-watts narrow-linewidth all fiber yb-doped laser operating at 1179 nm,” *Optics express*, vol. 18, no. 6, pp. 5920–5925, 2010.

[102] L. Huang, H. Zhang, X. Wang, and P. Zhou, “Diode-pumped 1178-nm high-power yb-doped fiber laser operating at 125$\circ$ c,” *IEEE Photonics Journal*, vol. 8, no. 3, pp. 1–7, 2016.

[103] F. Calegari, G. Sansone, S. Stagira, C. Vozzi, and M. Nisoli, “Advances in attosecond science,” *Journal of Physics B: Atomic, Molecular and Optical Physics*, vol. 49, no. 6, p. 062001, 2016.

[104] M. Hentschel, R. Kienberger, C. Spielmann, G. A. Reider, N. Milosevic, T. Brabec, P. Corkum, U. Heinzmann, M. Drescher, and F. Krausz, "Attosecond metrology," *Nature*, vol. 414, no. 6863, pp. 509–513, 2001.

[105] P. Villoresi, P. Ceccherini, L. Poletto, G. Tondello, C. Altucci, R. Bruzzese, C. De Lisio, M. Nisoli, S. Stagira, G. Cerullo *et al.*, "Spectral features and modeling of high-order harmonics generated by sub-10-fs pulses," *Physical review letters*, vol. 85, no. 12, p. 2494, 2000.

[106] C. Spielmann, N. Burnett, S. Sartania, R. Koppitsch, M. Schnürer, C. Kan, M. Lenzner, P. Wobrauschek, and F. Krausz, "Generation of coherent x-rays in the water window using 5-femtosecond laser pulses," *Science*, vol. 278, no. 5338, pp. 661–664, 1997.

[107] U. Morgner, F. X. Kärtner, S.-H. Cho, Y. Chen, H. A. Haus, J. G. Fujimoto, E. P. Ippen, V. Scheuer, G. Angelow, and T. Tschudi, "Sub-two-cycle pulses from a kerr-lens mode-locked ti: sapphire laser," *Optics letters*, vol. 24, no. 6, pp. 411–413, 1999.

[108] D. H. Sutter, G. Steinmeyer, L. Gallmann, N. Matuschek, F. Morier-Genoud, U. Keller, V. Scheuer, G. Angelow, and T. Tschudi, "Semiconductor saturable-absorber mirror–assisted kerr-lens mode-locked ti: sapphire laser producing pulses in the two-cycle regime," *Optics letters*, vol. 24, no. 9, pp. 631–633, 1999.

[109] R. Ell, U. Morgner, F. X. Kärtner, J. G. Fujimoto, E. P. Ippen, V. Scheuer, G. Angelow, T. Tschudi, M. J. Lederer, A. Boiko *et al.*, "Generation of 5-fs pulses and octave-spanning spectra directly from a ti: sapphire laser," *Optics letters*, vol. 26, no. 6, pp. 373–375, 2001.

[110] W. Tomlinson, R. Stolen, and C. Shank, "Compression of optical pulses chirped by self-phase modulation in fibers," *JOSA B*, vol. 1, no. 2, pp. 139–149, 1984.

[111] R. L. Fork, C. B. Cruz, P. Becker, and C. V. Shank, "Compression of optical pulses to six femtoseconds by using cubic phase compensation," *Optics letters*, vol. 12, no. 7, pp. 483–485, 1987.

[112] M. Nisoli, S. De Silvestri, O. Svelto, R. Szipöcs, K. Ferencz, C. Spielmann, S. Sartania, and F. Krausz, "Compression of high-energy laser pulses below 5 fs," *Optics letters*, vol. 22, no. 8, pp. 522–524, 1997.

[113] G. Krauss, S. Lohss, T. Hanke, A. Sell, S. Eggert, R. Huber, and A. Leitenstorfer, "Synthesis of a single cycle of light with compact erbium-doped fibre technology," *Nature photonics*, vol. 4, no. 1, pp. 33–36, 2010.

[114] A. Chong, L. G. Wright, and F. W. Wise, "Ultrafast fiber lasers based on self-similar pulse evolution: a review of current progress," *Reports on Progress in Physics*, vol. 78, no. 11, p. 113901, 2015.

[115] A. Chong, H. Liu, B. Nie, B. Bale, S. Wabnitz, W. Renninger, M. Dantus, and F. Wise, "Pulse generation without gain-bandwidth limitation in a laser with self-similar evolution," *Optics express*, vol. 20, no. 13, pp. 14 213–14 220, 2012.

[116] S. Pitois, C. Finot, L. Provost, and D. J. Richardson, "Generation of localized pulses from incoherent wave in optical fiber lines made of concatenated mamyshev regenerators," *JOSA B*, vol. 25, no. 9, pp. 1537–1547, 2008.

[117] W. Liu, R. Liao, J. Zhao, J. Cui, Y. Song, C. Wang, and M. Hu, "Femtosecond mamyshev oscillator with 10-mw-level peak power," *Optica*, vol. 6, no. 2, pp. 194–197, 2019.

[118] C. Ma, A. Khanolkar, Y. Zang, and A. Chong, "Ultrabroadband, few-cycle pulses directly from a mamyshev fiber oscillator," *Photonics Research*, vol. 8, no. 1, pp. 65–69, 2020.

[119] M. Jansen, B. D. Cantos, G. P. Carey, R. Dato, G. Giaretta, S. Hallstein, W. R. Hitchens, D. Lee, A. Mooradian, R. F. Nabiev *et al.*, "Visible laser and laser array sources for projection displays," in *Liquid Crystal Materials, Devices, and Applications XI*, vol. 6135. International Society for Optics and Photonics, 2006, p. 61350T.

[120] Y. Hirano, "Highly efficient, compact green laser for laser tv," in *LASE, Part of SPIE Phonotics West 2009 San Jose Convention center, San Jose, CA, USA*, 2009.

[121] S. E. Ltd, "Ipg lasers feature in nec's digital cinema projector," https://optics.org/news/7/4/22.

[122] A. Francis, *Ophthalmic lasers: photocoagulation, photoradiation, and surgery.* Mosby, 1983.

[123] W. Koechner, *Solid-state laser engineering.* Springer, 2013, vol. 1.

[124] G. McConnell, "Confocal laser scanning fluorescence microscopy with a visible continuum source," *Optics Express*, vol. 12, no. 13, pp. 2844–2850, 2004.

[125] D. A. Shea and M. D. Morris, "Bone tissue fluorescence reduction for visible laser raman spectroscopy," *Applied spectroscopy*, vol. 56, no. 2, pp. 182–186, 2002.

[126] W. B. Bridges, "Ion lasers-the early years," *IEEE Journal of Selected Topics in Quantum Electronics*, vol. 6, no. 6, pp. 885–898, 2000.

[127] W. Long Jr, "Plummer mj, stappaerts ea," *Appl. Phys. Lett*, vol. 43, p. 735, 1983.

[128] J. Rigden, A. White, and E. Gordon, "Nerem, boston, mass.. nov. 6, 1962," in *Proc. Inst. Radio Engrs*, vol. 50, 1962, p. 1697.

[129] W. Silfvast, "New cw metal-vapor laser transitions in cd, sn, and zn," *Applied Physics Letters*, vol. 15, no. 1, pp. 23–25, 1969.

[130] D. N. Astadjov, K. D. Dimitrov, D. R. Jones, V. K. Kirkov, C. E. Little, N. V. Sabotinov, and N. K. Vuchkov, "Copper bromide laser of 120-w average output power," *IEEE Journal of Quantum Electronics*, vol. 33, no. 5, pp. 705–709, 1997.

[131] M. J. Weber, *CRC handbook of laser science and Technology supplement 2: optical materials.* CRC press, 2020.

[132] A. Dienes, "Mode-locked cw dye lasers," *Opto-electronics*, vol. 6, no. 1, pp. 99–113, 1974.

[133] J. Sutherland, P. French, J. Taylor, and B. Chai, "Visible continuous-wave laser transitions in pr 3+: Ylf and femtosecond pulse generation," *Optics letters*, vol. 21, no. 11, pp. 797–799, 1996.

[134] E. Granados, D. J. Spence, and R. P. Mildren, "Deep ultraviolet diamond raman laser," *Optics express*, vol. 19, no. 11, pp. 10 857–10 863, 2011.

[135] Y. Fujimoto, O. Ishii, and M. Yamazaki, "Multi-colour laser oscillation in pr3+-doped fluoro-aluminate glass fibre pumped by 442.6 nm gan-semiconductor laser," *Electronics Letters*, vol. 45, no. 25, pp. 1301–1302, 2009.

[136] M. Poulain, M. Poulain, and J. Lucas, "Verres fluores au tetrafluorure de zirconium proprietes optiques d'un verre dope au nd3+," *Materials Research Bulletin*, vol. 10, no. 4, pp. 243–246, 1975.

[137] H. Okamoto, K. Kasuga, I. Hara, and Y. Kubota, "Visible–nir tunable pr 3+-doped fiber laser pumped by a gan laser diode," *Optics Express*, vol. 17, no. 22, pp. 20 227–20 232, 2009.

[138] J. Nakanishi, T. Yamada, Y. Fujimoto, O. Ishii, and M. Yamazaki, "High-power red laser oscillation of 311.4 mw in pr3+-doped waterproof fluoro-aluminate glass fibre excited by gan laser diode," *Electronics Letters*, vol. 46, no. 18, pp. 1285–1286, 2010.

[139] J. Nakanishi, T. Yamada, Y. Fujitomo, O. Ishii, and M. Yamazaki, "Sub-watt output power at 638nm in wavelength by direct oscillation with pr-doped waterproof fluoro-aluminate glass fiber laser," in *The European Conference on Lasers and Electro-Optics.* Optical Society of America, 2011, p. CJ_P6.

[140] J. Nakanishi, Y. Horiuchi, T. Yamada, O. Ishii, M. Yamazaki, M. Yoshida, and Y. Fujimoto, "High-power direct green laser oscillation of 598 mw in pr 3+-doped waterproof fluoroaluminate glass fiber excited by two-polarization-combined gan laser diodes," *Optics letters*, vol. 36, no. 10, pp. 1836–1838, 2011.

[141] J. Nakanishi, T. Yamada, Y. Fujitomo, O. Ishii, and M. Yamazaki, "Watt-order output power at 638 nm in wavelength by direct oscillation with pr-doped fiber laser," in *2012 Conference on Lasers and Electro-Optics (CLEO).* IEEE, 2012, pp. 1–2.

[142] J. Nakanishi, T. Yamada, M. Murakami, Y. Fujimoto, O. Ishii, and M. Yamazaki, "Watt-order direct green laser oscillation at 522nm in pr3+-doped waterproof fluoro-aluminate-glass fiber," in *CLEO: Science and Innovations*. Optical Society of America, 2013, pp. JTu4A–02.

[143] S. Kajikawa, T. Terao, M. Yoshida, S. Motokoshi, O. Ishii, M. Yamazaki, and Y. Fujimoto, "Single-mode visible laser oscillation in pr-doped double-clad structured waterproof fluoro-aluminate glass fibre," *Electronics Letters*, vol. 52, no. 10, pp. 861–863, 2016.

[144] S. Kajikawa, M. Yoshida, S. Motokoshi, O. Ishii, M. Yamazaki, and Y. Fujimoto, "Visible ns-pulse laser oscillation in pr-doped double-clad structured waterproof fluoride glass fibre with sesam," *The Journal of Engineering*, vol. 2017, no. 7, pp. 407–409, 2017.

[145] D. Wu, J. Peng, Y. Zhong, Y. Cheng, B. Qu, J. Weng, Z. Luo, B. Xu, N. Chen, H. Xu *et al.*, "2-d materials-based passively q-switched 635 nm pr3+-doped zblan fiber lasers," in *Advanced Solid State Lasers*. Optical Society of America, 2015, pp. ATu2A–28.

[146] W. Li, C. Zhu, X. Rong, J. Wu, H. Xu, F. Wang, Z. Luo, and Z. Cai, "Bidirectional red-light passively q-switched all-fiber ring lasers with carbon nanotube saturable absorber," *Journal of Lightwave Technology*, vol. 36, no. 13, pp. 2694–2701, 2017.

[147] D. Wu, C. Quan, Z. Guo, Z. Cai, and H. Xu, "Self q-switched mode-locking in compact red pr3+-doped zblan fiber laser," *Journal of Optics*, vol. 20, no. 8, p. 085501, 2018.

[148] H. Okamoto, K. Kasuga, I. Hara, and Y. Kubota, "Over-10 mw broadband pr3+: Zblan-fibre light source at 635 nm pumped by gan ld," *Electronics Letters*, vol. 44, no. 23, pp. 1346–1347, 2008.

[149] M. Horowitz, Y. Barad, and Y. Silberberg, "Noiselike pulses with a broadband spectrum generated from an erbium-doped fiber laser," *Optics letters*, vol. 22, no. 11, pp. 799–801, 1997.

[150] X. Luo, T. H. Tuan, T. S. Saini, H. P. T. Nguyen, T. Suzuki, and Y. Ohishi, "All-fiber supercontinuum source pumped by noise-like pulse mode locked laser," *IEEE Photonics Technology Letters*, vol. 31, no. 15, pp. 1225–1228, 2019.

[151] M. Horowitz and Y. Silberberg, "Control of noiselike pulse generation in erbium-doped fiber lasers," *IEEE Photonics Technology Letters*, vol. 10, no. 10, pp. 1389–1391, 1998.

[152] C. Kong, C. Pilger, H. Hachmeister, X. Wei, T. H. Cheung, C. S. Lai, T. Huser, K. K. Tsia, and K. K. Wong, "Compact fs ytterbium fiber laser at 1010 nm for biomedical applications," *Biomedical optics express*, vol. 8, no. 11, pp. 4921–4932, 2017.

[153] N. Akhmediev, A. S. Rodrigues, and G. E. Town, “Interaction of dual-frequency pulses in passively mode-locked lasers,” *Optics communications*, vol. 187, no. 4-6, pp. 419–426, 2001.

APPENDIX A

Nonlinearity and Dispersion Parameter Calculation for Photonic Crystal Fiber

The nonlinearity coefficient γ is defined by

$$\gamma = \frac{n_2 \omega}{c A_e f f} \tag{A.1}$$

where, n_2 is the nonlinear refractive index, ω is the center frequency, c is the velocity of the light and A_{eff} is the effective area of the fiber which is given by

$$A_{eff} = \pi \omega_0^2 \tag{A.2}$$

where, ω_0 is the approximate fiber diameter.

- The photonic crystal fiber (PCF) used in this dissertation is assumed to have approximate diameter of 2.114 μm which gives A_{eff}= 3.51 μm^2. n_2 is 2.3 $\times$ 10^8 μm^2/W for silica fibers and ω corresponds to 1030 nm of central wavelength. By substituting all these values in Equation A.1, γ becomes 0.0405 W$^{-1}m^{-1}$
- For a standad SMF fiber at 1 μm such as 1060-XP has a cored diameter of approximately 6 μm, which accounts to a smaller γ of 0.0047 W$^{-1}m^{-1}$

For the PCF under consideration, the dispersion parameter (D) Vs wavelength data is provided by the manufacturer and represented by Figure A.1(a). The group velocity dispersion (GVD) coefficient β_2 can be calculated as

$$\beta_2 = \frac{-0.001 D \lambda^2}{2\pi c} ps^2/m \tag{A.3}$$

The value of GVD coefficient for the PCF is obtained by substituting the appropriate values in Equation A.3 i.e. $\beta_{2\ PCF}$= 0.006339 ps^2/m.

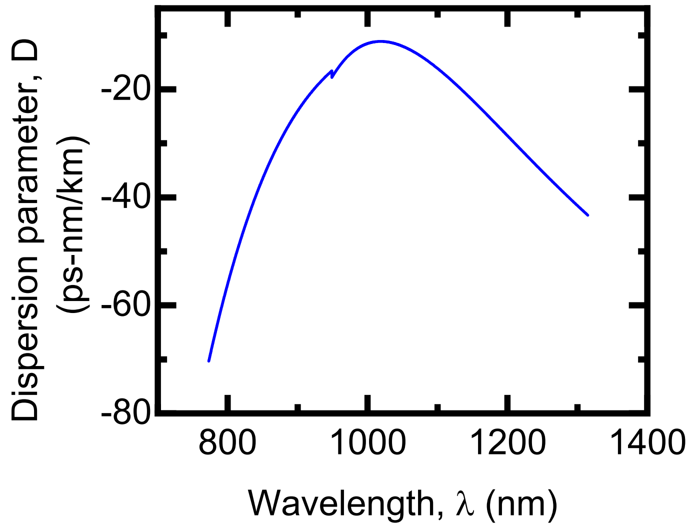

Figure A.1: Dispersion parameter distribution with respect to wavelength

In the vicinity of zero dispersion wavelength, it is necessary to calculate higher order dispersion terms for the PCF. The following steps should be followed to do so.

- STEP-I: Plot GVD coefficient, β_2 Vs frequency, ω graph as Taylor expansion of dispersion (given by Equation A.4) is in terms of frequency, ω. Figure A.3 shows such graph.

- STEP-II: Use curve fitting tool and obtain the curve fitting polynomial. For the purpose of this dissertation, curve fitting tool from MATLAB is used to estimate the fitting polynomial. The snapshot of this curve A.3.

- STEP-III: Calculate the higher dispersion coefficient based on the coefficients of polynomial. The polynomial obtained from the Figure A.3 is represented by Equation A.5. By comparing the coefficients Equation A.5 with that in Equation A.4, higher dispersion terms can be calculated. All these coefficients are listed in Table A.1.

$$\frac{\beta(\omega)}{\omega} = \beta_2(\omega) = \beta_2 + \beta_3(\omega-\omega_0) + \frac{\beta_4}{2}(\omega-\omega_0)^2 + \frac{\beta_5}{6}(\omega-\omega_0)^3 + \frac{\beta_6}{24}(\omega-\omega_0)^4 + \ldots \quad \text{(A.4)}$$

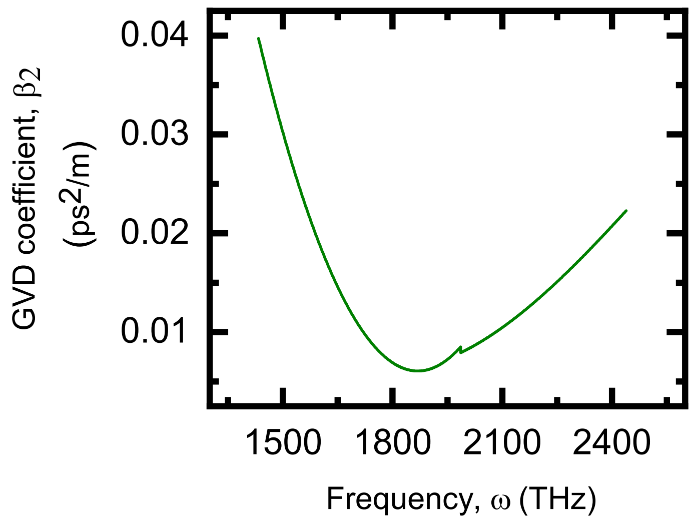

Figure A.2: GVD distribution with respect to frequency

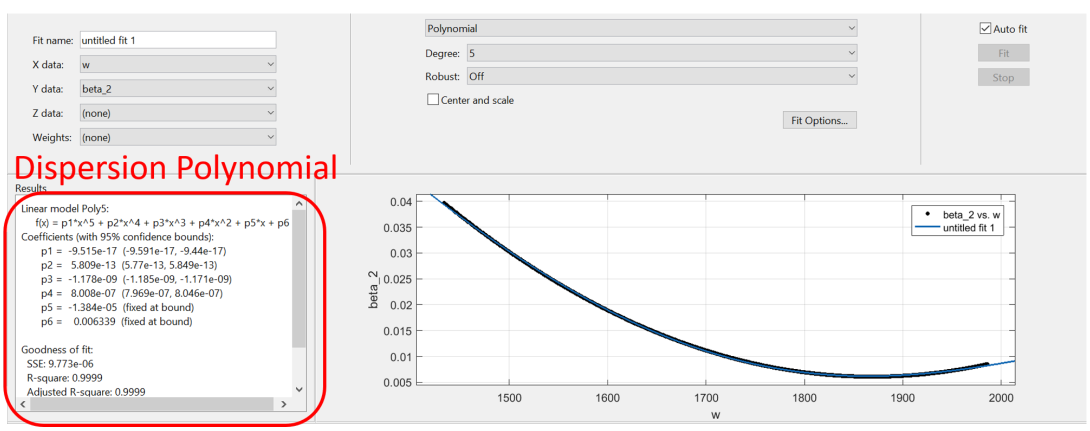

Figure A.3: Curve fitting window for the plot of GVD Vs frequency

Table A.1: Dispersion terms for the PCF

Dispersion coefficient	Value
β_2 (GVD)	0.006339 ps^2/m
β_3 (TOD)	1.384 $\times$ 10^{-5} ps^3/m
β_4	1.605 $\times$ 10^{-6} ps^4/m
β_5	-7.068 $\times$ 10^{-9} ps^5/m
β_6	1.394 $\times$ 10^{-11} ps^6/m
β_7	1.418 $\times$ 10^{-14} ps^7/m

$$f(x) = p_1x^5 + p_2x^4 + p_3x^3 + p_4x^2 + p_5x^4 + p_6 \tag{A.5}$$

Where, p_1 = -9.515 $\times$ 10^{-17} ps^7/m, p_2 = 5.809 $\times$ 10^{-13} ps^6/m, p_3 = -1.178 $\times$ 10^{-9} ps^5/m, p_4 = 8.008 $\times$ 10^{-7} ps^4/m, p_5 = -1.384 $\times$ 10^{-5} ps^3/m, p_6 = 0.006339 ps^2/m.

APPENDIX B

Group Velocity Dispersion Calculation for Praseodymium doped ZBLAN Fiber

The Sellmeier equation (Equation B.1) is an empirical relationship between refractive index and wavelength for a particular medium and this equation can be used to determine the dispersion of light in the material. The coefficients in Equation B.1 are provided by the manufacturer of praseodymium (Pr) doped ZBLAN fiber and summarized in table B.1 and the refractive index variation is plotted in Figure B.1.

$$n^2 = 1 + \frac{a\lambda^2}{(\lambda^2 - b^2)} + \frac{c\lambda^2}{(\lambda^2 - d^2)} + \frac{e\lambda^2}{(\lambda^2 - f^2)} \tag{B.1}$$

Table B.1: Sellmeier cofficient for Pr doped fiber

Sellmeier coefficient	Value
a	0.341643
b	70.20748
c	0.919276
d	100.874
e	0.305464
f	9951.811

Now, the dispersion parameter of the fiber , denoted by 'D' with the units of 'ps/km-nm' is related to the material refractive index by Equation B.2.

$$D_\lambda = -\frac{\lambda}{c}\frac{d^2n}{d\lambda^2} \tag{B.2}$$

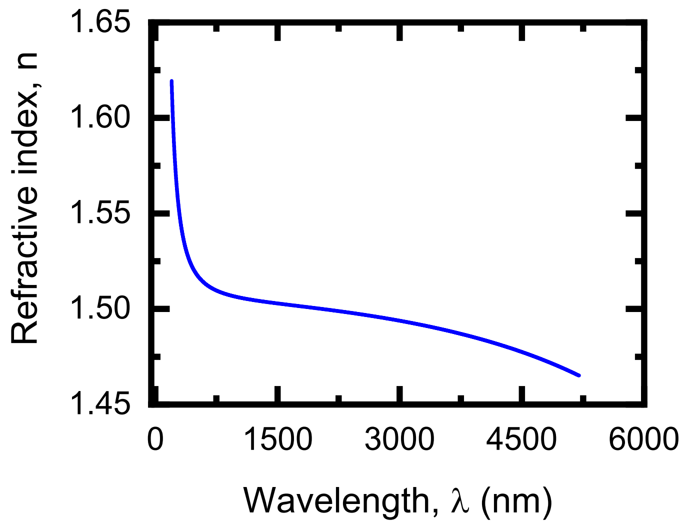

Figure B.1: Refractive index vs. wavelength for Pr:ZBLAN fiber

One can see that the dispersion parameter graph for this fiber is different than the one for silica fiber(PCF) shown in Figure A.1. By substituting the values for D parameter obtained from Figure in Equation A.3, GVD coefficent can be calculated at different wavelengths in visible region and these values are summarized in Table B.2.

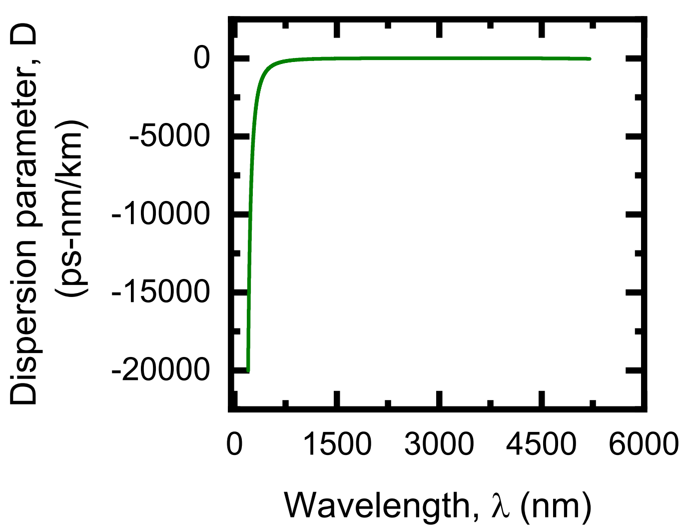

Figure B.2: Material dispersion parameter for Pr:ZBLAN fiber

Table B.2: GVD cofficient for Pr doped ZBLAN fiber

Wavelength	GVD coefficient (β_2) value
520 nm	0.82 ps^2/m
603 nm	0.685 ps^2/m
635 nm	0.647 ps^2/m